George C. Hadjisavvas

Theoretical Investigation Of The Properties Of Nanostructured Semiconducting Systems With Monte Carlo Simulations And First Principles Calculations

A Doctoral Dissertation

Physics Department, University of Crete
Heraklion, Greece
2005

George C. Hadjisavvas

Theoretical Investigation of the Properties of Nanostructured Semiconducting Systems with Monte Carlo Simulations and First Principles Calculations

A Dissertation
submitted to the Physics Department, University of Crete
in partial fulfillment of the requirements for the Degree of
Doctor of Philosophy in Physics

Heraklion, Greece, December 2005

Theoretical Investigation of the Properties of Nanostructured Semiconducting Systems with Monte Carlo Simulations and First Principles Calculations

Thesis author George C. Hadjisavvas

Thesis supervisor Prof. Pantelis C. Kelires

Thesis committee
P. C. Kelires
E. Kaxiras
S. Logothetidis
N. Papanicolaou
E. N. Economou
X. Zotos
N. Flytzanis

Physics Department, University of Crete
Heraklion, Greece

2005

Thesis Abstract

The scope of the present dissertation is to simulate two different types of nanostructures, namely quantum islands and quantum nanocrystals. The former nanodots are formed during heteroepitaxial growth. We will be focused in the formation of Ge islands on Si(100) substrate. The islands, which will be studied, might have the shape of a pyramid or of a dome. Ge islands formed on a Si(100) surface, which is precovered with a small amount of C, are a special and important class of Si-based nanostructures. These type will also be studied. The latter nanostructures are embedded nanocrystals in a matrix, usually amorphous. These quantum dots are formed by various techniques, such as implantation and laser ablation. A lot of interest exhibits the case of Si nanocrystals in a-SiO_2. In the first chapter a historical overview and the main aspects of each type of nanostructure is presented.

The structure, composition and energetics of such nanostructures are studied. In order to do this, Monte Carlo simulations within the empirical potential approach utilizing two different potentials were used. Also, optoelectronic properties of the embedded nanocrystals are extracted with Density Functional Theory (DFT) within the Local Density Approximation (LDA) and Generalized Gradient Approximation (GGA). A few details concerning the methods and the simulational aspects are included in the second chapter.

The bare Ge dots, either pyramids or domes, formed on Si(100) are firstly investigated. The stress and the composition profiles of those islands are calculated and compared. Also, from the comparison of those properties in the alloyed and non-alloyed dots many issues, concerning diffusion and intermixing, are interpreted. Volume exchange events and stress-driven intermixing need to be considered for the interpretation of experimental results.

In the next section Carbon-induced Ge dots on Si(100) are studied. Since C atoms affect very much the resulting structures and properties, it is important to know how they are distributed in the surface, or even if they occupy cites in and below the islands. It is found that the dots do not contain C, and that they have a gradual composition profile from SiGe at the bottom to bare Ge at the apex. Also, the effect of the Ge and C coverage are subjects which are investigated.

The case of the embedded Si nanocrystals in a-SiO_2 matrix are explored in the nect section. The interface structure and its energetics are studied as a function of the nanocrystal size. It is found that the low energy geometries at the interface are Si-O-Si bridge bonds. The reduction of their fraction as the size becomes smaller and the substantial deformation in small nanocrystals, give us the opportunity to give an

alternative explanation for the reduction of the optical gap in this size regime.

The size and the interface of such structures is found to play vital role in the photoluminescence. So, it is important to know if they have spherical of faceted shape. In order to examine this, seven planar interfaces of Si/SiO_2 with different crystal orientations for the Si substrate are constructed. Minimizing the surface energy of a volume with the calculated energies, a nanocrystal with 42 facets, mainly (100), (110) and (121) orientations, is found as the optimum shape. A comparison between a faceted and a spherical embedded nanocrystal revealed that the former might exist under some thermodynamic conditions.

Finally, the reduction of the band gap, with respect to the quantum confinement model, of the embedded Si nanocrystals is verified from our simulations. Also, besides the Si-O-Si bridge bonds and Si=O double bonds, which is beleived to pin the gap of the oxidized nanostructures, we found that distortions are also responsible for the behavior of these nanocrystals. A factor which have poorly been considered in litterature.

Acknowledgments

I would like to express my gratitude to my supervisor Prof. P.C. Kelires whose expertise, understanding, and patience, added considerably to my graduate experience. Without his support I would not have finished this thesis.

Immense thanks should be given to my family. Their love and support they provided me through my entire life was of immeasurable value to me.

I also feel the need to thank many other people who helped me while I was working this thesis. In particular, I must acknowledge M. Fyta and C. Mathioudakis for being good colleagues and also good friends. Their support and discussions were valuable for me. Special thanks goes to K. Giannakoudaki for standing by me in the difficult times. The encouragement and the editing assistance she offered me was catalytical. Last but not least, I would like to thank all my friends for being so patient and for their support throughout my academic years.

Contents

Thesis Committee . . . iii

Thesis abstract . . . v

Acknowledgments . . . vii

Preface . . . xiii

1 Introduction 1

1.1 Quantum Nanostructures . . . 1

1.2 Quantum Islands . . . 2

1.2.1 Growth mechanisms . . . 2

1.2.2 Shapes and Sizes of islands . . . 4

1.2.3 Interdiffusion . . . 6

1.3 Quantum Nanocrystals . . . 8

1.3.1 Preparation methods and conditions . . . 9

1.3.2 Sample Characteristics . . . 10

1.3.3 Shapes of Nanocrystals . . . 11

1.3.4 Theoretical work in literature . . . 12

2 Methodology 19

2.1 Methods of Simulations . . . 19

2.2 The Monte-Carlo Method . . . 21

2.2.1 The Metropolis Algorithm . . . 22

2.3 Ensembles . . . 23

2.3.1 Canonical ensemble - (N,V,T) . . . 23

2.3.2 Isobaric-Isothermal Ensemble - (N,P,T) . . . 24

2.3.3 Grand Canonical Ensemble - (μ,V,T) . . . 25

2.3.4 Isobaric-Semigrand Ensemble - (N,P,T,$\Delta\mu$) 26
2.4 The Wooten-Winer-Weaire Method 28
2.4.1 Bond Switch Moves 29
2.4.2 WWW methodology 30
2.4.3 Modifications of the WWW method 32
2.4.4 Bond Conversion Moves 33
2.5 Empirical Potentials 33
2.5.1 Tersoff Potential 35
2.5.2 Stillinger-Weber Potential 36
2.5.3 Keating-like Potential 37
2.6 Atomic Level Stresses 38
2.7 Wulff Construction Method 38
2.8 First Principles Calculations 39
2.8.1 The Problem 40
2.8.2 Born-Oppenheimer Theory 41
2.8.3 Density Functional Theory 41
2.8.4 Local Density Approximation (LDA) 43
2.8.5 Generalized Gradient Approximation (GGA) 44
2.8.6 Plane Waves and Pseudopotentials 44
2.8.7 The V.A.S.P. Software 46

3 Bare Ge Dots **47**
3.1 Introduction 47
3.2 Simulation 49
3.3 Results 51
3.3.1 Stress profiles of non-alloyed domes 51
3.3.2 Composition profiles of alloyed domes 51
3.3.3 Stress profiles of alloyed domes 57
3.4 Conclusions 57

4 Carbon-induced Ge Dots on Si(100) **59**
4.1 Introduction 59

4.2 Simulation 61
4.3 Results 62
4.3.1 Stress profile on non-alloyed islands 62
4.3.2 Composition profiles of alloyed islands 64
4.4 Conclusions 69

5 Si Nanocrystals Embedded in a-SiO_2 I. Spherical Nanocrystals 71
5.1 Introduction 71
5.2 Simulation 72
5.2.1 Construction and Amorphization of the Cell 72
5.2.2 Construction of the Cell 73
5.2.3 Amorphization of the Matrix 73
5.3 Results 74
5.3.1 Structural Characteristics 74
5.3.2 Oxygen penetration 75
5.3.3 Chemical Composition 76
5.3.4 Bridge Bonds 78
5.3.5 Interface Energy 78
5.4 Conclusions 82

6 Si Nanocrystals Embedded in a-SiO_2 II. Faceted Nanocrystals 83
6.1 Introduction 83
6.2 Simulation 84
6.3 Results 85
6.4 Spherical vs Faceted Nanocrystal 91
6.5 Conclusions 95

7 First Principles Calculations 97
7.1 Introduction 97
7.2 Simulations 99
7.3 Results 100
7.3.1 Hydrogenated Si-nc and Quantum Confinement 100

7.3.2 Hydrogenated Si-nc with Oxygen 102
7.3.3 Embedded Si nanocrystals in a-SiO_2 104
7.4 Conclusions 108

Appendices **111**

A Optical Properties **113**
A.1 Introduction 113
A.2 Results 114
A.2.1 Bulk Si 114
A.2.2 Amorphous Si 116
A.2.3 Bulk β-cristobalite SiO_2 116
A.2.4 Embedded Si Nanocrystals 116

List of Figures **121**

List of Tables **127**

Publications **129**

Bibliography **131**

Preface

Computational physics is much more than "Physics Using Computers". The essential point in computational physics is not the use of machines, but the systematic application of numerical techniques in place of, and in addition to, analytical methods, in order to render accessible to computation as large part of physical reality as possible. The use of computers in physics, as well as most other branches of science and engineering, has increased many times along with the rapid development of faster and cheaper hardware. Many physical problems have been solved thanks to the Computational Physics.

However, It is well accepted that many physical problems can not be solved analytical. Also, despite the fact that great insight is gained through experiments, in some cases there are controversial experimental findings. The aim of computational physics is to solve those physical problems, or even to resolve the controversy, which is exists in some aspects.

The present dissertation deals with nanostructured semiconducting materials. Nanostructures are defined as "an assembly of building blocks on the scale where their properties become different from their bulk counterparts". Due to their interesting properties, are found to be the promising materials for advanced electronic devices and optical applications.

Among them, increased attention has been received by two different type of nanostructures, namely quantum islands, which are formed during heteroepitaxial growth, and quantum nanocrystals, which are embedded nanoclusters in a host matrix. Their shape, size, interdiffusion, chemical composition and strain patterns, are some of the parameters which affect their properties. However, some aspects can not be easily measured with the current experimental techniques and a theoretical answer is needed.

In this dissertation, we are aiming at providing an accurate and realistic picture of some aspects, which concerns these type of nanocrystals, and can not be straight-

ened out without the contribution of computational physics. These findings may be important for future studies or even applications.

Chapter 1

Introduction

Two different semiconductor nanostructures are the subject of the present thesis, namely quantum islands and quantum nanocrystals. The former nanodots are formed during heteroepitaxial growth. We will be focused in the case of Ge islands on Si(001). The latter nanostructures are embedded nanocrystals in a matrix, usually amorphous. A lot of interest exhibits the case of Si nanocrystals in a-SiO_2. The main aspects of each case will be given in this first chapter.

1.1 Quantum Nanostructures

A Quantum Nanostructure, also called a quantum dot, is a semiconductor crystal whose size is of the order of a few nanometers to a few hundred nanometers. These quantum dots confine electrons, holes, or electron-hole pairs (so-called excitons) to zero dimensions, in a region of the order of the electron de Broglie wavelength. This confinement can be one-dimensional as in quantum wires, two-dimensional as in quantum wells, and three-dimensional as in quantum nanocrystals. This confinement leads to discrete quantized energy levels and to the quantization of charge in units of the elementary electric charge. Quantum Dots are particularly significant for optical applications due to their high quantum yield.

Two main factors have led to the increasing attention received by semiconductor nanostructures, in the last decade. First of all, they provide a mean to create artificial potentials for carriers, electrons, and holes in semiconductors at length scales where confinement takes place. Beside the fundamental point of view, semiconductor nanostructures have a large potential for applications in nanoelectronics and optoelectronics. This is because by using the confinement effect, new device concepts become feasible, which provide additional degrees of freedom in design. Thus, quan-

tum mechanics becomes applicable not only in systems of academic interest, but also in systems of practical impact.

Two classes of nanostructures exhibiting great scientific interest are quantum islands, formed on a substrate during heteroepitaxial growth, and embedded nanocrystals in a matrix, which is usually amorphous. These two types will be the subject of this thesis. Our aim is to carry out a thorough investigation of the structure, composition and energetics of the materials. For the latter class, the optoelectronic properties are also studied. A historical overview and the main aspects of each type will be discussed in the next sections.

1.2 Quantum Islands

Semiconductor nanostructures often consist of different semiconducting materials having different bandgaps. This leads to a confinement of the motion of excitons, resulting in the strong photoluminescence due to the recombination of electrons and holes, and making these materials very important for optoelectronic applications. It is possible to grow heterostructures where the motion is restricted in three dimensions resulting in nanometer-sized quantum islands. The idea is to have as pure the composition of the islands (just one component) with respect to the surroundings as possible, so as to enhance confinement. For quantum mechanical reasons, the dots behave as big molecules, there are only certain energy levels allowed within this islands.

During molecular beam epitaxy, under certain conditions, quantum dots nucleate spontaneously when a material is grown on a substrate to which it is not lattice matched. For example, the spontaneous formation of germanium dots on silicon under certain growth conditions occurs because of the large difference (4 %) in lattice spacing between the two elements. The resulting strain produces coherently strained islands on top of a two-dimensional "wetting-layer". The epitaxial growth of self-assembled quantum dots is an important technique to prepare novel structures for optical and semiconductor devices.

1.2.1 Growth mechanisms

Several methods for the self-organized growth of semiconductor nanostructures have been suggested. The most prominent one is certainly the Stranski-Krastanow growth method [1, 2, 3]. This mode, leading to the formation of nanoscale islands on top of a two-dimensional (2D) wetting layer, occurs for almost any semiconductor heterostructure, with a certain lattice mismatch between the constituent materials.

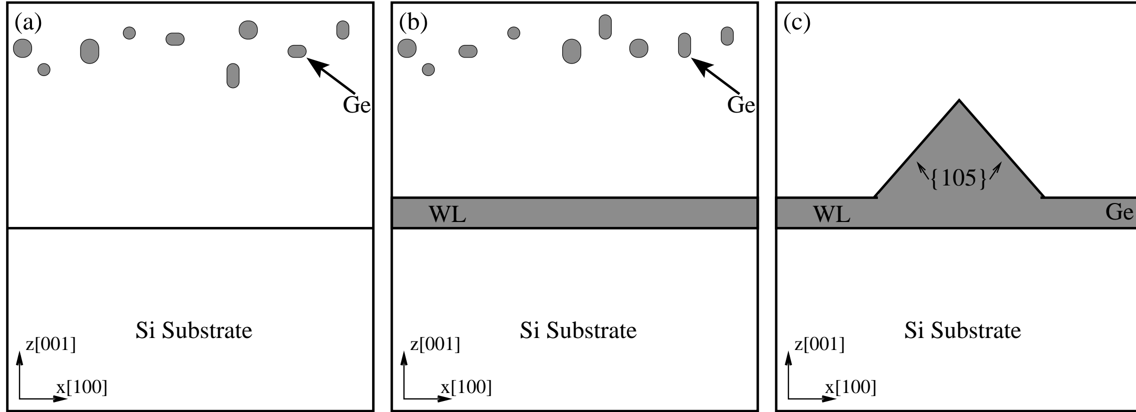

Fig. 1.1: Schematic representation of Stranski-Krastanow growth. (a) The bare Si(001) substrate is shown while the first atoms (or clusters of atoms) of Ge are going to be deposited on the surface. (b) Ge atoms wet the substrate without forming any island until a critical thickness of this *wetting layer*. (c) Dots are formed.

Fig. 1.1 shows a schematic illustration of the Stranski-Krastanow growth mode. In panel (a) the pure substrate, Silicon (100), and the Germanium atoms falling onto the surface of Si, just like in the Chemical-Vapor-Deposition (CVD) method, are illustrated. The first step is the formation of the two-dimensional wetting layer, which was mentioned above, Fig. 1.1(b). The formation of the wetting layer (WL) is favored because it relives the elastic energy, stored in the growing hetero-epitaxial layer. This relief depends on the type of the materials and especially on their misfit. Finally, Fig. 1.1(c), shows the formation of quantum islands on the WL. The essence of this method lies in the formation of the WL.

The driving force, for the self-organization processes during growth, is the misfit between the crystal lattice of the growing layer, and that of the substrate which, in turn, creates strain in the growing layer. Numerical analysis reveals that the critical thickness decreases with increasing mismatch. For the case of Ge on Si, having 4% mismatch, the thickness equals to approximately four monolayers. Thus, this thickness could be reduced by simply increasing the mismatch.

Using the above analysis, one should achieve the formation of islands without any wetting layer. This mechanism is called the Vollmer-Weber growth mode. The steps of this mode are shown in Fig. 1.2. The quantum dots appear at the initial stages, of the deposition procedure, panel (b). Further deposition of Ge atoms/molecules, just increases the size of the dot and wets the rest of reconstructed Si surface.

This mode can be easily activated by using a substrate with smaller lattice constant, for example Si_xC_{1-x}. In this case, islands with very small dimensions (base

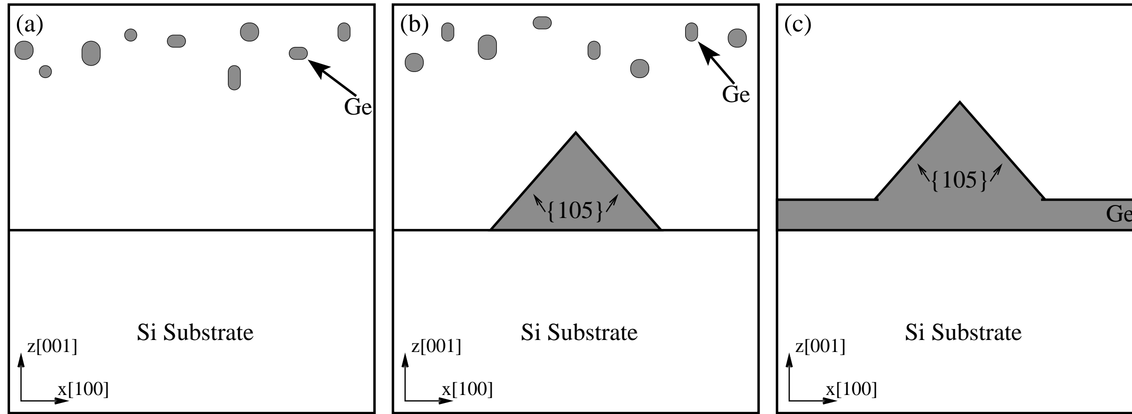

Fig. 1.2: Schematic representation of Vollmer-Weber growth. (a) The bare Si(100) substrate. (b) Islands are formed immediately, without the formation of a 2D wetting layer. (c) Further deposition wets the rest surface and covers the already formed island.

width of only 10 nm and a height of about 1 nm) can be nucleated. This gives rise to strong photoluminescence signal from such islands.

It is found that the predeposition of C, mainly with Molecular Beam Epitaxy (MBE), leads to C-rich "patches" on the surface with a (4×4) reconstruction [4]. Ge adatoms do not stick to these patches, because of the chemical repulsion between Ge and C atoms [5, 6], and so, the islands grow among those areas, on the (2×1) areas of the surface. This explains the observed small island sizes, as well as the photoluminescence properties. However, it turns out that the island formation is actually more complicated and not only the strain but also the bond chemistry, between Si, Ge and C, needs to be considered. Also, since C atoms play such a vital role, it is essential to know how they are distributed on the surface region, or even if they occupy cites in and below the dots.

1.2.2 Shapes and Sizes of islands

In SiGe on Si heteroepitaxy four forms of islands are observed: shallow mounds, which are also called prepyramids, square pyramids with {105} facets, hut clusters, which are elongated pyramids with {105} facets and large domes with facets in several orientations.

In Fig. 1.3, typical shapes of (a), (b) Ge domes, (c) pyramids, and (d), (e), (f) shallow mounds (prepyramids) are presented, obtained by STM with atomic resolution [7]. In the first stage of growth, shallow prepyramids are formed. Their

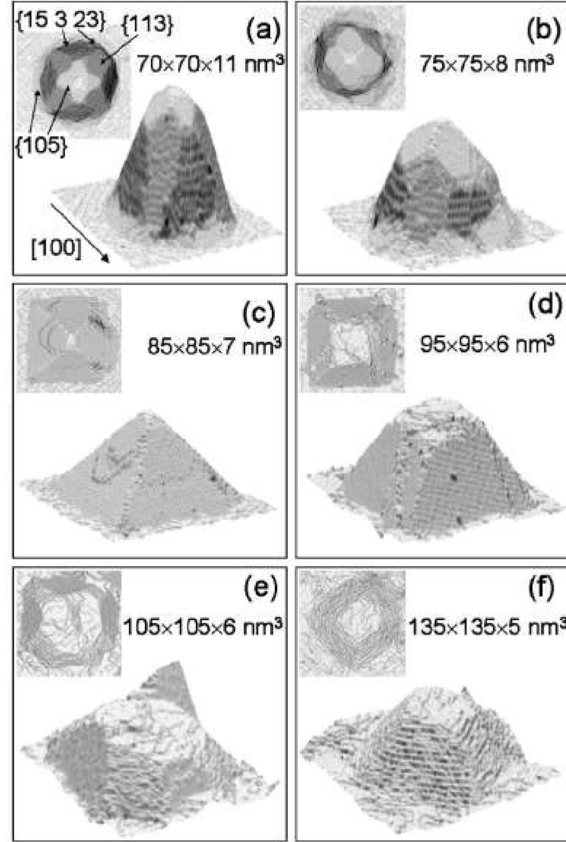

Fig. 1.3: Typical Ge island shapes, obtained by STM, during Si capping of Ge domes, grown on Si(001): (a),(b), domes; (c) pyramids; (d)-(f) prepyramids. The Si coverages are 0, 1, 2, 4, 8, and 16 ML's for panels (a)-(f). Taken from Ref. [7].

side walls increase gradually until an angle of about 11° is reached [8, 9, 10, 11], which corresponds to the {105} facets. Gradually, these shallow mounds convert via T pyramids to pyramids. *T pyramids* are {015} pyramids with rounded top. Large domes are formed for Ge coverages above 5 monolayers (ML) and finally we get superdomes. The structure of Ge domes on Si is complicated. The crystallographic facets, which are observed, are the {113}, {105}, {15 3 23} and a top {001} facet parallel to the substrate surface [7, 12, 13]. Finally, in superdomes except of the previous facets, {111}, {126} and {4 20 23} are also observed.

The size distribution of these islands, as well as their evolution during growth, are shown in Fig. 1.4. These results have been determined by AFM and STM, during Ge deposition on Si(001) [11]. They point out that the prepyramid height-to-width ratio (aspect ratio) varies from 0.03 to 0.05 with increasing island size. In contrast, pyramids exhibit an aspect ratio of 0.1 which remains approximately constant as the

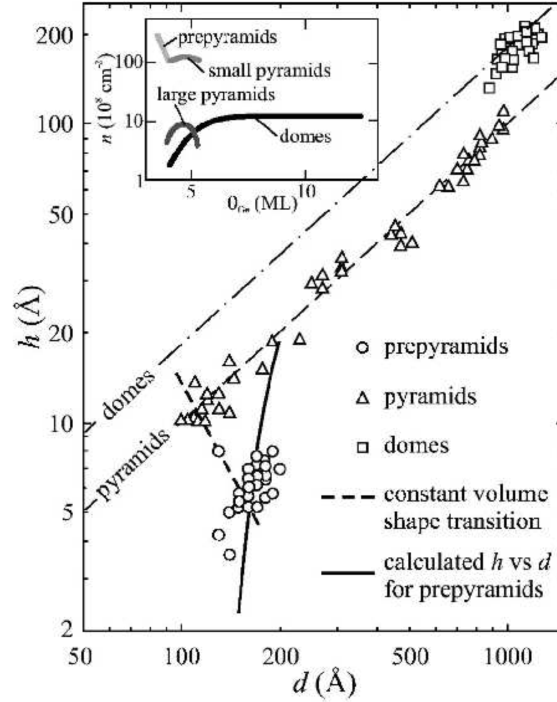

Fig. 1.4: Size distribution of several island types, during deposition of Ge on Si(001). The inset shows the time evolution of the island density for different types. Adapted from Ref. [11].

pyramid size increases. On the other hand, domes have an aspect ratio of about 0.18. Note that pyramids and domes are observed, during growth, at higher temperatures, while the much smaller hut clusters are formed at lower growth temperatures.

Take into account that a reverse shape transition occurs during capping with Si. So, a transition from domes to pyramids and even back to shallow mounds has been observed [7]. Also, both an increase of the island base width and a decrease of the island height is noted [14].

1.2.3 Interdiffusion

It has become apparent that the most challenging problem for a complete description of the islanding phenomenon is the issue of intermixing. Without analysing and settling this issue, many other important processes cannot be fully understood. These include the island nucleation process [15, 16, 17, 18], self-assembling and organization [19], and shape transitions [20]. For example, significant interdiffusion and mixing of species is expected to affect the nucleation process, because the strain field

due to the mismatch will be unavoidably altered and any strain driven mechanism has to take into account. For surface kinetic processes we also need to consider the effect. Similar arguments apply in the case of shape transitions occurring either after post-growth thermal annealing or during capping of the dots with the host material.

But most importantly, intermixing and its extent are expected to affect the confinement within the QDs and their optoelectronic properties. It is therefore vital to gain knowledge about the composition variations within the islands. Note that not only is mere mixing of species an important factor, but so also are any variations of composition and the resulting inhomogeneities. Another related issue is the interlinking of interdiffusion with the stress field in the system. While there have been in the past numerous theoretical investigations of the stress field in QDs [17, 21, 22, 23, 24], no attempts to link stress and composition had been made.

Generally speaking, intermixing is a complicated phenomenon. Simple arguments suggest that interdiffusion of species is favoured, provided that kinetic barriers are overcome, because it lowers the effective lattice mismatch and thus reduces the elastic strain (which partially remains even after islanding takes place). However, whether this phenomenon takes place during or after growth, or at both times, cannot be easily answered. Naturally, higher growth or annealing temperatures would provide the necessary energy to overcome the potential barriers, so a certain degree of intermixing in such cases should be expected. Also, what cannot be speculated beforehand is how compositions vary within the islands and as a function of temperature and size.

From the theoretical point of view, a significant contribution to the problem has been made by Tersoff [25, 26] within continuum elasticity theory. The basic assumption involved in this work is that the composition is determined solely by the variation in strain across the growing island surface, and that there is negligible bulk diffusion within the island. Thus, when the equilibrium surface composition is buried by further growth, it becomes the composition of the interior. However, recent experiments [27] suggesting the possibility for bulk diffusion in the islands shed doubt on this simplification of the problem. An interesting feature, found also by Sonnet and Kelires [28] and Yu and Madhukar [21] in pyramidal islands, is a highly compressed region near, but not at, the island edges. It is found that intermixing is driven by strain energy enhancement near the island perimeter, where the strain has a maximum [28]. Also, an effective strain relief mechanism is based on the diffusion from this region toward the island apex.

Experimentally, a number of studies have addressed the problem [29, 30, 31, 32, 33] and suggested that intermixing takes place, but its degree and the stage at which this happens remain controversial. Some of these studies [32, 33] suggested that intermixing is already taking place during growth, especially at high tempera-

tures, *albeit* without quantifying its extent. Other studies [29, 30, 31] provided firm evidence that intermixing at medium growth temperatures is rather initiated after island nucleation, and showed that this is possible at even higher temperatures by controlling the deposition rate. Resent experiments [34, 35] made an attempt to probe the composition profiles within the Ge/Si(100) islands.

The aim of this dissertation is to shed some light into this fuzzy picture, and to discuss some of the critical aspects of stress relaxation and alloying in Ge/Si(100) islands. We report the results of Monte Carlo simulations and the comparison of the simulated profiles with experimental ones.[1]

Also, the case of Ge islands formed on a Si(100) surface, which is precovered with a small amount of C, is studied. The controversy which exists in experimental results, concerning the distribution of C atoms in the surface region, in and below the dot, is resolved. The stress fields and the associated composition profiles in small pyramidal islands and the surrounding surface region is extracted.[2]

1.3 Quantum Nanocrystals

Since the discovery of intense light emission in porous Si, by Canham, at the beginning of the 1990's [36], a lot of work has been devoted to the study of Si nanostructures, which are related to porous Si. Unfortunately, porous Si has many problems, such as instability of Photoluminescence (PL) efficiency in ambient conditions, and inhomogeneous structural and fragile mechanical properties, while prevent its use in practical applications. On the other hand, Silicon nanocrystals embedded in a-SiO_2 have many advantages, including high stability, self organized quantum well structure and compatibility with metal-oxide semiconductor technology.

The opening of the band gap, when the nc size shrinks, is nowadays an unquestionable fact for Si-nc embedded in a-SiO_2 [36, 37, 38]. This opening arises as a consequence of the quantum confinement of carriers in the three dimensional potential well of the nanocrystal. The PL emission, which is reported for the case of Si nanocrystal, consists of an intense (visible in the naked eye) and wide (about 0.3 eV at half maximum) emission peaking in the near infrared or the visible spectrum (between 1.4 and 1.9 eV).

On the other hand, the oxidization of the nanocrystals is found to influence greatly the PL emission. More specifically, it is shown by many groups that when

[1] Published in: G. C. Hadjisavvas, and P. C. Kelires, *'Critical aspects of alloying and stress relaxation in Ge/Si(100) islands'*, Physical Review B, **72**, 075334 (2005).

[2] Published in: G. Hadjisavvas, Ph. Sonnet. and P. C. Kelires, *'Stress and composition of C-induced Ge dots on Si(100)'*, Physical Review B, **67**, 241302(R) (2003).

the crystalline size decreases to few nanometers, the PL in air does not have the same trend as the one predicted by quantum confinement theory. The PL does not increase much beyond 2.1 eV, even for crystallite sizes below 3 nm. This observation is clearly shown in Fig. 1.5, adapted from Ref. [39], in which the experimental PL energy (measured in Ar and air) and the calculated PL energy as a function of nanocrystal sizes are presented. Note that in zone I and II the PL peak energies are almost the same while in zone III there is a substantial difference. It is widely believed that, in zone III oxygen creates trapped electron and hole states on nanocrystalline surfaces and so the trapped surface states reduce the effective size of the optical gap.

In order to understand the origin of this redshift, the influence of various gas environments was examined. A large redshift was observed as soon as the samples were transfered from Ar to pure oxygen atmosphere. In contrast, no redshift at all was detected when the samples were kept in pure hydrogen or in vacuum [39]. As a consequence, it is assumed that the redshift was related to surface passivation and due to the presence of oxygen.

It is believed that an active role in the PL efficiency plays the Si/a-SiO_2 interface, both by forming radiative states and by passivating the non-radiative ones [39, 40]. Therefore, a stoichiometric a-SiO_2 matrix and a perfect Si/a-SiO_2 interface, are of essential importance. In literature, two main nanostructures are studied, Si nanocrystals (nc) and Si/insulator multilayers.

1.3.1 Preparation methods and conditions

Silicon nc have been produced with several different techniques. These include high-dose Si implantation in SiO_2 [41, 42, 43], laser ablation [44, 45], gas evaporation [46], sputter deposition [47, 48], low-energy cluster beam deposition (LECFD) [49], plasma-enhanced chemical vapor deposition (PECVD) of sub-stoichiometric Silicon oxide (SiO_x) [50] and even annealing of SiO_x thin films [51]. All of them have their own advantages and disadvantages. The main aim of these methods is to achieve the control of the size profile of the nanocrystals. So, among these techniques, ion implantation is one of the most suitable choices, giving distributions of nanocrystal sizes with width of about 0.6 nm (at half width).

On the other hand, the samples were characterized by different techniques such as infrared spectroscopy, atomic force microscopy (AFM), Scanning Tunneling Microscopy (STM), high-resolution transmission electron microscope (HRTEM), Rutherford backscattering spectrometry (RBS), x-ray absorption spectroscopy (XAS), etc.

Again, just as in the case of preparation methods, each technique has its own characteristics. It should be noted that, currently, HRTEM is the tool used to image

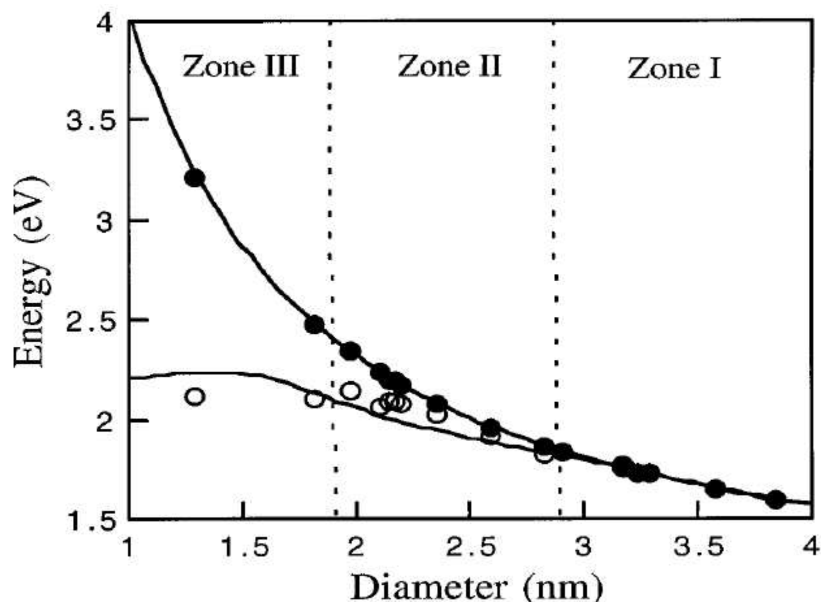

Fig. 1.5: Comparison between experimental and theoretical PL energies as a function of crystalline size. The upper line is the free exciton band gap and the lower line is the lowest transition energy in the presence of a Si=O bond. In zone I the PL peak energies are identical, whether the samples have been exposed to oxygen or not. Adapted from Ref. [39].

individual Si-nc. However, it is not necessarily the best imaging technique, when quantitative and statistical measurements have to be performed. Also, the poor contrast between Si and SiO_2 makes the measurements extremely difficult. Note that nanocrystals with a diameter of less than 1.0 nm are very difficult to be distinguished from the SiO_2 matrix [52]. In this size regime, the nanocrystal is consists of about four planes of atoms.

1.3.2 Sample Characteristics

The various techniques and experimental conditions used to prepare these systems, give rise to samples with different chemical, structural and optical properties. As a consequence, the interpretation of the light emission mechanism, given in different works, is often controversial mainly due to the lack of accurate sample characterization.

Important information concerns the amount of Si atoms segregated in the Silicon nanocrystals, the evaluation of the size and distribution of the clusters. The chemical composition and structure of the interface (and even the host matrix) are also crucial

parameters. However, the actual structure of the amorphous matrix depends on Si concentration, deposition parameters, and annealing treatments. The Silicon total content of most samples vary from 35 to 46 %.

The main findings are summarized below:

- It is known that Si nanocrystals exhibit strong photoluminescence in the red, when their sizes are in the range of 3 to 5 nm. Also, the PL energy shifts to larger wavelengths, when the mean size increases.
- Some times, PL is not immediately observable after the preparation of the sample. It takes from few hours to few days until the luminescence becomes clearly visible. This effect is believed to correlate with the progressive oxidation of the surface. So, by increasing the compositional ratio of oxygen, the PL peak wavelength blueshifts, due to the size reduction of nc.
- It has been demonstrated that the luminescence signal from the nc, increases by increasing the annealing temperature. Moreover, the luminescence peak position slightly redshifts by increasing the temperature of the thermal annealing.
- Si-nc are actually surrounded by some sub-stoichiometric SiO_x ($x<2$) transition "amorphous" layer [53]. It has also been shown that the thickness of this amorphous layer increases by increasing the size of the nanocrystals, always representing approximately 10% of the total diameter [54].

1.3.3 Shapes of Nanocrystals

Most researchers focused their investigation on the Silicon nanocrystals of diameter smaller than 5 nm, because of the interesting optical properties of nanocrystals in this size range. However, it has not been observed any deviation from a spherical shape of the embedded nanocrystals in this size regime.

On the other hand, some groups have reported that in larger sizes some crystallographic facets begin to appear [55, 56]. More specifically, Ref. [55] observed highly oriented Si nanocrystals of ~4 to 100 nm in size. Their sample preparation technique is based on the multiple low energy oxygen ion implantation during Si molecular beam epitaxy (LOI-MBE). In addition, they found that the facets, which construct the nanocrystals are mainly the (100) and (111). A high resolution TEM image of an embedded Si nanocrystal is shown in Fig. 1.6. The diameter of this nanoparticle is about 160 Å, while the (100) and (111) facets are easily identified.

Y. Q. Wang *et al.* [56], on the other hand, used high-fluence implantation of Si ions into amorphous SiO_2 and annealing. They found that faceting is thermodynam-

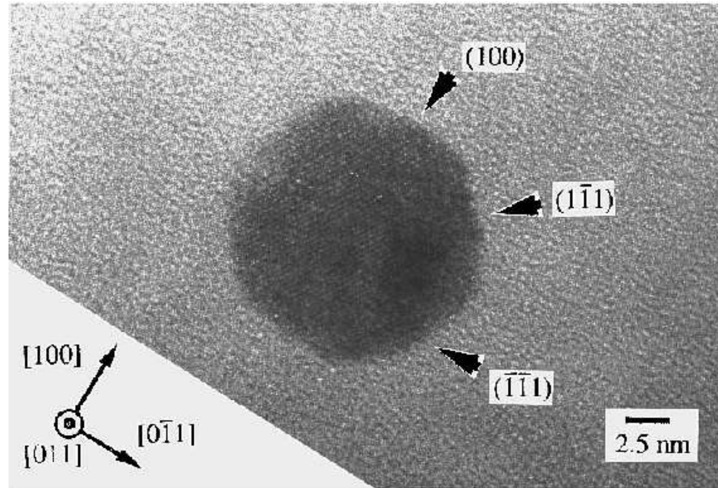

Fig. 1.6: A magnification of a particular Silicon Nanoparticle in a sample with diameter of 160 Å. {100}, {111} and their equivalent facets are identified. Adapted from Ref. [55].

ically favorable to minimize the surface energy, leading to an equilibrium shape. In their case, (100), (111) and (311) facets have been identified, while the faceted Si nanocrystals were of sizes larger than 6 nm.

1.3.4 Theoretical work in literature

Three different systems related to the Si-nc/a-SiO_2 nanocomposite system have been studied until now. The first system is the planar interface of Si/a-SiO_2, which revealed structural and chemical information about the interface. The second system is the free-standing (isolated) Si nanocrystals terminated by either O or H. These systems were mainly used in order to understand the optical properties of the nanocrystals. Finally, a system of a Si nanocrystal embedded in c-SiO_2 was studied, giving results on both structural and optical properties.

Planar interface. Much effort [57, 58, 59, 60] has been devoted to the understanding of the planar Si(001)/a-SiO_2 interface. It is found that the lowest energy structural element is a bridge bond. A bridge bond is a Si-O-Si bond connecting two Si atoms on the surface of the substrate. These bonds can bend and stretch with minimal energy cost. The structure with the lowest interface energy is found to be an abrupt transition between the Si substrate and the a-SiO_2. More specifically, two very close energetically structures are the most favorable ones, the check and stripe phase. Both of them consist of fully bridge-bonded structures. These two structures are shown in Fig. 1.7.

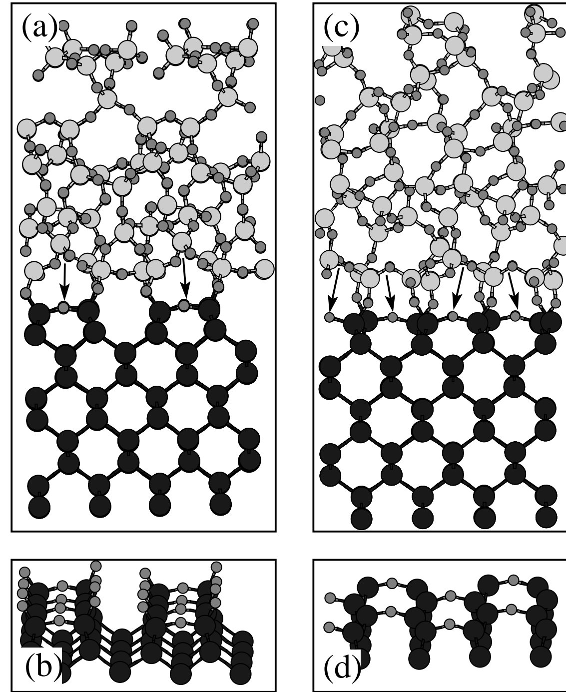

Fig. 1.7: Planar interface Si(100)/a-SiO_2. Two very close energetically structures, stripe (a),(b) and check (c),(d) phase. Arrows indicate bridge bonds. The black (light gray) balls represent Si atoms in substrate (a-SiO_2) while smaller dark gray atoms denote O.

The existence of bridge bonds has been verified by Monte Carlo simulations by Tu and Tersoff [61]. The level of bridge bonding reached by this simulations was of the order of 75%. Bridge bonds are also found by *ab-initio* calculations to be the lowest structural elements. Furthermore, it is shown that an interface with no suboxide layers (an abrupt transition) has lower energy than an interface with suboxides [59].

The a-SiO_2/Si interface widths reported in the literature range from abrupt to more than 7 Å wide. These variations may reflect different preparation conditions. However, it is quite clear that various measurement techniques probe different aspects of the interface. For example, many methods can not resolve the atomic structure but some average. Other techniques require intrusive sample preparation methods, such as depth profiling by sputtering or etching, which alter the chemistry of the interface.

For the a-SiO_2/Si(111) interface it is shown that the suboxide states, including Si^{+1}, Si^{+2} and Si^{+3}, exhibit different depth distributions. Using a simple model, which is based on the statistical cross-linking of dangling bonds between the Si

Fig. 1.8: Schematic illustration of the chemical composition of the transition layers based on the model of Ref. [63].

substrate and the amorphous SiO_2, a chemically abrupt interface is proposed [62].

The a-SiO_2/Si(100) interface is far more important for device applications and far more suitable for a theoretical investigation than the Si(111) counterpart. Indeed, extensive theoretical studies were recently performed for the a-SiO_2/Si(100) interface. Most of them suggested a chemically graded interface with the suboxide distributed over a range of about 6 Å [63, 64].

More specifically, it is shown that the Si^{+1} and Si^{+2} species have the same depth distribution, while the Si^{+3} species are distributed in a wider region from the interface boundary. In more detail, it is suggested that there are three transition layers. The distribution of the suboxides at each transition layers are, 36% Si^{+1} and 64% Si^{+2}, 71% Si^{+3} and 29% Si^{+4}, and 35% Si^{+3} and 65% Si^{41}, at the first, second and third interfacial layers from the Si substrate, respectively [63]. A schematic illustration of the chemical composition of those transition layers is shown in Fig. 1.8.

However, the knowledge gained from these studies, can not directly be transferred to the case of the Si-nc/a-SiO_2 interface, which is curved, more or less spherical, and so encompasses all crystal orientations. Most importantly, its bonding and energetics are functions of the nc size, due to the dramatic change of surface area to volume ratio, a factor which is absent in the planar case.

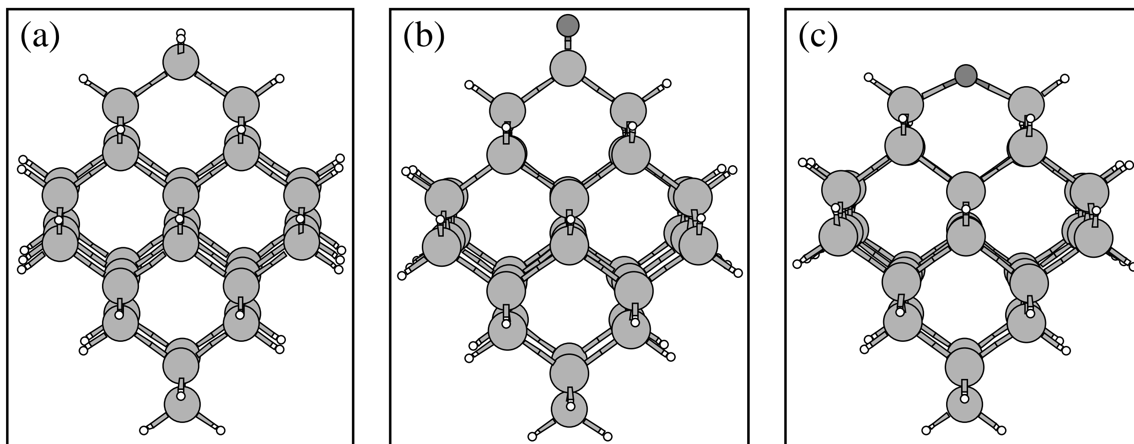

Fig. 1.9: Three different types of isolated Si nanocrystals passivated with H. In panel (a) the nanocrystal is terminated only with H ($Si_{35}H_{36}$), in (b) has one Si=O double bond ($Si_{35}OH_{34}$), and in (c) has one Si-O-Si bridge bond ($Si_{34}OH_{34}$). The light gray atoms stand for Si, the white ones for H and the dark gray for O.

Isolated Si-nc. On the other hand, most of the work concerning isolated Si-nc, passivated by either H or O, is done in order to explain the opening of the band gap during the reduction of the nanocrystals. This is because the observed redshift has been attributed to surface oxidation of silicon nanocrystals. It is believed that oxygen creates trapped electron and hole states on nanocrystalline surfaces. In Fig. 1.9(a) an isolated Si nanocrystal passivated by H is shown.

Different models have been proposed. The group of Ossicini [65] considered the role of the surface geometry distortion of small hydrogenated Si cluster in the excited state. More specifically, they studied the case of a Hydrogen incorporation into a strained Si-Si bond, revealing a lowering in transition energies by 1.1 to 1.2 eV. In this way, they pointed out that distortions should no longer be neglected.

On the other hand, some groups reported that the oxidation introduces defect levels in the Si-nc band gap, pinning their emission energy. These defect levels were due to the formation of Si=O double bonds [39, 66]. A nanocrystal which is passivated by H and has one Si=O double bond is shown in Fig. 1.9(b).

Finally, Vasiliev *at al.* [67] have pointed out that similar results can be obtained also for O connecting two Si atoms (Si-O-Si bridge bonds) at the Si nanocrystal surface. An example of a bridge bond is illustrated in Fig. 1.9(c). All these findings give us the opportunity to conclude that either bridge bonds or double bonds are responsible for the reduction of the band gap.

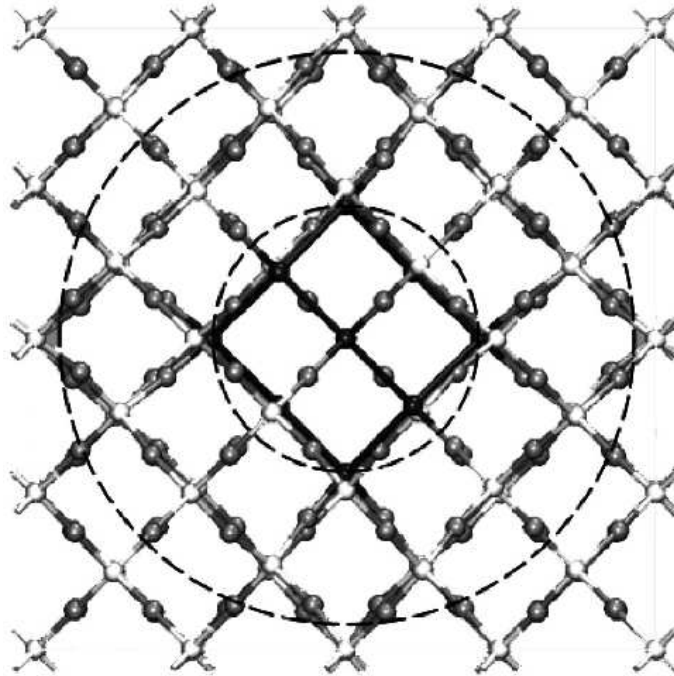

Fig. 1.10: Top view of the relaxed structure for the Si_{10}/β-SiO_2 supercell. The white and the gray balls stand for the Si and O atoms of $SiO_2\beta$, the black ones for the Si atoms of the nanocrystal.

However, those simulated systems ignore the structural changes, which might be induced on both the surface and the inner parts, when the nc are embedded in the amorphous oxide.

Si-nc/c-SiO_2. In the only previous theoretical attempt to simulate the structure of the Si-nc/a-SiO_2 interface [68], a crystalline SiO_2 embedding matrix was used (β-crystobalite). In this case, the core of the Si-nc is of crystalline nature, while the interface, between Si-nc and SiO_2, extends on a transition layer of about 1.0 nm width. Moreover, the structure of this region is progressively changing from the crystalline core to amorphous Si, to stressed SiO_2, and finally to c-SiO_2

An illustration of the studied structure is shown in Fig. 1.10. The two dashed circles help to highlight the three different regions in which the final relaxed structure is organized. The inner region indicates the strained Si nanocrystal, while between the dashed lines is a cap shell of distorted β-SiO_2 around the nanocrystal. In the outer region is shown the crystalline β-SiO_2. The optical properties of this system are compared to experimental data, revealing that not only Si-nc, but also modified silica capping region plays an important role.

> Although this attempt eases the computational load, it is not an accurate representation of the real situation. However, this study represents only the first step towards more complicated models closer to the real samples.

In this dissertation, we are aiming at providing an accurate and realistic picture of embedded nanocrystals, which has not be done so far. We study the structure, the energetics, and the optical properties of these nanostructures.[3]

[3]Published in: G. C. Hadjisavvas, and P. C. Kelires, *'Structure and Energetics of Si Nanocrystals Embedded in a-SiO_2'*, Physical Review Letters, **93**, 226104 (2004).

Chapter 2

Methodology

Two different approaches were used in the present thesis, one based on Monte Carlo method and another based on first principles. Both of them are being described briefly in this section. Methodology, interatomic potentials and statistical ensembles are some of the aspects of the Monte Carlo method. Also, an alternative technique to construct a complete tetrahedral amorphous network (Continues Random Network) is described. For the first principles calculations, the main approximations, such as Born-Oppenheimer, Density Functional Theory, Local Density Approximation, Generalized Gradient Approximation and Pseudopotentials are concepts which are explained.

2.1 Methods of Simulations

Despite the fact that we live in the computer age, we can not simulate the motion of all the atoms of a solid ($\sim 10^{23}$ atoms). This is due to speed and memory limitation of computers. Therefore some approximations should be used in order to simulate these systems and extract their properties. The most important approximation to choose a limited size simulational cell, which is replicated in space, in all directions, by using periodic boundary conditions. In this way the number of atoms which are needed in order to accurately describe the system is reduced dramatically. Also the range of the forces can be approximated and truncated in order to save a lot of computational effort. For example, using short-range forces reduces the number of interactors with a reference atom. Finally, one typical simplification is to simulate only a short life time of the motion of atoms.

On the other hand, there is a well known balance between better statistics and higher accuracy. The more the approximations are made, the less accuracy you

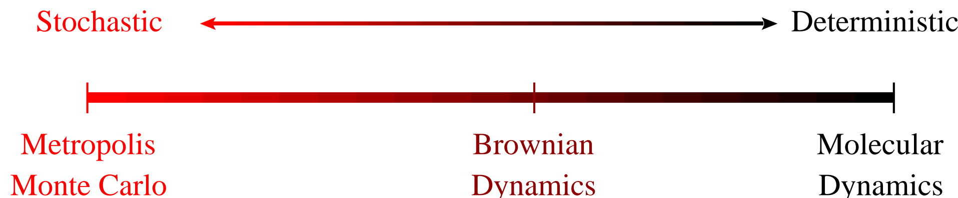

Fig. 2.1: Different simulation methods.

have. However, this gives you the possibility to use more particles in the simulations and thus have better statistics. For example, a calculation becomes tedious when accurate quantum-mechanical forces are used, and statistics necessarily are poor. On the other hand, by using a less accurate classical-empirical description, one has the opportunity to have more simulational time and thus better statistics.

Simulations are typically categorized according to their degree of stochasticity/determinism. Fig. 2.1 shows a schematic of such a categorization. In the left part of this figure the Monte Carlo (MC) method is shown, which is a completely stochastic method. Monte Carlo is usually used in conjuction with empirical potentials (classical energetics, thus no electronic properties are inferred), and so it is in principle less accurate than using either tight binding (TB) or *ab initio* schemes, due to the lack of quantum-mechanical description. On the other hand, advantages of this formalism are the simplicity, the much greater statistical precision in the simulations, and the use of larger cells, which compensate in part the sacrifice in accuracy. Applying the MC approach, systems in equilibrium are studied. The most frequently used ensembles are the canonical (N,V,T) and isobaric-isothermal (N,P,T) ensembles, which will be described later.

In the right part we have all the deterministic methods, i.e. molecular dynamics (MD). In this scheme, using the positions and velocities of the particles the interactions between them are calculated. Then applying Newton laws, the new positions, velocities, accelerations and forces are calculated. Using MD one can study systems of equilibrium and non-equilibrium, while the ensembles which can be used are the (N,V,E), (N,V,T) and (N,P,T). MD is used not only in conjuction with empirical potentials, but also with TB and first-pronciples methods.

Finally there also are methods lying among the two extremes, using some aspects of the stochastic and some of the deterministic method. For example, the Brownian Dynamics approach is an arithmetic solution of the Langevin equation

$$m\bar{a}_i(t) = \bar{F}_i(t) + \bar{A}_i(t) - \xi_i\bar{\nu}_i(t)$$

where $\bar{A}_i$ is a random force and $\xi_i\nu_i(t)$ a dissipative term.

2.2 The Monte-Carlo Method

The Monte Carlo (MC) method is a powerful numerical approach for the approximate solution of complex mathematical problems using sampling techniques. In its most basic application, it is used for the numerical integration of high-dimensional integrals or for the calculation of averages over a multivariable probability distribution.

Standard numerical methods involve the discretization of the integration range into a regular grid and sampling of the integrand over it. In MC method instead of using such a grid, N random numbers in the integration range are taken, x_i, and the mean value, M, of the integrated function f(x) is calculated. In this way the integral will simply be $I = LM$ where L is the integration length and $M = \frac{1}{N}\sum_{i=1}^{N} f(x_i)$. In order to achieve better precision in MC integration the process of sampling is modified to reduce the variance of the function without altering the mean value. This is the concept of *importance sampling* which is tightly connected with the MC method.

The theoretical basis for MC simulations is the theory of *Markov process.* Suppose we have a discrete sequence of random variables x_1, x_2, x_3,... that take values in a finite state space S(N) of N states, generated such as that the next state x_{n+1} depends only on the current state x_n and not on the previous one. A *Markov chain* is the set of the successive states generated by a Markov process, starting from an initial state. The probability of generating the new state j from the state i is called transition probability $P(i \to j)$. Of course the transition probabilities must satisfy the conditions of *positivity* and the *normalization.*

$$P(i \to j) \geq 0 \tag{2.1}$$

and

$$\sum_{j=1}^{M} P(i \to j) = 1, \quad \forall i \tag{2.2}$$

The Markov process is chosen in a way that when the simulation runs long enough, every state i will be passed with a frequency proportional to a desired probability distribution π_i. In order to produce this distribution starting from any initial state, some conditions should be also satisfied. The first one is the *ergodicity condition* which implies that in a Markov process any state j in state space must be accessible by any other state i. The second one is called the *balance condition.* This condition ensures that after the period of time needed for the Markov process to reach the desired distribution, the probability of occurrence of any state in the

Markov chain should not change in time. Finally the *detailed balance condition* says that the Markov process on average should pass from state i to state j as often as it passes from state j to state i, for any pair of states i, j.

2.2.1 The Metropolis Algorithm

The Metropolis Algorithm [69] is a technique to create a Markov chain over some state space, which converges to a desired probability distribution π_i. This algorithm can be very easily used in any ensemble, as it will be shown. As it is mentioned this scheme should satisfy the condition of ergodicity and balance condition. In this way the choice of Metropolis *et al.* for the transition probability was

$$P(i \to j) = \min(1, \frac{\pi_j}{\pi_i}) \tag{2.3}$$

The main steps of the Metropolis algorithm is shown below:

1. Initial configuration of the system
2. Choose randomly an atom
3. Move it $r \to r'$
4. Compute the difference of the potential $\Delta W = W(\bar{r}') - W(\bar{r})$
5. If $\Delta W < 0$ accept the move and continue from step 2.
6. Compute $p = e^{-\beta \Delta W}$.
7. Pick a random number h(0,1).
8. If h<p keep configuration and go to step 2.
9. Reject it and go to step 2.

where the potential ΔW is tightly connected with the transition probability π_i which was used above. It depends of the ensemble which is used. In the next sections we will see all the ensembles used in our simulations and how this potential changes in each one.

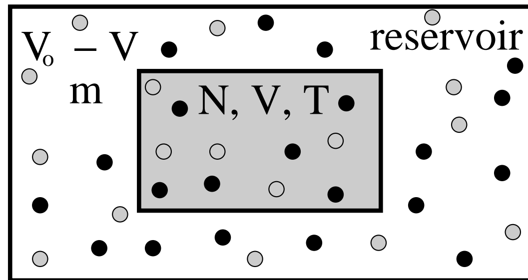

Fig. 2.2: Schematic representation of canonical ensemble. The number of particles, the volume and the temperature of the system are kept fixed, (N,V,T).

2.3 Ensembles

Statistical physics is concerned with the study of systems composed of a large number of particles, i.e. atoms, molecules, electrons, etc., and thus having many degrees of freedom. Its scope is to relate the microscopic level with the macroscopic one.

Lets say we have a classical system in equilibrium. This system is described by the Hamiltonian $H(\bar{r}^N, \bar{p}^N) = K + U$ which is the sum of the kinetic and potential energy of the particles. Here, $\bar{r}$ stands for the coordinates and $\bar{p}$ for the momenta of N particles. In this notation, the mean value of every observable quantity $A(\bar{r}^N, \bar{p}^N)$ is given by the sum over all states on the phase space with respect to the stationary probability $P(\bar{r}^N, \bar{p}^N)$:

$$\langle A \rangle = \frac{1}{h^{3N} N!} \int A(\bar{r}^N, \bar{p}^N) P(\bar{r}^N, \bar{p}^N) d\bar{r}_N d\bar{p}_N \tag{2.4}$$

where the factor h^{3N} is introduced because of the quantization of phase space while the factor N! because of the indistinguishability of identical particles.

2.3.1 Canonical ensemble - (N,V,T)

In the case of the canonical ensemble, the quantities which are kept constant are the number of particles, the volume and the temperature of the system, (N,V,T). A schematic representation of this ensemble is shown in Fig. 2.2, in which the system is sketched inside a reservoir.

The proper thermodynamic potential, whose minimum determines thermal equilibrium is the Helmholtz free energy $F = E - TS = -k_B T \ln Z(N, V, T)$. On the

other hand, the probability distribution is

$$P(\bar{r}^N, \bar{p}^N) = \frac{e^{-\beta H(\bar{r}^N, \bar{p}^N)}}{Z(N, V, T)} \tag{2.5}$$

where

$$Z(N, V, T) = \frac{1}{h^{3N} N!} \int e^{-\beta H(\bar{r}^N, \bar{p}^N)} d\bar{r}^N d\bar{p}^N \tag{2.6}$$

is called the partition function of the system, $\beta = \frac{1}{K_B T}$ and K_B is the Boltzmann factor.

Applying the above equations in Eq. 2.4 one gets:

$$\langle A \rangle = \frac{\int A(\bar{r}^N, \bar{p}^N) e^{-\beta H(\bar{r}^N, \bar{p}^N)} d\bar{r}^N d\bar{p}^N}{\int e^{-\beta H(\bar{r}^N, \bar{p}^N)} d\bar{r}^N d\bar{p}^N} \tag{2.7}$$

Note that the Hamiltonian is a quadratic function of momenta, meaning that the integrations with respect to the latter can be carried analytical. On the other hand the integration of functions $A(\bar{r}^N)$, like the potential energy $U(\bar{r}^N)$, over the configuration part of the phase space is the difficult part. In this case the integration over momenta cancel out, and Eq. 2.7 is written:

$$\langle A \rangle = \frac{\int A(\bar{r}^N) e^{-\beta U(\bar{r}^N)} d\bar{r}^N}{\int e^{-\beta U(\bar{r}^N)} d\bar{r}^N} \tag{2.8}$$

In this ensemble the acceptance probability of a trial move is:

$$P_{acc} = \min(1, e^{-\beta \Delta W}) \tag{2.9}$$

where $\Delta W = U(\bar{r}'^N) - U(\bar{r}^N)$

2.3.2 Isobaric-Isothermal Ensemble - (N,P,T)

In the Isobaric-Isothermal ensemble the number of atoms, the pressure and the temperature of the system are kept fixed, (N,P,T). In Fig. 2.3 a system in this ensemble is illustrated. Note that the volume of the system is allowed to vary. Under these conditions the thermodynamic potential which determines this system is the Gibbs free energy:

$$G = F + PV = -k_B T \ln Z(N, P, T). \tag{2.10}$$

where Z is the partition function of the system for the (N,P,T) ensemble:

$$Z(N, V, T) = \frac{1}{h^{3N} N!} \int_0^\infty dV e^{-\beta PV} \int e^{-\beta H(\bar{r}^N, \bar{p}^N)} d\bar{r}^N d\bar{p}^N \tag{2.11}$$

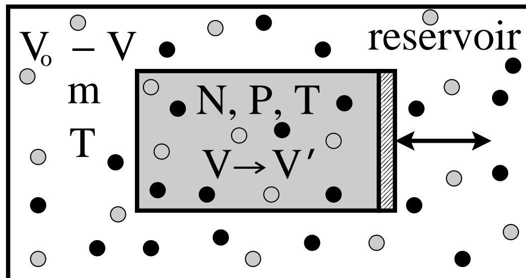

Fig. 2.3: Schematic illustration of the Isobaric-Isothermal ensemble. The number of particles, the pressure and the temperature of the system are kept fixed, (N,P,T).

In order to find the mean value of a quantity $A(\bar{r}^N, \bar{p}^N)$ we do similar calculations just as in the case of a (N,V,T) canonical ensemble. In this case we get:

$$\langle A \rangle = \frac{\int dV \int A(\bar{r}^N) e^{-\beta U(\bar{r}^N)} e^{-\beta PV} d\bar{r}^N}{\int dV e^{-\beta PV} \int e^{-\beta U(\bar{r}^N)} d\bar{r}^N} \tag{2.12}$$

In MC simulation the volume is treated as an additional coordinate. So, except of the mutual moves in particle positions, just as in the canonical ensemble, trial moves in volume are also attempted. Applying the metropolis scheme, the acceptance ratio for volume moves is:

$$P_{acc}(V \to V') = \min(1, e^{-\beta \Delta W}) \tag{2.13}$$

where

$$\Delta W = (U' - U) + P(V' - V) - N k_B T \ln(V'/V) \tag{2.14}$$

and (U′-U) is the change in potential energy due to the volume move.

2.3.3 Grand Canonical Ensemble - (μ,V,T)

Although we have not used this ensemble, it is necessary to explain its main scheme because it is the precursor of the next ensemble. In this scenario, the chemical potential of type of atoms, the volume and the temperature of the system are the fixed variables, (μ,V,T). The interesting point here is that the number of atoms change during the simulation according to the chemical potential of the species. Insertions or deletions of particles result to great energy differences that lead to very low acceptance ratios and slow convergence, especially in dense or structured systems, like crystalline solids.

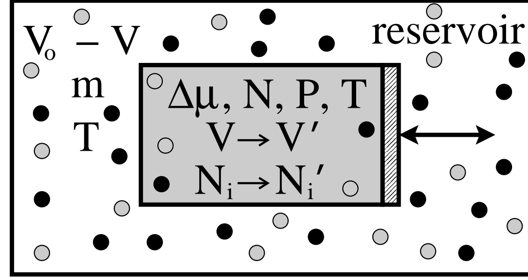

Fig. 2.4: Isobaric-Semigrand ensemble. The total number of particles, the pressure, the temperature and the differences of chemical potentials between different types of atoms are kept fixed, (N,P,T,$\Delta\mu$).

2.3.4 Isobaric-Semigrand Ensemble - (N,P,T,$\Delta\mu$)

The problems of the Grand Canonical Ensemble are overtaken using this ensemble. In this case the total number of the atoms, the pressure, the temperature and the chemical potential differences $\Delta\mu$ between deferent type of atoms are kept fixed, (N,P,T,$\Delta\mu$). In Fig. 2.4 a system with these conditions is shown. These conditions allow fluctuations Δn in the number of atoms of each species, as a result of exchanges of particles within the system, which are driven by the appropriate chemical potential differences. At the same time, we have also exchanges of volume with the reservoir, as well as the traditional MC moves, involving random atomic displacements. This ensemble can be considered as a combination of the grand canonical and the isobaric-isothermal ensemble.

In this case the thermodynamic potential whose minimum determines thermal equilibrium is the isobaric-semigrand potential:

$$Y = G - \sum_{i=1}^{n} (\mu_i - \mu_r) N_i = \mu_r N \tag{2.15}$$

where G is the Gibbs free energy, μ_i is the chemical potential of specie i from which there are N_i atoms. The total number of species is n.

The partition function for the (N,P,T,$\Delta\mu$) ensemble is:

$$Z = \int_0^\infty dV e^{-\beta PV} \frac{V^N}{N!} \sum_{identities} \prod_{i=1}^{n} e^{\beta(\mu_i - \mu_r)N_i} \int_u ds^N e^{-\beta U()} \tag{2.16}$$

Finally the acceptance probability is:

$$P_{acc}(i \rightarrow i') = \min(1, e^{-\beta \Delta W}) \tag{2.17}$$

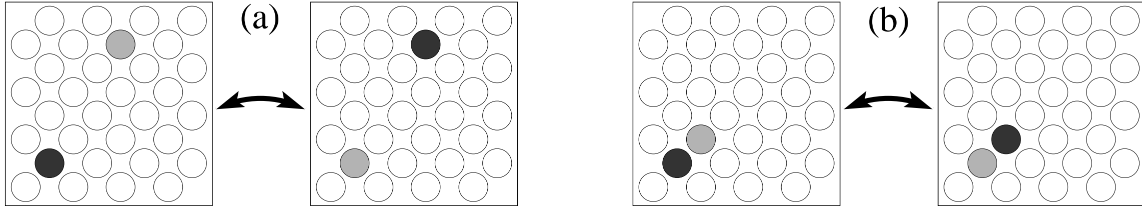

Fig. 2.5: Two different types of switching move: (a) two distant random atoms and (b) two nearest neighbors exchange identities.

where $\Delta W = (U' - U) - (\mu_{i'} - \mu_i)$, and here $(U' - U)$ is the change in potential energy due to the identity change.

In this ensemble we consider two possible types of switching moves which are visualized in Fig. 2.5. In the first type, the two atoms are chosen randomly. In the second type, which is the limiting case of the first type, we constrain the two atoms to be nearest neighbors. Obviously, equilibration is reached faster using the first type of moves, because diffusion of atoms at large distances is readily modeled. On the other hand, the second type is a more realistic representation of a diffusion event, but needs a considerably larger number of moves to diffuse an atom at large distances. By considering both types, we can test the consistency of the MC equilibration, since at the ergodic limit they ought to lead to similar island compositions. Note that we have no explicit barriers (activation energies) in the switching (exchange) moves of either type, besides the implicit barriers associated with overcoming the small size mismatch. We are currently working on the inclusion of such exchange barriers in the algorithm.

To overcome the large formation energies and diffusion barriers, especially using C, which has huge atomic size mismatch with Ge or even Si, a modification of this ensemble was introduced [5, 6]. More specifically, appropriate relaxations of first nearest-neighbor atoms accompany each attempted move. An example of an identity switch, a substitution of a Si by a C atom, is shown in Fig. 2.10. This makes the flips less costly since the exchange barriers are effectively reduced. Each nearest neighbor, k, is relaxed away or toward the central atom, 0, which changes identity, in the bond direction $\bar{r}_{0k}$. This means that every scaled coordinate s^j is altered according to the scheme:

$$\Delta s_k^j(r_{0k}^j) = A_{bond} r_{0k}^j,$$

$$A_{bond} = \frac{(b_{0k}[i'(0), i(k)] - |\bar{r}_{0k}|)\chi_{rel}}{|\bar{r}_{0k}|}$$

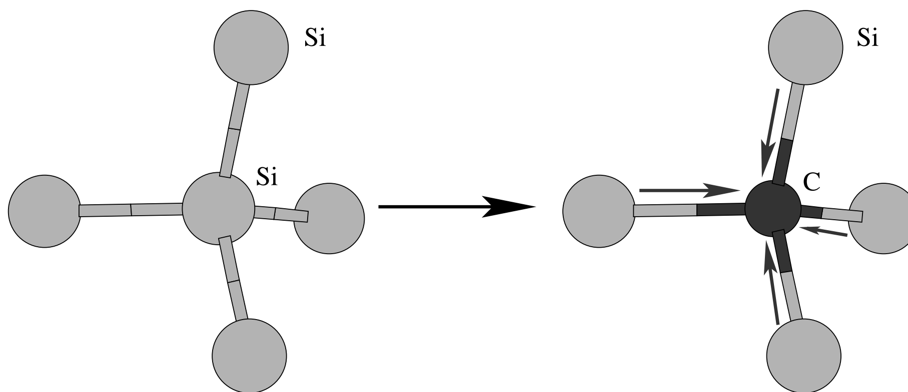

Fig. 2.6: An identity switch of a site from being Si to C, produces strained bonds. In order to make the flips less costly, appropriate relaxations of first nearest neighbor atoms are applied.

where b_{0k} is the bulk equilibrium bond length among atoms 0, after the flip, and k. The relaxation parameter χ_{rel}, ranging from 0.0 to 1.0, decides how large the relaxation should be. It is shown that intermediate values of χ_{rel} make the best effect.

2.4 The Wooten-Winer-Weaire Method

Using the Metropolis algorithm one can simulate systems in equilibrium and even experimental processes such as quenching and annealing, which are mainly used to produce amorphous networks. However, the amorphous cells constructed with these methods are not fully tetrahedral.

The structure of amorphous semiconductors is well represented by the Continoues Random Network (CRN) model introduced more than 70 years ago by Zachariasen [70]. The only requirement of this model is that each atom should satisfy fully its bonding needs. In spite of the simplicity of the model, it has turned out to be difficult to actually prepare CRN realizations of a quality comparable to that of experiment. Since then, the building of random network models for amorphous Si and Ge (and related models for SiO) has been undertaken by numerous different groups.

Such models continue to be used for a variety of calculations of physical properties. The required characteristics are the following. First, the model should contain at least several hundred atoms. This is the size of simulations at which realistic calculations can be carried out. Second, the model should conform to periodic boundary conditions. Finite clusters with free surfaces introduce problems even at the level

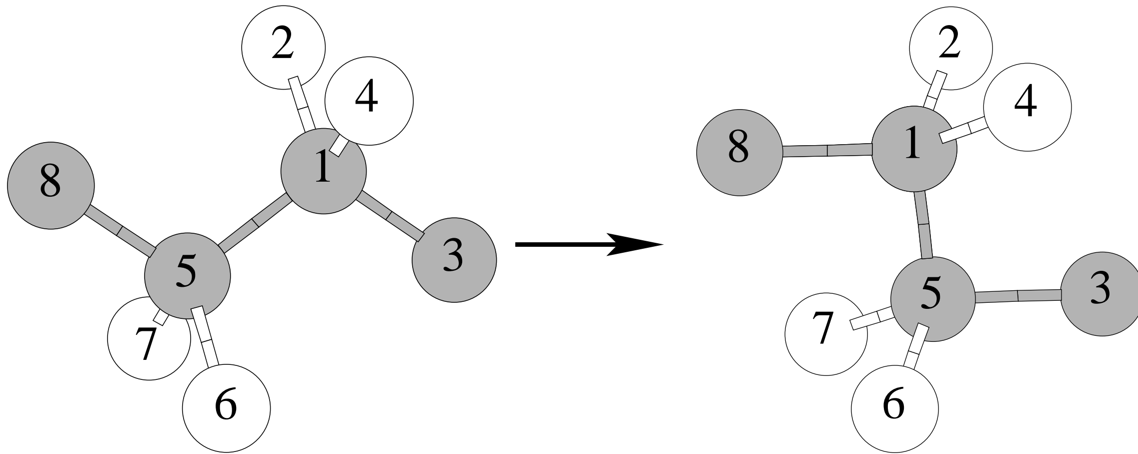

Fig. 2.7: Bond Switch move. The elementary rearrangement applied by Wooten *at al.* [74].

of structural comparisons. However, this requirement is the most problematic one. Finally, the local tetrahedral bonding should not be too glossly distorted and must agree with experimental estimates. The "ideal" CRN is defined as that with the lowest spread in the bond-length and bond-angle distributions.

A lot of models have been built trying to meet the above criteria [71, 72, 73]. However, few of them succeded to construct a novel procedure for the generation of tetrahedral random network. Today the most well accepted model is that of Wooten-Winer-Weaire, known as the WWW model.

2.4.1 Bond Switch Moves

Wooten *et al.* [74] found that one needs to introduce rearrangements that do not produce excessive bond distortion. The rearrangement which they used is shown in Fig. 2.7. The use of this simple type of move was inspired by an analogous process described by Weaire *et al.* [75]. The idea is switching two second-neighbor bonds that are parallel to each other in the perfect diamond structure and approximately so, in case of other structures. For this rearrangement, the expression "pair defect" was used, even though the word "defect" was really inappropriate.

The exact procedure is as follows. A pair of nearest-neighbor atoms are being selected (atoms 1 and 5 in Fig. 2.7). Two bonds that were to be switched were then selected at random, but following some restrictions. First, the bonds must be chosen to be as nearly parallel as possible (5-8 and 1-3). One way to ensure this criterion is

by requiring that this bonds are not members of the same 5, 6 or 7-fold ring. Also, no 4-fold rings were allowed because such rings involve large bond distortions. Of course they can be allowed in high temperature in the expectation that they would be removed during the annealing process. Finally, the bonds must not be excessively long. In practice, bond switches with bond length greater than 1.7 times the ideal bond length are rejected.

Note that the bond breaking of (1-3 and 5-8) and the bond connection (1-8 and 5-3) procedure follows a minimization of the geometrical configuration which minimizes the energy of the system. Geometric relaxation is accomplished by calculating the forces of each atom in term and then moving it to its position of equilibrium. Each atom is repositioned in term, and this process is being repeated over enough cycles, until the bond lengths converge to within 1 part in 10^4 of their final values.

By this elementary rearrangement the tetrahedral structure is conserved while bond and angle distortions are produced. Also, except of six atom rings, five and seven member rings appear. These two results are the main clues that this method will produce amorphous network with good agreement with experimental results.

2.4.2 WWW methodology

Besides this *geometrical* relaxation, there is also the *topological* relaxation. This topological relaxation is the essential process which takes place at each finite temperature. In practice, two bonds are switched at random and the energy difference between the initial and final structure is calculated $\Delta E = E_f - E_i$. If the new structure has lower structure is accepted, else it is accepted with probability $e^{-\Delta E/k_B T}$, where k_B is the Boltzmann constant and T is the temperature. This approach is of course the Metropolis algorithm [69] applied to optimization by simulated annealing.

The complete procedure introduced by WWW consists of two steps. The first one is called the "Initial Randomization" procedure. The starting structure of this model, is a supercell with the perfect diamond structure and is shown in Fig. 2.8(a). Note that the simplest and most physically appealing measure of agreement between models and experiment is a comparison of Pair Distribution Function g(r). g(r) shows the probability of finding an atom at distance r from an atom positioned at r=0, by averaging over all atoms of the lattice. For example, in the case of crystalline solids, the pair distribution function is a sum of delta functions at characteristic distances of the lattice. Each term corresponds to a coordination shell, i.e. the number of neighbors at a certain distance. This function is also shown in Fig. 2.8(a).

Then the structure is repeatedly rearranged by the elementary process of bond switch move. In the metropolis scheme this means that high temperature is applied

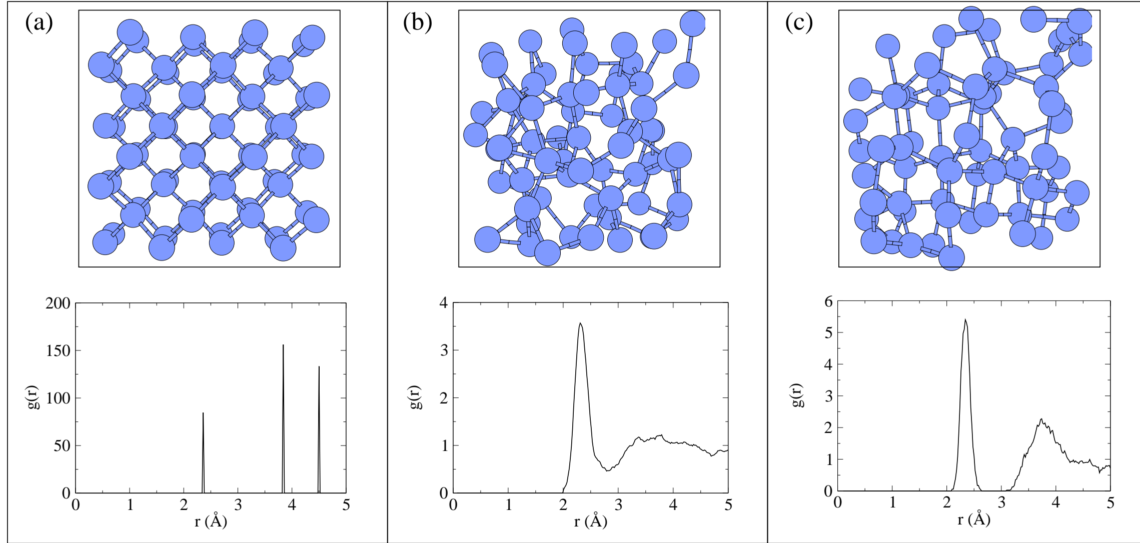

Fig. 2.8: Three snaps of the Wooten-Winer-Weaire simulation. (a) The initial supercell of crystalline Si and its pair distribution function g(r) which is consisted of delta functions. (b) The supercell at high temperature. The characteristics of a liquid structure are observed in the g(r). (c) The final structure of the simulation. Note that the third peek in g(r) is missing.

to the trial switches on the system. Progressive alteration of the diamond structure generates a sequence of increasingly distorted models. However, the process is continued until glossy distorted network with rms bond angle deviation from tetrahedral of about 22° is constructed (Fig. 2.8(b)). Note that in the pair distribution function only the first peak is present, a characteristic of a liquid structure.

The second step is the quenching procedure. Having produced a randomized but highly strained structure, it is necessary to continue with random bond switch moves in order to lower the energy. So the temperature is gradually reduced until 0.1 eV applying these topological rearrangements. The final structure then is in very good agreement with experiment. The rmd bond angle deviation from tetrahedral using the Keating potential is about 10.9°. In Fig. 2.8(c) the resulting tetrahedral network and the distribution function are shown. One of the striking deference between the distribution functions of crystalline and amorphous structure is that in the amorphous structure the third peak is missing. Also, the fourth and fifth peaks are broadened and merged into a single peak (not shown in figure).

Note that if the initial structure is not sufficiently randomized there is a possibility that the cell will return to the diamond structure. For this reason the randomization procedure stops when the rms deviation is about twice of what is required

for the amorphous network (10.9° is what experimentally found).

The initial scope of their method was to create amorphous Silicon and Germanium with periodic boundary conditions. These two systems are so similar that even the experimental distribution function of a-Si is a scaled distribution function of a-Ge. The great difference appears in systems with strong chemical order, such as SiO_2.

In the case of SiO_2, the Oxygen atoms complicate the structure. One first attempt to create a-SiO_2 was to start from the a-Si network, created for example by the WWW method, to insert between each Si-Si bond an Oxygen atom and finally to relax the structure [76]. This method is not used any more because its resulting structure does not have good agreement with experiment.

Despite the above attempt, another method is a modification of the WWW which preserves the chemical order of SiO_2 [77]. This is done by choosing the two central atoms of the switch move (1 and 5 as in Fig. 2.4) the (topologically) closest atoms of the same type, such as the two Si neighbors of an oxygen in SiO_2. Then 3 and 8 must be chosen similarly. In this way the constructed a-SiO_2 is in good agreement with experimental measurements.

2.4.3 Modifications of the WWW method

A lot of improvements for the method of WWW have been introduced since then. Some of them really speed up the calculation time, while others were practical only for rare cases. Here, we used two modifications made by Barkema and Mousseau [78] which were useful in our case. The improvements introduced are the following.

- First, the evaluation of the acceptance of the trial move using the Metropolis accept/reject procedure was done without doing full relaxation of the supercell. In order to do so, we have to decide first a threshold energy which is given by

$$E_t = E_b - k_B T \ln(s) \tag{2.18}$$

  where s is a random number between 0 and 1, E_b is the initial energy of the structure before the bond rearrangement.

  Since the energy is harmonic around the minimum, the decrease in energy obtained during further relaxation is approximately equal to the square of the force times some proportional constant c_f. So, during the relaxation the final energy can be estimated to be:

$$E_f \approx E - c_f |F|^2 \tag{2.19}$$

where E is the energy of every relaxation step. In this way, if at any moment during the relaxation, $E - c_f|F|^2$ is greater than the threshold energy E_t the trial move is rejected. We must note that the constant c_f depends on the units and the system which is applied. In our case c_f is well below 1. Also to account for unharmonicities, the moves are not rejected during the first steps of the relaxation. Using this modification a lot of computational time is gained from the moves, which are eventually rejected, producing a more efficient method.

- A local/nonlocal relaxation procedure is used. It is presumable that the atoms with large strain are those close to the bond switch. So, instead of the whole cell, the three neighbor cells are relaxed in the first few steps. In this way the force evaluation is limited gaining again a lot of computational time. In combination with the previous improvement, this makes the time per bond rearrangement almost independent of the configuration size.

2.4.4 Bond Conversion Moves

Interfaces between Si and SiO_2, such as planar interfaces or even Si-nanocrystals embedded in SiO_2, cannot compositionally equilibrate only with bond switch moves. We are thus led to introduce another type of moves, which are called bond conversion moves. This is our contribution to the development of the method. This type of moves is shown in Fig. 2.9. In this scenario a Si-Si bond is exchanged with a Si-O-Si and vise versa. Note that the number of Si and O atoms remain constant, thus we do not have to use any chemical potential. However, the method can be generalized to allow fluctuations in the number of atoms of each species (semi-grand ensemble), in order to study nucleation, clustering, expansion of nanocrystals, and other phenomena. Also, applying this type of move interdiffusion in the system is allowed to be studied.

2.5 Empirical Potentials

A good classical potential is one that with a small number of free parameters can describe a wide range of properties well and also is “transferable”. The later means that it should be able to describe properties of other states of the material than those it was fitted to.

The parameters are determined by a fitting procedure, so as to reproduce various physical quantities of the reference system. Some of the properties which are used to fit interatomic potentials are crystal structure, cohesive energy, elastic constants,

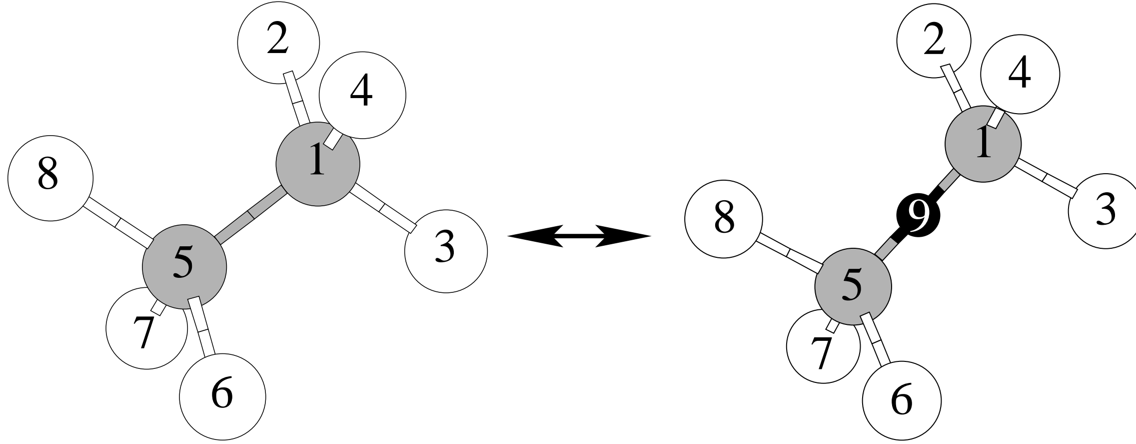

Fig. 2.9: Bond Conversion move. A Si-Si bond is converted to a Si-O-Si bond and vise versa. The total number of atoms in this way remain fixed.

equation of state P(V), neutron scattering, etc.

A classical potential can be written in the form:

$$V = \sum_{i} V_1(r_i) + \sum_{i,j} V_2(r_i, r_j) + \sum_{i,j,k} V_3(r_i, r_j, r_k) + ... \tag{2.20}$$

where

- V is the total potential energy of an N atom system. In principle all sums loop from 1 to N while in practice they can often be much reduced in order to gain computational time.

- V_1 is the single particle potential, which describes external forces (e.g. an electric field). In system with no external forces this part is 0.

- V_2 is a pair potential which only depends on the distance between atoms $r_{ij} = |\bar{r}_i - \bar{r}_j|$. Note that if there were a direct dependence on the vectors $\bar{r}_i$, $\bar{r}_j$ (and not on their difference), the potential would depend on the choice of the origin. In many cases, an environment dependence is embedded into the two-body term, as we will see later.

- V_3 is a "three-body potential" which may have an angular dependence. To preserve the independence on the atom indices, the potential has to depend only on three variables, i.e. $V_3 = V_3(r_{ij}, r_{ik}, \theta_{ijk})$.

- Four-body and even five-body potentials do exist, especially in chemical and biological applications. The potentials we are interested in are up to three-body term.

2.5.1 Tersoff Potential

The Tersoff potential [79, 80, 81] is a two body potential, which implicitly includes many body interactions (an environment dependence and no absolute minimum at the tetrahedral angle). Its form looks like the Morse potential [82]. Tersoff based his potential on the ideas presented by Abell [83] a few years earlier. The Tersoff-Abell formalism has become the basis or inspiration for a huge number of potentials developed since then. The basic philosophy is that the more neighbors an atom has, the weaker the bonds which are formed to these atoms are. This is described in potentials of the form: $V_{ij} = V_{repulsive}(r_{ij}) + b_{ijk}V_{attractive}(r_{ij})$ by constructing an environment-dependent term b$_{ijk}$ which weakens the pair interaction when the coordination number of an atom is increased.

So, the energy E, as a function of the atomic coordinates is taken to be

$$E = \sum_i E_i = \frac{1}{2}\sum_{i \neq j} V_{ij} \tag{2.21}$$

where

$$V_{ij} = f_C(r_{ij})[f_R(r_{ij}) + b_{ij} f_A(r_{ij})] \tag{2.22}$$

which is mainly consisted of tree terms. The first one f_R is a repulsive term, while the second term f_A is an attractive one.

$$f_R(r_{ij}) = A_{ij}e^{-\lambda_{ij}r_{ij}}, \qquad f_A(r_{ij}) = -B_{ij}e^{-\mu_{ij}r_{ij}} \tag{2.23}$$

The final term f_C is used as a cut off of the potential in order to speed up the computational time.

$$f_C(r_{ij}) = \begin{cases} 1, & r_{ij} < R_{ij} \\ \frac{1}{2} + \frac{1}{2}\cos[\pi(r_{ij} - R_{ij})/(S_{ij} - R_{ij})], & R_{ij} < r_{ij} < S_{ij} \\ 0, & r_{ij} > S_{ij} \end{cases} \tag{2.24}$$

The inclusion of the many body interactions appears in the parameter b_{ij}:

$$b_{ij} = \chi_{ij}(1 + \beta_i^{n_i}\zeta_{ij}^{n_i})^{-1/2n_i} \tag{2.25}$$

where $\zeta_{ij} = \sum_{k \neq i,j} f_C(r_{ik})\omega_{ik} g(\theta_{ijk})$ and $g(\theta_{ijk}) = 1 + c_i^2/d_i^2 - c_i^2/[d_i^2 + (h_i - \cos\theta_{ijk})^2]$

Here i,j, and k label the atoms of the system, r_{ij} is the length of the ij bond, and θ_{ijk} is the bond angle between bonds ij and ik. Single subscripted parameters, such as λ_i and n_i, depend only on the type of atom (C, Si or Ge). All the mixed parameters are given by the arithmetic mean $\lambda_{ij} = (\lambda_i + \lambda_j)/2$, $\mu_{ij} = (\mu_i + \mu_j)/2$ or by geometric mean $A_{ij} = (A_i A_j)^{1/2}$, $B_{ij} = (B_i B_j)^{1/2}$, $R_{ij} = (R_i R_j)^{1/2}$, $S_{ij} = (S_i S_j)^{1/2}$.

The crucial parameter, which interpolates between the elemental parameters is χ_{ij} ($\chi_{ii} = 1$, $\chi_{ij} = \chi_{ji}$). It is chosen to give correctly the enthalpy of formation ΔH of the respective ZB-structure compound. For SiC, $\chi_{SiC} = 0.98763$, fitted to $\Delta H_{SiC} = -0.33$ eV/atom. For SiGe, $\chi_{SiGe} = 1.00061$, fitted to theoretical value $\Delta H_{SiGe} = 8.9$ meV/atom [84]. For GeC there were no available data to fit, so the enthalpy if formation of this compound was defined as:

$$\Delta H_{GeC} = E(GeC) - \frac{1}{2}[E(Ge) + E(C)]$$

resulting $\Delta H_{GeC} = 0.2$ eV/atom, yielding a $\chi_{GeC} = 0.96238$ [85].

2.5.2 Stillinger-Weber Potential

The Stillinger-Weber potential [86] was initially proposed for Silicon and is a "three-body" potential. The parametrization for Germanium was suggested by Ding and Andersen [87] while for the composite system SiGe was proposed by Kelires [88].

The potential energy function is written:

$$E = \sum_{i<j} \upsilon_2(r_{ij}) + \sum_{i<j<k} \upsilon_3(\bar{r}_i, \bar{r}_j, \bar{r}_k) \tag{2.26}$$

where two body term is:

$$\upsilon_2(r_{ij}) = \epsilon_{ij} f_2(r_{ij}/\sigma_{ij}) \tag{2.27}$$

and

$$f_2(\bar{r}_{ij}) = \begin{cases} A_{ij}[B_{ij}(r_{ij}/\sigma_{ij})^{-4} - 1]\exp[(r_{ij}/\sigma_{ij} - a)^{-1}], & r_{ij}/\sigma_{ij} < a \\ 0, & otherwise \end{cases} \tag{2.28}$$

Final, the three body term:

$$\upsilon_3(\bar{r}_i, \bar{r}_j, \bar{r}_k) = \epsilon_{ijk} f_3(\bar{r}_i, \bar{r}_j, \bar{r}_k) \tag{2.29}$$

with

$$f_3(\bar{r}_i, \bar{r}_j, \bar{r}_k) = h(r_{ij}, r_{ik}, \theta_{jik}) + h(r_{ji}, r_{jk}, \theta_{ijk}) + hh(r_{ki}, r_{kj}, \theta_{ikj}),$$

$$h(r_{ij}, r_{ik}, \theta_{jik}) = \begin{cases} \lambda_{jik} e^{\gamma(r_{ij}/\sigma_{ij}-a)^{-1}+\gamma(r_{ik}/\sigma_{ik}-a)^{-1}} (\cos\theta_{jik} + \frac{1}{3})^2, & \frac{r_{ij}}{\sigma_{ij}}, \frac{r_{ik}}{\sigma_{ik}} < a \\ 0, & otherwise \end{cases}$$

Again, i,j, and k label the atoms of the system, r_{ij} is the length of the ij bond, and θ_{ijk} is the bond angle between bonds ij and ik.

Just like in the Tersoff potential, some of the mixed parameters are given as the arithmetic mean of the elemental parameters:

$$A_{ij} = (A_i A_j)^{1/2}, B_{ij} = (B_i B_j)^{1/2}, \sigma_{ij} = (\sigma_i + \sigma_j)/2,$$

or as the geometric mean:

$$\epsilon_{ij} = \chi_{ij}(\epsilon_i \epsilon_j)^{1/2},\ \epsilon_{jik} = (\epsilon_{ij}\epsilon_{ik})^{1/2},\ \lambda_{ij} = (\lambda_i \lambda_j)^{1/2},\ \lambda_{jik} = (\lambda_{ij}\lambda_{ik})^{1/2}.$$

2.5.3 Keating-like Potential

The last empirical potential which we use is a Keating-like [89]. This valence force model depends on both the positions $\{\bar{r}\}$ of the atoms and the set of bonds connecting pairs of atoms. It is a simple three body term potential and its functional form is:

$$E_{\{\bar{r}\}} = \frac{1}{2}\sum_i k_b(b_i - b_0)^2 + \frac{1}{2}\sum_{i,j} k_\theta(\cos\theta_{ij} - \cos\theta_0)^2 + \gamma\sum_{m,n}(d_2 - |\bar{r}_m - \bar{r}_n|)^3 + U$$

The first two terms represent the cost of bond-length and bond-angle distortions, respectively. The third term is used to ensure that the neighbor atoms will be included in the neighbor list and distant atoms will be excluded. So, m and n label atoms which are neither 1st nor 2nd neighbors, but for which $|\bar{r}_m - \bar{r}_n|$ is actually less than the distance $d_2 = 3.84$ Å between next-nearest neighbors in crystalline Silicon. Also, parameter $\gamma = 0.5$ eV/Å^3 [77, 61]. The term U represents a "suboxide penalty", the chemical energy cost of any suboxide taken by *ab initio* calculations [90]. Here i and j represent the ith and jth bond of the network while m and n represent atoms. The parameters of the potential are given summarized in Table 2.1.

Table 2.1: Parameters of the Keating-like potential for Silicon and Oxygen.

	k_b	b_0		k_θ		$\cos\theta_0$		U
Si-Si	9.08	2.35	Si-Si-Si	3.58	Si	-1/3	Si^{+1}	0.47
Si-O	27.0	1.60	O-Si-O	4.32	O	-1.00	Si^{+2}	0.51
			Si-Si-O	3.93			Si^{+3}	0.24

2.6 Atomic Level Stresses

Whereas a perfect crystal is stress free, deviations from the ideal lattice represent sources for internal stress, i.e. stresses which can exist without the action of external forces. Examples are vacancies and interstitials, which exist in any crystal at non-zero temperature, or dislocations produced by non-equilibrium processes such as crystallization and plastic deformation. In an amorphous material there are stresses at the atomic level because of the lack of atomic order. These atomic-level stresses are defined at any atomic position and result from the incompatibility between a given atom and its environment [91]. Define stress over an atomic volume

$$\sigma^{\alpha\beta}(i) = \frac{1}{\Omega_i} \int_{\Omega_i} \sigma^{\alpha\beta}(\bar{r} d\bar{r}) \tag{2.30}$$

while the total stress is defined as the sum over all atomic volumes:

$$\sigma^{\alpha\beta} = \sum_i \Omega_i \sigma^{\alpha\beta}(i) \tag{2.31}$$

For isotropic systems there is a more simplified way to calculate the atomic level stress. It is given using the formula [5, 6]:

$$\sigma_i = -\frac{dE_i}{dlnV} \sim p_i \Omega_i \tag{2.32}$$

where E_i is the energy of atom i, as obtained by decomposition of the total energy into atomic contributions, and V is the volume. Dividing by the appropriate atomic volume Ω_i, converts into units of pressure. Due to this definition of local stresses, a positive (negative) sign indicates compressive (tensile) stress.

2.7 Wulff Construction Method

The main parameter responsible for the shape of a material is the surface (or interfacial) tension γ. This surface tension is defined as the work required to create a unit area of interface. Surface tension may be considered to arise due to a degree of unsaturation of bonds that occurs when a molecule resides at the surface and not in the bulk. Note that the term “surface tension” is used for solid/vapour or liquid/vapour interfaces, while the term interfacial tension is more generally used for the interface between two liquids, two solids or a liquid and a solid.

In general, the surface tensions of liquids and gases are isotropic, so the lowest energy form will be the one that minimizes the surface area (hence liquid droplets/gas

bubbles are spherical). However in crystals, the surface free energy is generally anisotropic. Consequently, the equilibrium crystal shape will not generally be spherical, but can be determined by the Gibbs-Wulff theorem.

In 1878, Gibbs proposed that for the equilibrium shape of a crystal, the total surface Gibbs function of formation should be a minimum for a constant volume of crystal, i.e.:

$$d\sum_n A_n\gamma_n = \sum_n \gamma_n dA_n = 0 \tag{2.33}$$

where: A_n = area of the n-th face and γ_n = surface tension of the n-th crystal face, which is assumed constant over the whole face and independent of the crystal shape. Many years latter, Wulff (1901) [92] stated that

$$\frac{\gamma_n}{h_n} = constant = C \Rightarrow \gamma_n = Ch_n \tag{2.34}$$

where h_n is the distance from a point in the crystal known as Wulffs point. This theorem states that the thermodynamically stable crystal shape is determined when the total surface energy is minimized if the volume is constant.

Mathematically speaking the Wulff shape W_γ is given by the formula:

$$W_\gamma := \{x \in R : x \cdot n \le \gamma_n, \forall n\} \tag{2.35}$$

Note that in this construction the length scales of W_γ have units of γ. On the other hand, schematically we can construct the equilibrium shape of a crystal, very easily, using the following procedure:

- Draw vectors normal to all possible crystallographic faces $\hat{n}$ from an arbitrary point O.
- The distances m to γ_n, are marked on the vectors.
- Planes normal to the vectors are constructed through the marks.
- The resulting closed polyhedron is the equilibrium form.

An illustration of the above procedure is shown in Fig. 2.10.

2.8 First Principles Calculations

Ab initio is Latin and means literally *"out of nothing"*, although it is often translated as first principles. In physics this is used to denote calculations which

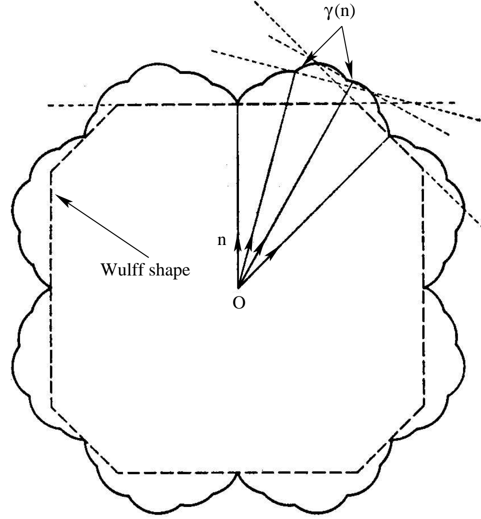

Fig. 2.10: An illustration of the Wulff construction method.

are based only on well known physical laws with no free fitting parameters. In condensed matter physics, it is used almost exclusively to mean quantum mechanical electronic structure calculations, i.e. Hartree-Fock or Density-Functional Theory (DFT) calculations. (Purists though, tend to say that DFT is not truly ab initio.)

2.8.1 The Problem

In order to predict the electronic and geometric structure of a solid, a total energy calculation is required. Minimizing that energy with respect to the electronic and ionic coordinates results in the ground state of the system.

The general non-relativistic Hamiltonian for a system of N electrons and N_I ions is:

$$H_{tot} = \sum_{I=1}^{N_I} \frac{-\hbar^2}{2m_I}\nabla_I^2 + \sum_{i=1}^{N} \frac{-\hbar^2}{2m}\nabla_i^2 +$$

$$+\frac{1}{2}\sum_{i,j=1}^{N} \frac{e^2}{|\bar{r}_i - \bar{r}_j|} + \frac{1}{2}\sum_{I,J=1}^{N_I} \frac{Z_I Z_J e^2}{|\bar{R}_I - \bar{R}_J|} + \sum_{i=1}^{N}\sum_{I=1}^{N_I} \frac{Z_I e^2}{|\bar{r}_i - \bar{R}_I|} + V_{ext}. \tag{2.36}$$

where $\bar{r}_i$ ($\bar{R}_I$) stands for the positions of the electrons i (ions I), m (m_I) denotes the mass of the electron (ion) and Z_I the atomic number of ions.

The first two terms in Eq. 2.36 represent the kinetic energy of ions and electrons

respectively, while the next three terms the interactions among them. More specifically, the third term is the electron-electron, the fourth is the ion-ion and the fifth is the electron-ion interaction. All these three terms are described by Coulomb's law. The final term is an external potential (i.e. an electric field).

Depending on the external potential, the Hamiltonian will be time dependent or not. In the case where V_{ext} does not have an explicit time dependence, the energy of the system will be a solution of the time independent Schrodinger equation:

$$H_{tot}\Psi(\bar{r}_1, ..., \bar{r}_N, \bar{R}_1, ..., \bar{R}_{N_I}) = E\Psi(\bar{r}_1, ..., \bar{r}_N, \bar{R}_1, ..., \bar{R}_{N_I}) \tag{2.37}$$

However, in order to solve this equation some approximations have to be considered.

2.8.2 Born-Oppenheimer Theory

The Born-Oppenheimer theory [93] and the adiabatic approximation are used in order to eliminate the kinetic energy of ions from Eq. 2.36. It is based on the large difference in mass between the electrons and ions and that the forces on those particles are the same. So, the electrons respond almost instantaneously to the motion of ions.

Thus the ions can be treated adiabatically. In this way the many-body problem is reduced to the solution of the dynamics of the electrons in some frozen-in configuration of ions. The total Hamiltonian is now written:

$$H_{tot} = K_I + H \tag{2.38}$$

where K_I is the kinetic potential of ions and H all the rest terms.

Despite this simplification, the many-body problem remains difficult to be solved. More approximations are needed in order for total energy calculations to be performed accurately and efficiently.

2.8.3 Density Functional Theory

The Density Functional Theory (DFT) was developed by Hohenberg and Kohn [94] and Kohn and Sham [95]. This theory maps the ground state of an interacting electron gas onto the ground state of non-interacting electrons, which experience an effective potential. Although this effective potential is not precisely known, some approximations of it work well.

The key idea of the DFT is based on the theorems of Hohenberg and Kohn. They proved that the total energy of an electron gas is a unique functional of the electron

density $n(\bar{r})$, i.e. $E[n(\bar{r})]$. Also they showed that the minimum value of the total energy functional is the ground state energy of the system, and that the density that yields that minimum value is the exact single particle ground state density $n_0(\bar{r})$.

In this notation, defining the electronic density as:

$$n(\bar{r}) = \int |\Psi(\bar{r}_1, ..., \bar{r}_N)|^2 d^3\bar{r}_1 ... d^3\bar{r}_N \tag{2.39}$$

the total energy functional can be written as:

$$E[n(\bar{r})] = T[n(\bar{r})] + \frac{e^2}{2}\int\int \frac{n(\bar{r})n(\bar{r}')}{|\bar{r}-\bar{r}'|} d^3\bar{r} d^3\bar{r}' + E_{xc}[n(\bar{r})] +$$

$$+\sum_{I=1}^{N_I} Z_I e^2 \int \frac{n(\bar{r})}{|\bar{r}-\bar{R}_I|} d^3\bar{r} + +\frac{1}{2}\sum_{I,J=1}^{N_I} \frac{Z_I Z_J e^2}{|\bar{R}_I - \bar{R}_J|} + \int n(\bar{r}) V_{ext} d^3\bar{r} \tag{2.40}$$

Where $T[n(\bar{r})]$ is the kinetic energy of electrons which is defined from:

$$T[n(\bar{r})] = \langle\Psi|\sum_{i=1}^{N} -\frac{\hbar^2}{2m}\nabla^2|\Psi\rangle \tag{2.41}$$

The exchange-correlation functional $E_{xc}[n(\bar{r})]$ is just a correction to the electrostatic integral due to electron-electron interaction:

$$\langle\Psi|\frac{1}{2}\sum_{i,j=1}^{N} \frac{e^2}{|\bar{r}_i - \bar{r}_j|}|\Psi\rangle = \frac{e^2}{2}\int\int \frac{n(\bar{r})n(\bar{r}')}{|\bar{r}-\bar{r}'|} d^3\bar{r} d^3\bar{r}' + E_{xc}[n(\bar{r})] \tag{2.42}$$

The problem is that there isn't any analytical form for the exchange-correlation energy so approximations should be made.

One year later, Kohn and Sham [95] proposed an exact method for calculating the total energy $E[n(\bar{r})]$ of a system. They proposed that instead of dealing a system with interacting electrons, non-interacting electrons moving in an effective potential should be considered. In this scheme the Kohn-Sham equation, or else the *single particle Scrödinger equation* is given by:

$$[-\frac{\hbar^2}{2m}\nabla^2 + V_{ion}(\bar{r}) + V_H(\bar{r}) + V_{xc}(\bar{r})]\Psi_i(\bar{r}) = \epsilon_i \Psi_i(\bar{r}) \tag{2.43}$$

where Ψ_i is the wave function of electronic state i, ϵ_i is the Kohn-Sham eigenvalue and V_H is the Hartree potential of the electrons:

$$V_H(\bar{r}) = \int \frac{e^2 n(\bar{r})}{|\bar{r}-\bar{r}'|} d^3\bar{r}' \tag{2.44}$$

and

$$V_{ion}(\bar{r}) = \sum_{I=1}^{N_I} \frac{Z_I e^2}{|\bar{r} - \bar{R}_I|} \tag{2.45}$$

The last term of the operator in Eq. 2.43 is the exchange-correlation potential and is given by:

$$V_{xc}(\bar{r}) = \frac{\delta E_{xc}}{\delta n(\bar{r})} \tag{2.46}$$

where in this case of non-interacting electrons their density is given by:

$$n(\bar{r}) = \sum_{i}^{N} |\Psi_i(\bar{r})|^2 \tag{2.47}$$

Note that the eigenvalues of the Kohn-Sham equation are not the energies of the single particle system but the derivatives of the total energy with respect to the occupation numbers of this states [96]. So, the highest occupied eigenvalue of a calculation is nearly the ionization energy for that system [97].

If the exchange-correlation energy functional was known, then by taking the functional derivative with respect to the electronic density would produce the exact exchange-correlation potential, Eq. 2.46. To date, there is no analytic expression for this functional but a lot of approximations exist. The most popular are the Local Density Approximation (LDA) [95] and the Generalized Gradient Approximation (GGA). [97]

2.8.4 Local Density Approximation (LDA)

In this approximation, the exchange correlation energy of an electronic system is constructed by assuming that the exchange correlation energy per electron at point $\bar{r}$ in the electron gas, $\varepsilon_{xc}(\bar{r})$, is equal to the exchange-correlation energy per electron in a homogeneous electron gas at point $\bar{r}$.

$$E_{xc}[n(r)] = \int \varepsilon_{xc}(\bar{r}) n(\bar{r}) d\bar{r} \tag{2.48}$$

and

$$\frac{\delta E_{xc}[n(\bar{r})]}{\delta n(\bar{r})} = \frac{\partial [n(\bar{r})\varepsilon_{xc}(\bar{r})]}{\partial n(\bar{r})} \tag{2.49}$$

with

$$\varepsilon_{xc}(\bar{r}) = \varepsilon_{xc}^{hom}[n(\bar{r})] \tag{2.50}$$

The values of ε_{xc}^{hom} used are based on Monte Carlo calculations of the energy of homogeneous electron gases of varying densities. Although LDA is expected to be valid only for systems with slowly varying densities, it gives reasonable results for the total energy of even polar covalent and ionic systems.

2.8.5 Generalized Gradient Approximation (GGA)

In the LDA the exchange correlation energy is approximated with a functional which depends solely on the electronic density. In the generalized gradient approximation the exchange-correlation energy depends on the magnitude and gradient of the electron density as well:

$$\varepsilon_{xc}[n(\bar{r})] = \varepsilon_{xc}^{hom}[n(\bar{r})]F[n(\bar{r})] \tag{2.51}$$

where the function $F[n(\bar{r})]$ is expressed in semiempirical way as a polynomial of the variable

$$s = \frac{|\nabla n(\bar{r})|}{n(\bar{r})^{4/3}} \tag{2.52}$$

A detailed description of the generalized gradient approximation can be found in Ref. [98]

2.8.6 Plane Waves and Pseudopotentials

A basis set for the eigenfunctions $\Psi = \sum_i \phi_i$ is necessary. The choice of the basis is a crucial parameter of this problem. Each basis has its advantages and disadvantages. The most common in use is the Plane Waves basis set.

Some of the properties, that plane waves basis set have, are:

⊕ Bloch's theorem [99], states that in case the Hamiltonian of a system is periodical, i.e. $H(\bar{r}+\bar{R}) = H(\bar{r})$ with periodicity $\bar{R}$, then its eigenvalues and eigenfunctions will be characterized by a wave number $\bar{k}$ and will be:

$$\psi_{\bar{k}}(\bar{r}+\bar{R}) = e^{i\bar{k}\bar{R}}\psi_{\bar{k}}(\bar{r}) \tag{2.53}$$

The Bloch's theorem allows a huge simplification of periodic systems. Any periodic system can be studied within its primitive unit cell and by applying periodic boundary conditions a lot of computational time is gained. Also due to this theorem, plane waves are the natural choice for the representation of electron orbitals in a periodic system.

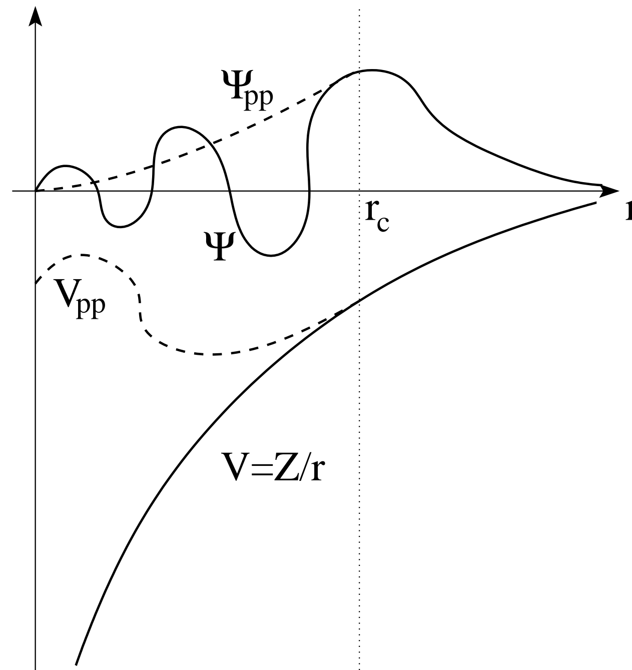

Fig. 2.11: Schematic illustration of a pseudopotential and pseudo-wave.

⊕ A plane wave is unbiased, meaning that it does not assume any preconceptions of the form of the problem.

⊕ Kinetic energy operator is diagonal in a plane wave representation, while the potential is diagonal in real space. So, the use of Fast Fourier Transform in changing between these representations provides a large saving in computational cost.

⊕ Plane waves are orthonormal and the convergence increases systematically with the number of plane-waves. On the other hand, other basis set, i.e. Gaussian basis, do not form an orthonormal set and also they do not provide a clear and systematic way to improve the convergence of the calculations.

⊖ However, the number of basis function needed to describe the atomic wavefunctions accurately near to the nucleus would be prohibitive. Thus another approximation had to be introduced. This is the representation of the potential of the ionic cores (nucleus and core electrons) with pseudopotentials.

It is well known that the physical properties of solids depend more on the valence electrons than the core ones. The idea of pseudopotentials is based on this observation. It removes the core electrons and the strong ionic potential and replaces them

with a weaker pseudopotential that acts on a set of pseudo-wave functions rather than the true valence wave functions.

In Fig. 2.11 an ionic potential, valence wave function, the corresponding pseudopotential and pseudo-wave function are illustrated schematically. The rapid ionic oscillations in the core region are due to the strong ionic potential.

The most general form of the pseudopotentials is:

$$V_{PP} = \sum_{lm} |lm\rangle V_l \langle lm| \tag{2.54}$$

where $|lm\rangle$ are the spherical harmonics characterized by l and m, and V_l is the pseudopotential for angular momentum l. V_l is an analytical polynomial function containing many fitted parameters.

The form of the pseudopotential V_{pp} should follow some rules. First of all, the V_{pp} and the ionic potential V must be identical outside the core region, and consequently the pseudo-function must be equal with the actual wave function Ψ in this region ($\bar{r} > \bar{r}_c$). Also, both Ψ_{pp} and Ψ must be continuum at $\bar{r} = \bar{r}_c$ and Ψ_{pp} to be normalized.

2.8.7 The V.A.S.P. Software

The first-principles claculations presented in this thesis were performed by using the Vienna *Ab initio* Simulation Package (VASP), based on Density Functional Theory within the Local Density and Generalized Gradient Approximations [100, 101, 102]. It was provided to our group by the Hafner-Kresse group at the University of Wien, Austria.

Using the ultrasoft Vanderbilt-type pseudopotentials [103], as supplied by G. Kresse and J. Hafner [104], the required energy cut-offs in the expansion of the wavefunction are essentially low.

Chapter 3

Bare Ge Dots

We report Monte Carlo simulations of alloying and stress relaxation in Ge/Si(100) dome and pyramidal islands. The simulated composition profiles consist of inhomogeneous Si-rich cores and outer Ge-rich shells. Comparison to experimentally deduced profiles gives us the opportunity to discuss some of the most controversial aspects of the problem. We propose that for a global interpretation of experimental results volume diffusion and stress-driven intermixing need to be considered, beside surface events and kinetically-driven alloying.

3.1 Introduction

Despite the intense investigations in recent years, the issue of intermixing/alloying in self-assembled strained semiconductor islands is far from being well understood. Consequently, its effect on the optoelectronic properties is unclear. Some of the most controversial aspects of the problem include the specific mechanisms of alloying, the relative contributions of thermodynamics and kinetics to intermixing, and its effect on the stress state of the islands.

Because it is a simple, two-element heteroepitaxial system, Ge/Si(100) has been the model case for such investigations. Recently, some experimental studies have been able to report quantitative island composition profiles [105, 106, 35, 34]. However, the results and the conclusions drawn from these studies are highly controversial. Malachias *et al.* [105] analyzed dome islands grown at 600 °C by chemical vapor deposition (CVD), using anomalous x-ray diffraction (AXRD) and selective etching. They found that the domes consist of a Si-rich core covered by a Ge-rich outer shell, and that the vertical variation of Ge content from the bottom to the top is slow. Subsequent work by the same groups [106] analyzed, in addition, dome islands

grown by molecular beam epitaxy (MBE) at 700 °C, using AXRD. They again found a Si-rich core and a Ge-rich outer shell. On the other hand, Schülli *et al.* [34] who analyzed dome islands grown at 600 °C by MBE, also using AXRD, found no evidence for a Si-rich core. The extracted vertical variation of Ge content was rapid at the bottom, with an abrupt jump from $\sim$ 10% to $\sim$ 80%, very different than in Refs. [105, 106]. Even more striking was the profile suggested by Denker *et al.* [35], which was extracted from small pyramidal islands grown by MBE at 560 °C using selective etching. Instead of a Si-rich core, they found Si-enriched corners with the center remaining rich in Ge. However, larger pyramids and domes, in the *same sample*, were heavily enriched with Si, even in the core.

These vastly different results unavoidably open up the discussion about the very fundamental processes occuring during alloying. The possibility for a variety of diffusion paths can not be excluded, because these results would otherwise be hard to reconcile. At present, it is unclear whether these experimental profiles are a result of thermodynamics or kinetics, or both, and in what degree the different experimental growth techniques influence the profiles.

The authors of Ref. [35] explained their profile using a purely kinetic model of random surface diffusion of Ge and Si atoms during growth, assuming a small diffusion length of Si atoms compared to the island base width, and excluding any strain-driven intermixing and any volume diffusion events at the basal interface in the center of an island. On the other hand, the authors of Refs. [105, 106] interpreted their profiles as a result of thermodynamics, i.e., as arising from strain-energy minimization, but they also excluded any volume diffusion events.

The scope of this work is to shed some light into this fuzzy picture, and to discuss some of the critical aspects of stress relaxation and alloying in Ge/Si(100) islands, such as the relevance of surface and volume diffusion events. We report the results of Monte Carlo (MC) simulations and the comparison of the simulated profiles with experimental ones. The MC profiles consist of a Si-rich core, though inhomogeneous, and an outer Ge-rich shell. We thus show that some of the reported experimental strain and composition profiles [105, 106] are compatible with a quasi-equilibrium model, and that volume exchange diffusion events are possible. The other profiles [35] can not just be explained by a pure kinetic model, but strain-driven intermixing needs to be considered.

The extent of atomic diffusion is a crucial factor in this problem. Often, it is argued that only surface diffusion is significant [105, 35, 107], but there are unambigious experimental indications that diffusion involves several sub-surface layers. Nakajima *et al.* convincingly showed that in the Ge/Si(100) system diffusion readily takes place down to at least the fourth sub-surface layer, even at sub-monolayer Ge

coverages and low T's [108]. This happens because of the substantial subsurface stress field due to the reconstruction [5, 6] which enhances diffusion by lowering the barriers. Calculations have shown that the diffusion barriers in the subsurface region are significantly lower ($\sim$ 1 eV) than the bulk values ($\sim$ 4 eV) [109]. This mechanism alloys the WL and the island at the initial stages of growth. Similarly, stress enhanced diffusion is expected to also operate at later stages when high stress builds up in the island [110].

We are thus led to simulate the diffusion processes in the islands by a *quasi-equilibrium* MC approach, which assumes that at high enough temperatures (this depends on the growth method), diffusion in the island, the WL, and few monolayers (ML) in the substrate is fast due to strain, leading to *local equilibrium*. Details of the method have been previously published [28, 111]. Here, we describe the central points.[1]

3.2 Simulation

Due to high barriers of diffution, molecular-dynamics methods can not reach equilibrium in practical times. Also, *ab-initio* approaches are impractical, because of the immense number of configurations needed. So, only Monte Carlo methods can achieve this goal, since they can sample over millions of compositionally distinct equilibrium configurations without tracing the actual path of the diffusing species.

We work with a fixed system composition, i.e., we assume that a given amount of Ge atoms is deposited on Si(100) and this material forms the WL and the island. The formation of the composition profile is driven by free-energy minimization. Individual contributions include the surface energy, the strain energy, the alloy mixing energy, and the configurational entropy. Energy lowering is achieved by redistributing the atoms in the system. The chemical potential remains constant for fixed composition. Under these conditions, we equilibrate the system using the isobaric-isothermal (N, P, T) ensemble, supplemented by Ising-type identity flips in the form of *mutual particle interchanges* (e.g. from Si to Ge at a certain site and *vice versa* at another site), so that the composition is kept constant [5, 6]. We constrain the two flipped atoms to be nearest neighbors, in order to realistically simulate Si-Ge exchange diffusion events. The implementation of this ensemble for MC simulations is done through the Metropolis algorithm [111]. Due to the random selection of the flipped pairs, both surface and volume diffusion events are taken into account [112].

[1] The results of this work have been published in : G. C. Hadjisavvas, and P. C. Kelires, *'Critical aspects of alloying and stress relaxation in Ge/Si(100) islands'*, Physical Review B, **72**, 075334 (2005).

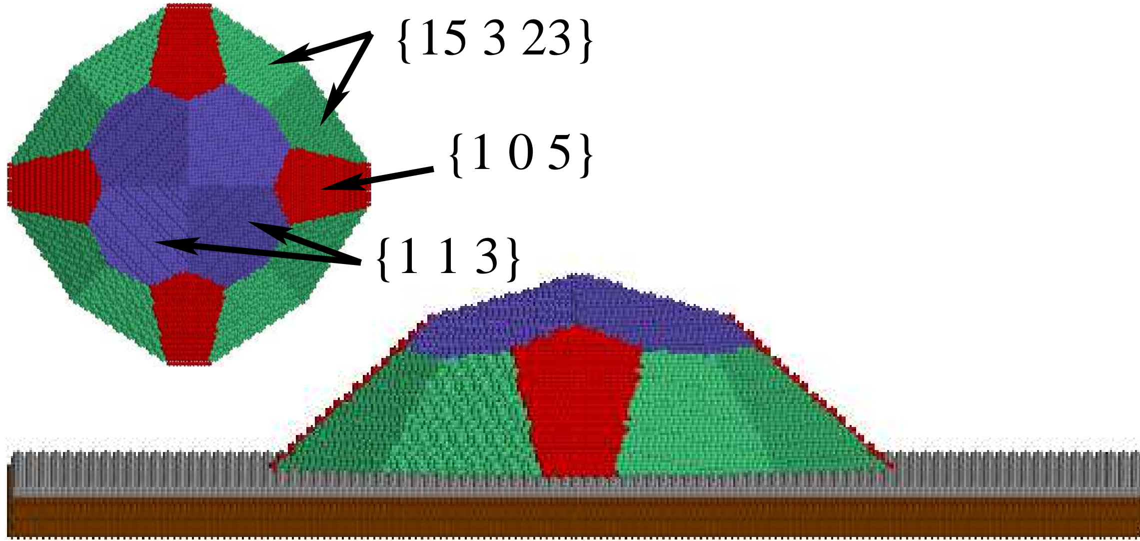

Fig. 3.1: Schematic of a multifaceted dome island used in the simulations. Different facets are shown by arrows.

For the interactions, we have used the well established interatomic potentials of Stillinger-Weber [86, 88] (SW) for multicomponent systems, which treat strain and heteronuclear bonding reasonably accurately [113]. The stress state of the islands is analyzed using the tool of atomic level hydrostatic stresses σ_i [110, 28, 114]. The stress field is mapped site by site, and the average stress $\bar{\sigma}$ in each ML in the dot, the WL, and the substrate, or over the whole island, is inferred by summing up the σ_i's. Positive (negative) sign indicates compressive (tensile) stress.

The simulational cells consist of coherent islands on top of the WL and the Si(100) substrate. We study both pyramid- and dome-shaped islands. The pyramids have a square base and {105} facets, aspect ratio (height over base width) $h/a \sim 0.1$, and contact angle $\sim 11°$. Their size is ~ 90 Å. The total amount of Ge corresponds to 3.9 ML. The domes are multifaceted, bounded by {113}, {105}, and {15 3 23} planes, and have an aspect ratio 0.2, and size 120 Å(4.8 ML of Ge). A characteristic model dome structure is sketched in Fig. 3.1. The width of the WL is fixed at 3 ML. We limit the identity switches, and thus the extent of diffusion, down to 6 ML in the substrate, to conform with experimental observations. The substrate contains 10 ML of Si atoms, with the bottom layer kept fixed. Epitaxial strain is imposed by constraining laterally the cells to the Si lattice dimensions. Periodic boundary conditions are imposed in the lateral directions.

3.3 Results

In the next subsections, the results, of the above simulations, will be presented. First the stress profiles of the non-alloyed domes is shown. Next, the resulting composition profiles, both a lateral site-by-site profile and a vertical variation of Ge content are extracted. Finally, the stress profiles of the alloyed structures, and its comparison with the non-alloyed case, which reveal the strain relief imposed by the diffusion, will be discussed in the last subsection.

3.3.1 Stress profiles of non-alloyed domes

We begin with the analysis of the stress field in non-alloyed Ge islands [110, 28, 21, 24]. This corresponds to experimental situations where intermixing is either negligible (relatively low growth temperatures) or it is not yet initiated (the stress is below a critical compressive value [110]).

The stress pattern of a typical non-alloyed dome island is analyzed in Fig. 3.2. In the upper panel, the x dependence of the stress in the island base layer and the top substrate Si layer is plotted. In the lower panel, a stress map of the whole structure is portrayed. Stresses are overwhelmingly compressive in the interior of the island, but at the edges become tensile. Compression fades as we move upwards to the top. An interesting feature, found also by Sonnet and Kelires [28] and Yu and Madhukar [21] in pyramidal islands, is a highly compressed region near, but not at, the island edges. In conjunction with the well known [110, 21, 24] formation of a compressive corral in the WL and in the substrate at the island periphery - see the variation in the top substrate layer - this feature bears significance for the discussion on alloying that follows. Outside the corral, stresses in the substrate below the island are tensile.

3.3.2 Composition profiles of alloyed domes

At the initial stages of growth, stress in the island and the compressive corral is low [110]. When stress sufficiently builds up, in a manner exemplified in the pattern of Fig. 3.2, strain-driven intermixing and alloying is activated. (Possible kinetic mechanisms are discussed below.) To simulate the effect, MC switcing-exchange moves are performed over the runs, yielding at the ergodic limit average site occupancies. These denote the local compositions, and thus the composition profiles are mapped.

The overall composition profiles in the island can be easily extracted using the methodology explained above. More specifically, by calculating an average value

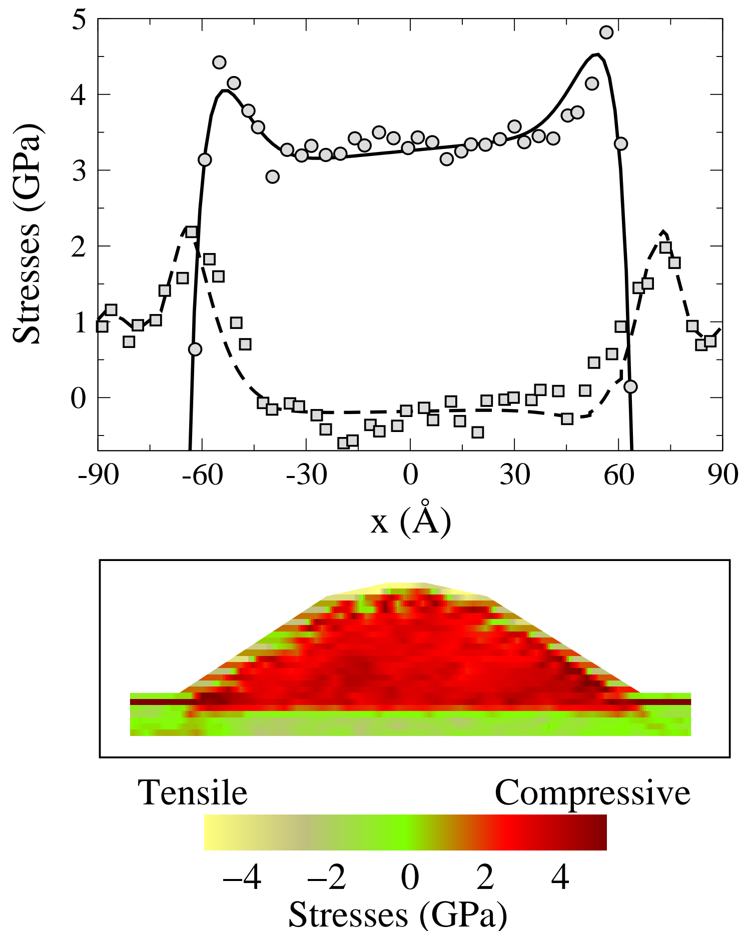

Fig. 3.2: Top panel: Variation of hydrostatic stress in the base layer (circles, solid line) of a non-alloyed dome and in the top substrate layer (squares, dashed line), along a line passing through the island base center. Bottom panel: Stress map of the dome island. A thin slice cut through its center is shown.

within each layer, in the quantum dot, the vertical variation of the Ge content as a function of the ML number, can be extracted. This variation is shown in Fig. 3.3, where zero is the base of the dome. Note that is is near parabolic. Thus, the Ge content is slowly varying in the bottom and rapidly varying when approaching the top of the island. This behaviour is valid in all cases studied, either domes or islands.

The opposite varriation is found experimentally in dislocated islands [33]. They found that the Ge fraction increases rapidly in the bottom and remains nearly constant at the top. This discrepancy might be due to the neglect, in the experimental analysis, of the lateral variation of composition. Often is assumed a constant lateral composition, which of course affects the outcome for the vartical variation. The

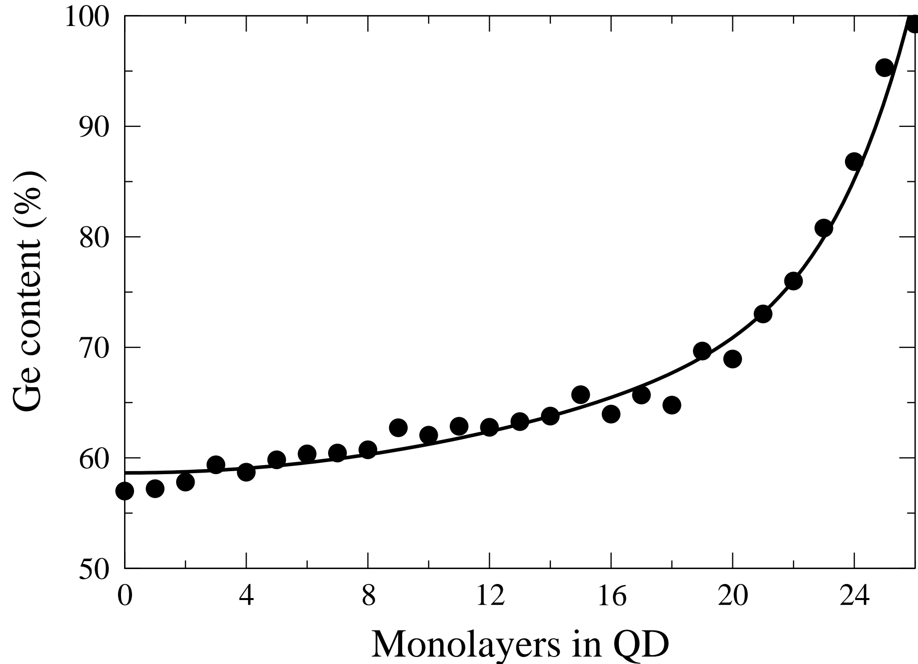

Fig. 3.3: Vertical variation of Ge content in the intermixed island. Solid line is a guide to the eye.

latteral variation, of such systems, has been shown by Sonnet and Kelires [28].

Characteristic composition profiles of a pyramid and a dome, calculated at 900 K, are shown in Fig. 3.4. It is clear that in both cases the profile is partitioned into two distinct regions. An inner region enriched with Si and an outer Ge-rich shell, which covers the islands from the base up to the top. The Si-rich area (Si fraction more than 40%) is not homogeneous, but there are clusters of sites with higher Ge propabilities dispersed in this core. This means that the strain-energy term overwhelms the alloy mixing and configurational terms which favor randomness. It is also evident that the highly compressed regions near the island edges (in the non-alloyed state, see Fig. 3.4) are now enriched with Si. This is because sites under compression (tension) tend to be occupied by the smaller (larger) species in the system [5, 6]. Such subtle features were also observed in simulations of pyramids using the Tersoff potential [28]. On the other hand, the formation of the Ge-rich outer shell can mainly be attributed to the lower surface energy of Ge [28, 106], but also to the tensile conditions prevailing at the edges.

It is striking that these MC composition profiles, simulated under quasi-equilibrium conditions, are similar in general lines to the experimental profiles in Refs. [105, 106]. We may interpret this similarity as implying that the latter profiles

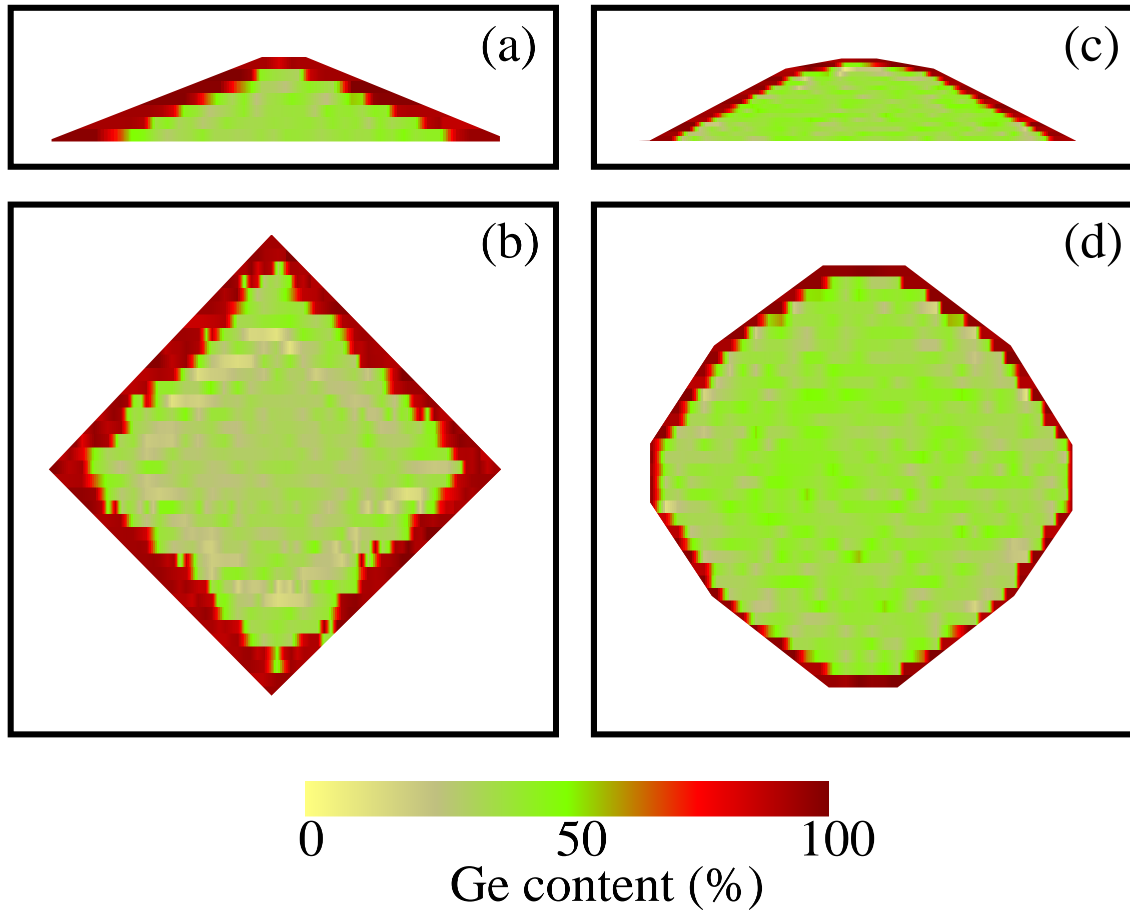

Fig. 3.4: Composition profiles in a pyramidal (left) and a dome island (right). Panels (a), (c) portray thin slice cuts through the center of the islands. Panels (b), (d) show the base layers.

are formed under conditions of strain-enhanced diffusion, including Si-Ge volume exchanges at the central basal region of the island. This mechanism readily explains the formation of a Si-rich core. Indeed, there is no reason to exclude such events, either at the initial stages of growth or at later stages when high stress accumulates in the island. In both cases, barriers are low (see above.)

Exchanges are also expected between the Si-enriched corral in the WL and the compressed regions in the island *near the edges.* These should also be considered as volume diffusion events. True surface events, i.e., Si atoms diffusing on the terrace and attaching to the edges, intruding then into the island, may contribute to alloying. However, they should not be so favorable because the edges are under tension [28, 21], and there is a barrier to cross over them. Note that, as a rule, intermixing reduces high elastic energy, arising from either compression or tension, but the actual composition depends on the sign of the stress state.

An alternative explanation for the generation of the Si-rich core was given in Ref. [105]. It says that stress relief is achieved by Si-Ge alloying of the island edges through the compressive corral by means of surface diffusion [106]. The alloyed regions are continuously buried under newly deposited Ge, as the edges move radially outward, giving rise to the Si-rich core. This is a plausible scenario, but there are some difficulties with it. (a) Edges are under tension. So, volume exchanges with the compressed near-edge region are more likely. (b) Even in this case, volume exchanges with central regions are also likely, as argued above, since the stress difference between the two regions is small (see Fig. 2). (c) Then, the notion of buried alloyed regions at the edges is redundant to explain the Si-rich core.

On the other hand, the kinetic model in Ref. [35] seems to explain the cross-like shape of the profile in small pyramids, but it does not account for the profiles in larger pyramids and domes, grown in the same sample, with the same method at the same T. The model is proposed to hold during growth. Then, since larger pyramids obviously develop from smaller ones, and domes are well known to develop from pyramids through facet transformations [115], one would expect to see larger pyramids and domes with Si-depleted cores (which are frozen in as further material is deposited). This is not seen in the experiment. The model does not account for the dome profiles in Refs. [105, 106], either.

Therefore, a pure kinetic model is inadequate for a global description. Instead, the profiles in Ref. [35] can be explained by also considering strain-driven alloying. In smaller pyramids, under limited diffusion (MBE growth, 560 °C), the most compressed areas, near the edges, are alloyed. Coupled to kinetic and geometrical factors, which are significant under conditions of low diffusivity, this favors Si enrichment at the corners. However, when pyramids grow larger or transform into domes,

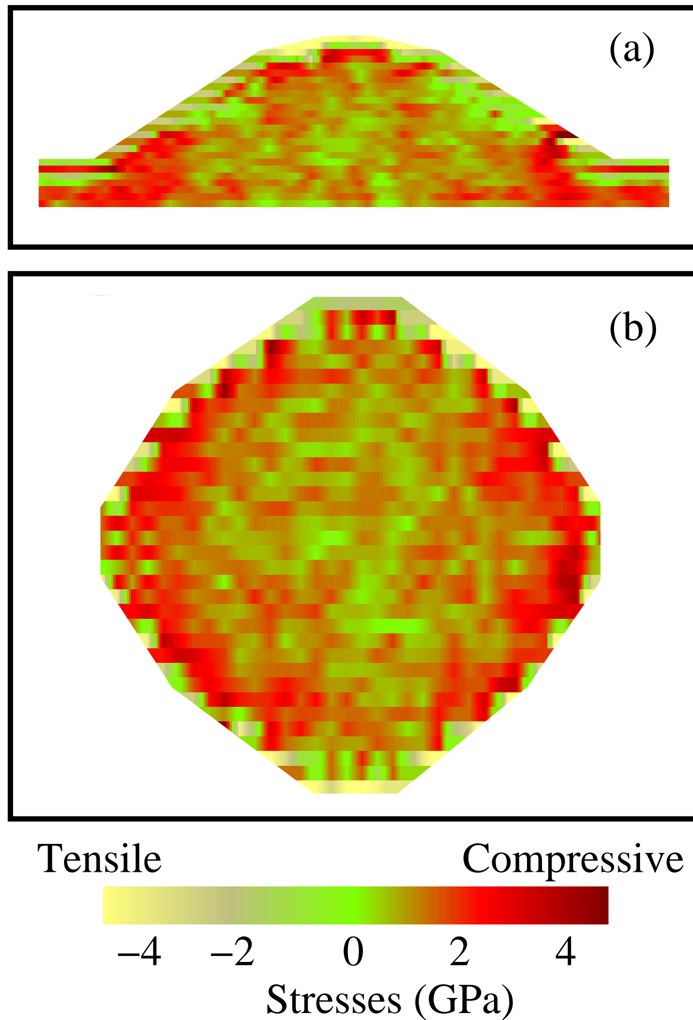

Fig. 3.5: Stress maps of an alloyed dome. (a) The whole cell. (b) The dome base layer.

high stress builds up in the interior. Now, strain-enhanced diffusion overwhelms kinetic contributions, and the cross-like shape disappears. Volume diffusion events, both near the edges and at the center, are triggered leading to extensive intermixing. Of course, strain-enhanced diffusion sets in from the onset at near equilibrium conditions. This requires high T's to activate volume events, as in Ref. [106] (MBE growth, 700 °C). Alternatively, CVD growth may provide such conditions, at even lower T's, as in Ref. [105].

3.3.3 Stress profiles of alloyed domes

Finally, we discuss the stress state of the alloyed domes. Fig. 3.5 shows the stress map of the dome shown also in Fig. 3.2 before alloying. Comparison of the two maps reveals that much of the compression in the island is relieved, especially in the core, but elastic energy still is stored in the compressive ring near the edges, and in the corral below. Thus, further annealing would alloy these regions. The map is very similar to the stress maps of alloyed islands reported in Ref. [106]. This is another indication that in these experiments near-equilibrium conditions might have been achieved.

3.4 Conclusions

In summary, our MC simulations provided stress and composition maps in Ge/Si (100) islands, whose comparison to experimental profiles, generated with different methods and deposition conditions, allowed us to discuss some of the most contoversial issues in this subject. We proposed that, beside surface diffusion, volume exchange events may play a role in shaping up the composition profiles, and that stress-driven intermixing is needed for the global interpretation of experimental results.

Chapter 4

Carbon-induced Ge Dots on Si(100)

Monte Carlo simulations shed light onto the stress field and composition of C-induced Ge islands on Si(100). It is shown that the dots do not contain C, under any conditions of temperature and coverage, but have a gradual composition profile from SiGe at the bottom to Ge at the apex. The average compressive stress in the islands is considerably reduced, compared to the pure Ge/Si case. At low Ge coverage, the terrace around the dots is enriched with Si-C dimers. At high Ge contents, Ge wets the surface and covers the pre-deposited C geometries. We predict enhancement of Ge content in the islands upon C incorporation.

4.1 Introduction

Ge islands formed on a Si(100) surface, which is precovered with a small amount of C, are a special and important class of Si-based nanostructures. They are fabricated by molecular-beam epitaxy [116, 117, 118, 119] and attracted interest because they are remarkably small, typical sizes are 10-15 nm in diameter and 1-2 nm in height, and exhibit intense photoluminescence (PL) [117]. The growth of these islands proceeds without the formation of a wetting layer (Volmer-Weber mode), contrary to the islands grown on bare Si(100) which follow the Stranski-Krastanov growth mode. This is attributed to the predeposited C atoms. Their small size reduces the lattice constant of the alloyed Si surface and exaggerates the mismatch with the Ge overlayer. In addition, C atoms modify the surface and interface energetics.

Since C atoms play such a vital role, it is essential to know how they are dis-

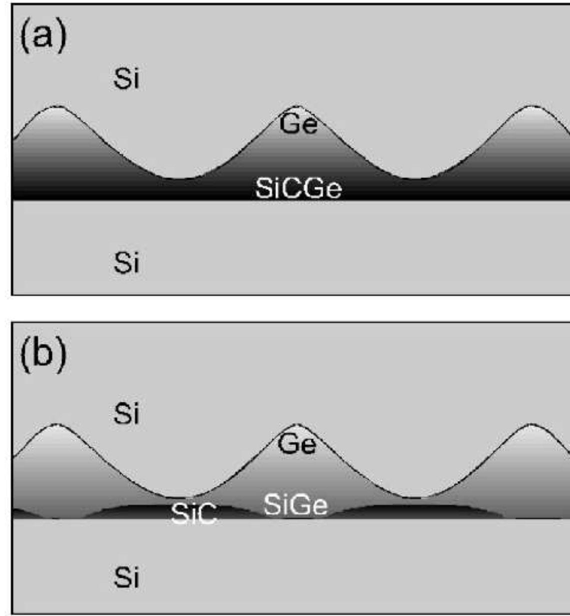

Fig. 4.1: Scheme of spatial dot compositions. (a) is taken from Ref. [117] while (b) is derived in Ref. [119].

tributed in the surface region, and especially whether they occupy sites in and below the dots. The interpretation of PL data strongly depends on this information, but the issue is controversial. There have been two different models drawn from experimental work. In the work of Schmidt and Eberl [117], the PL data were interpreted as suggesting that the dots have a gradual composition profile from homogeneous SiGeC below and at the bottom to pure Ge towards their apex. A schematic drawing of the dot composition is given in Fig. 4.1(a). On the other hand, Grützmacher and collaborators [119] interpreted their STM images as suggesting that the dots are free of C, have a gradual composition profile from SiGe at the bottom to Ge at the apex, and are located between C-rich patches. An idealized scheme of the material composition is shown in Fig. 4.1(b)

The scope of this work is to resolve the controversy and offer a theoretical answer to the problem. Through Monte Carlo (MC) simulations, we extract the stress fields and the associated composition profiles in small pyramidal islands and the surrounding surface region, at typical growth temperatures and for various carbon contents. Our results indicate that the Grützmacher model is more plausible. We predict enhancement of Ge content in the islands, compared to the carbon-free case. The stress pattern in the dots is different from the bare Ge/Si profile.[1]

[1] The results of this work have been published in : G. Hadjisavvas, Ph. Sonnet. and P. C. Kelires,

4.2 Simulation

The simulations are based on a *biased* MC algorithm, within the semigrand canonical ensemble, devised by Kelires to deal with C incorporation in the Si, Ge, and SiGe lattices, or with any case where large size-mismatch exists between the constituent atoms (For details see Ref. [85]). The characteristic MC moves in this algorithm are Ising-type identity flips. These moves attemp to change the identity of a randomly chosen atom into one of the other possible identities in the system, and are driven by the applied chemical-potential differences. To lower the high energy barriers associated with the identity conversion of a site into or from being C, appropriate relaxations of the bonds involving the specific site accompany the attempted switch. The usual MC moves, i.e., the random atomic displacements and volume changes, ensure full relaxation of the network.

In order to model the interactions and make the simulations tractable, we use the well established interatomic potentials of Tersoff for multicomponent systems [81], extended by Kelires to treat the ternary SiGeC system [85]. These potentials have been used with success in similar contexts [6]. In particular, bonding and strain fields induced by the surface reconstruction are accurately described, and various predictions made about C interactions and stress compensation are verified experimentally.

To model the experimental conditions as much as possible, we first "predeposit" C atoms in the Si(100) surface by the incorporation process described above, at various sub-monolayer coverages and at 900 K. The Si substrate in our simulational cell contains 9 monolayers (ML) 200 Å $\times$ 200 Å wide. The bottom layer is kept fixed throughout the simulation. The cell is constrained to have laterally the Si lattice dimensions, with relaxation occuring vertically. Periodic boundary conditions are imposed in the lateral directions.

It is now well established that C induces the $c(4 \times 4)$ reconstruction of the surface, although its structure is still a matter of debate [118, 120, 121]. At low coverages, the surface is partly covered with the $c(4 \times 4)$ configurations involving C atoms, while the rest retains the (2×1) symmetry. It has been shown by the experimental work of Leifeld *et al.* [119] that Ge dots nucleate on such C-free areas. The theoretical argument to support this originates from the work of Kelires who unraveled a repulsive interaction between Ge and C atoms in the Si lattice [85]. To conform with this experimental observation, we do not allow incorporation of C in the central portion of the surface in our simulational cell, producing so a C-free area. In the C-containing region, the dominant structures are Si-C dimers on the

---

'Stress and composition of C-induced Ge dots on Si(100)', Physical Review B, **67**, 241302(R) (2003).

terrace and C atoms in the third and fourth sub-surface layers, at sites below the surface dimers. These are believed to be the main configurations in the $c(4 \times 4)$ reconstruction at low C contents [120, 121]. To investigate the effect of the amount of C predeposited, we generate cells with 0.16 and 0.36 ML C coverage by varying the C chemical potential.

In the second stage, we form a coherent pure Ge island on top of the C-free area. The dot has a pyramidal shape with a square base and $\{105\}$ facets, and is oriented at an angle of 45° with respect to the dimer rows of the surface [3]. The dot contains 1750 atoms arranged in 7 ML. The base width is $\sim$ 92 Å. Typically, C-induced dots seen in experiment have similar dimensions. The amount of Ge in the cell is equivalent to $\sim$ 0.5 ML. With such Ge coverage, the model simulates islands produced by experiment at low substrate temperatures ($\sim$ 625 K), at which no Ge wetting layer is formed on the terrace [119].

4.3 Results

4.3.1 Stress profile on non-alloyed islands

We analyze the stress state of this initial configuration by invoking as a probe the concept of atomic level stresses σ_i, as in the previous chapter on bare Ge/Si islands. It comes out from this analysis that, in the presence of C, the stress pattern deviates significantly from the bare Ge/Si case. This is demonstrated in Fig. 4.2. It is clear that the overall compressive stress in the dot is significantly reduced under the influence of C, and that this reduction is enhanced as the amount of predeposited C increases. The average stress in the dot $\bar{\sigma}_{QD}$ for the bare case is 1.4 GPa/atom [122]. For 0.16 ML C, $\bar{\sigma}_{QD} = 0.45$ GPa/atom, while for 0.36 ML C, $\bar{\sigma}_{QD} = 0.27$ GPa/atom. In the substrate, tensile conditions prevail, especially on the terrace, because the C atoms experience large local tensile stresses. This is partly compensated in the first subsurface layer where the surface reconstruction induces compressive conditions [5, 6].

The most noticeable change due to C is observed in the bottom layer of the dot. It is found to be under slight tension, contrary to the bare case in which this layer is very compressed. The effect originates from certain Ge atoms which are under excessive tensile stress. As demonstrated in Fig. 4.3, which portrays the probability distribution of stresses $P(\sigma)$ in the layer, the most probable (peak) value still is on the compressive side, but the long tail of highly stretched atoms is overwhelming, giving a mean value on the tensile side.

To get more insight into this effect, we resort to the site by site analysis of the

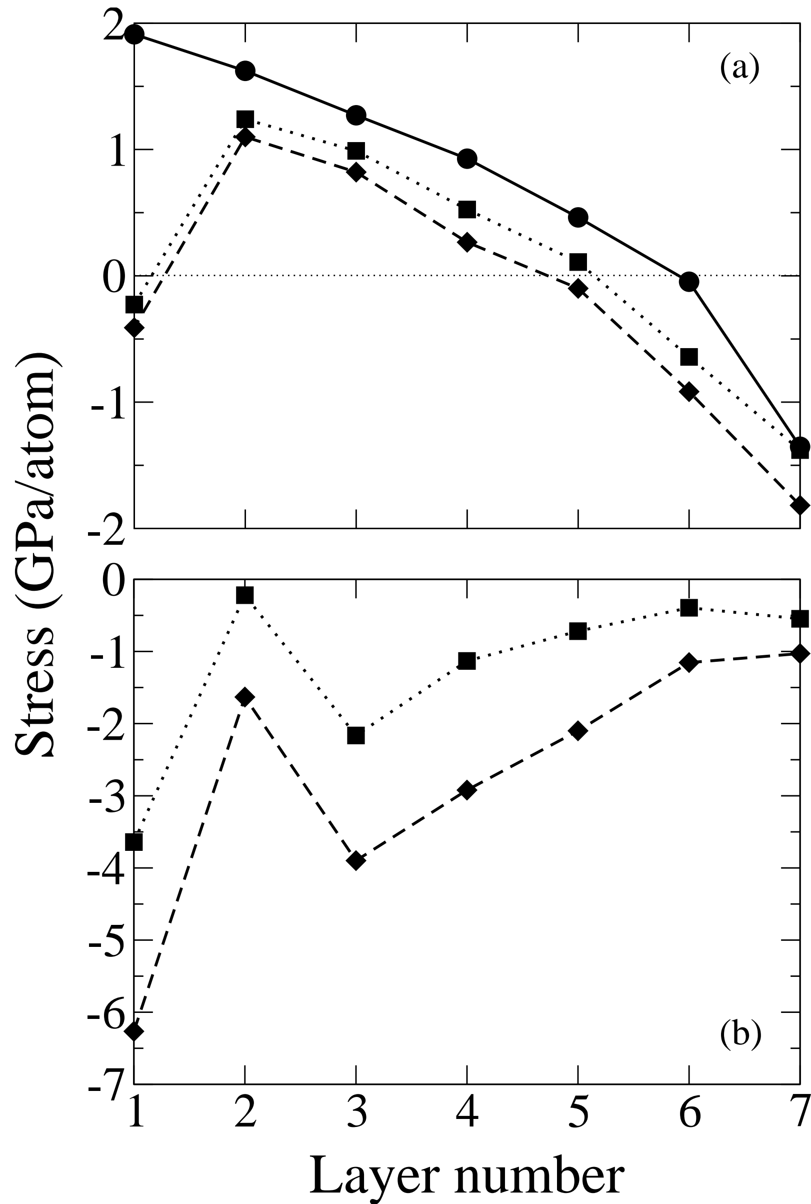

Fig. 4.2: Variations of average stress layer-by-layer in (a) the dot and (b) the substrate at 625 K. Layere numbered 1 denotes the base in the dot and the top layer in the substrate. Squares (diamonds) show variation in cell with 0.16 (0.36) ML C. As a reference, the bare variation in the dot is also shown (circles). Positive (negative) sign indicates compressive (tensile) stress.

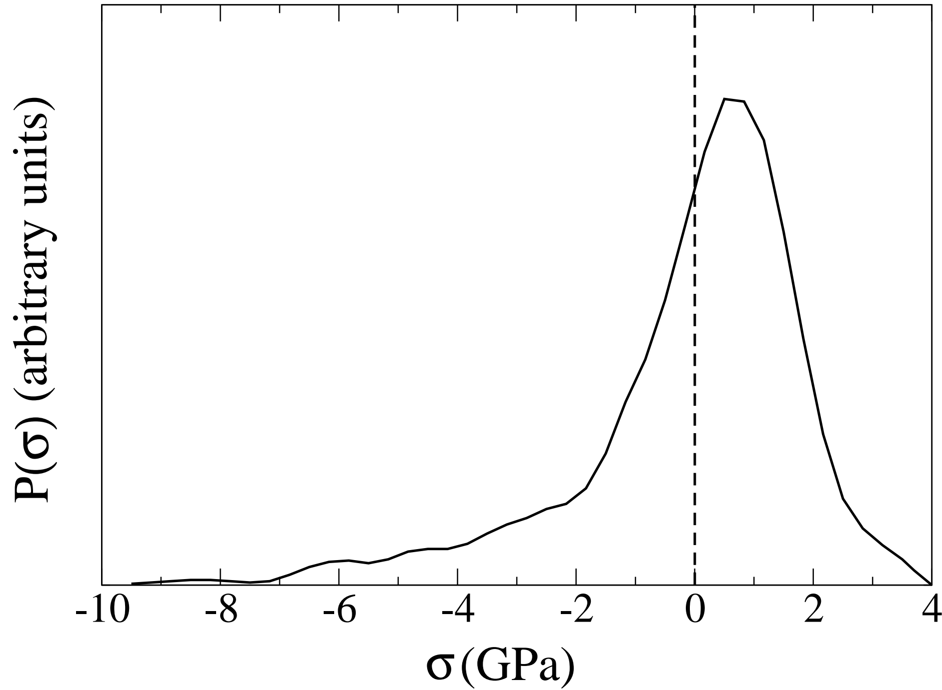

Fig. 4.3: Probability distribution of stresses in the base layer of the dot. Sign of stress as in Fig. 4.2.

stress pattern. This is illustrated in Fig. 4.4 for selected layers of the cell with 0.16 ML C content. It is clearly shown that a large number of Ge atoms in the base layer of the dot are under tension, not only at the periphery but also in regions inside, while the central region is compressed. In the bare case [122], only the peripheral Ge atoms are under tension. We can think of this effect as a "dragging out" of the exterior regions of the base layer to conform with the contracted surrounding lattice due to C incorporation. The effect considerably weakens in the second layer, which is mostly under compression (but still lower than in the bare case.) On the terrace, tensile stresses dominate around the dot, but the region just below the dot is mostly compressed as in the base dot layer. The first sub-surface layer exhibits regions of tensile stress, especially under the dot. This compensates for the compression above on the terrace and the base layer.

4.3.2 Composition profiles of alloyed islands

At higher temperatures ($\sim$ 800 K), intermixing of Ge with C in the Si-C areas, which was initially inhibited due to the Ge–C repulsion, is believed to take place [119]. To address this possibility and obtain the appropriate for high T's equilib-

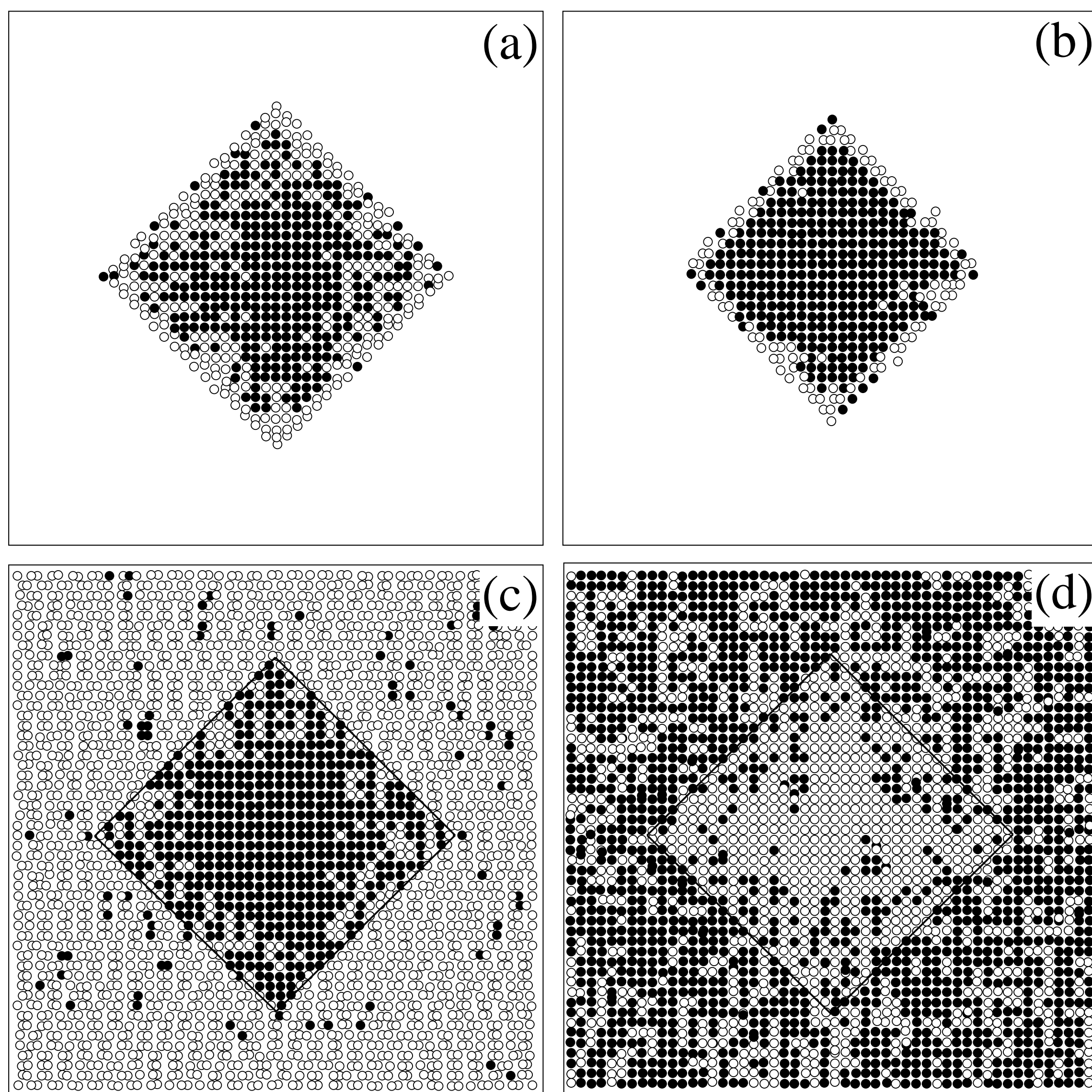

Fig. 4.4: Atomic sites shaded according to their local stress. Filled spheres, compressive; open spheres, tensile. (a) Base dot layer. (b) Second dot layer. (c) Top substrate layer. (d) Second substrate layer. Solid lines (guide to the eye) enclose the areas below the island.

rium distribution of species, the initial configuration is further relaxed at 800 K by interdiffusion. To model this, a pair of dissimilar atoms is chosen randomly and an attempt is made to switch their identity. At the ergodic limit of many thousands attempted flips per site, the *average* site occupancies are calculated, one for each species. These are compared to the respective *random* occupancies, which would be the result of a random distribution of atoms on the lattice sites, in order to infer the average identity of each site, i.e., the overwhelming occupancy.

The application of this analysis to the cell with 0.36 ML C content is shown in Fig. 4.5, for selected layers. The atoms are shaded according to their average identity. The outstanding feature revealed in these graphs is the complete absence of carbon from the dot layers (only the bottom two are shown). We repeated the simulation for an even higher T (1000 K), to increase further the acceptance of flipping moves, and found the same result. We can point out two factors responsible for this: (a) C has to break Ge-Ge bonds in the dot and form instead Ge-C bonds, which are unstable as we said. (b) The compressive stress in the dot is better compensated by the segregation of Si, rather than C. The latter would induce tensile conditions. So, Si atoms diffuse into the island, while Ge atoms outdiffuse from the interior to wet the terrace due to their low surface energy, mostly forming Ge-Ge dimers and few Ge-Si dimers. C atoms on the terrace are solely involved in Si-C dimers.

Interestingly, the areas on the terrace and in deeper layers, which are underneath the island base, also remain free of carbon after the redistribution of species. Note that the Ge and Si composition profiles in the island are quite similar to the respective profiles in the bare Ge/Si case [122]. Si atoms enrich the bottom layers, mainly in the central regions. This is consistent with the compressive conditions shown in Fig. 4.4. The Ge content is slowly varying in the bottom and rapidly varying when approaching the top of the island (Fig. 3.3). Taking all these observations into account, we conclude that there is no evidence for SiGeC alloying in the dot or below, and that our theoretical model is in general lines consistent with the experimental model of Grützmacher.

It is reported that at higher Ge coverages the C-induced dots show improved PL [117, 123]. We therefore investigated the distribution of species in this important case. We start with a configuration where Ge fully wets the terrace, covering the predeposited C-rich areas surrounding the island, as is done in experiment. This is equivalent to 1.6 ML Ge coverage. Then, the structure is equilibrated and relaxed by intermixing at 800 K. Again, we find that the dot remains free of C. But most importantly, the terrace is as well free of C, and the layer below contains a very small amount of it. Instead, C content is maximized in the third layer. This is clearly demonstrated in Fig. 4.6, which compares this case with the C profile for 0.5

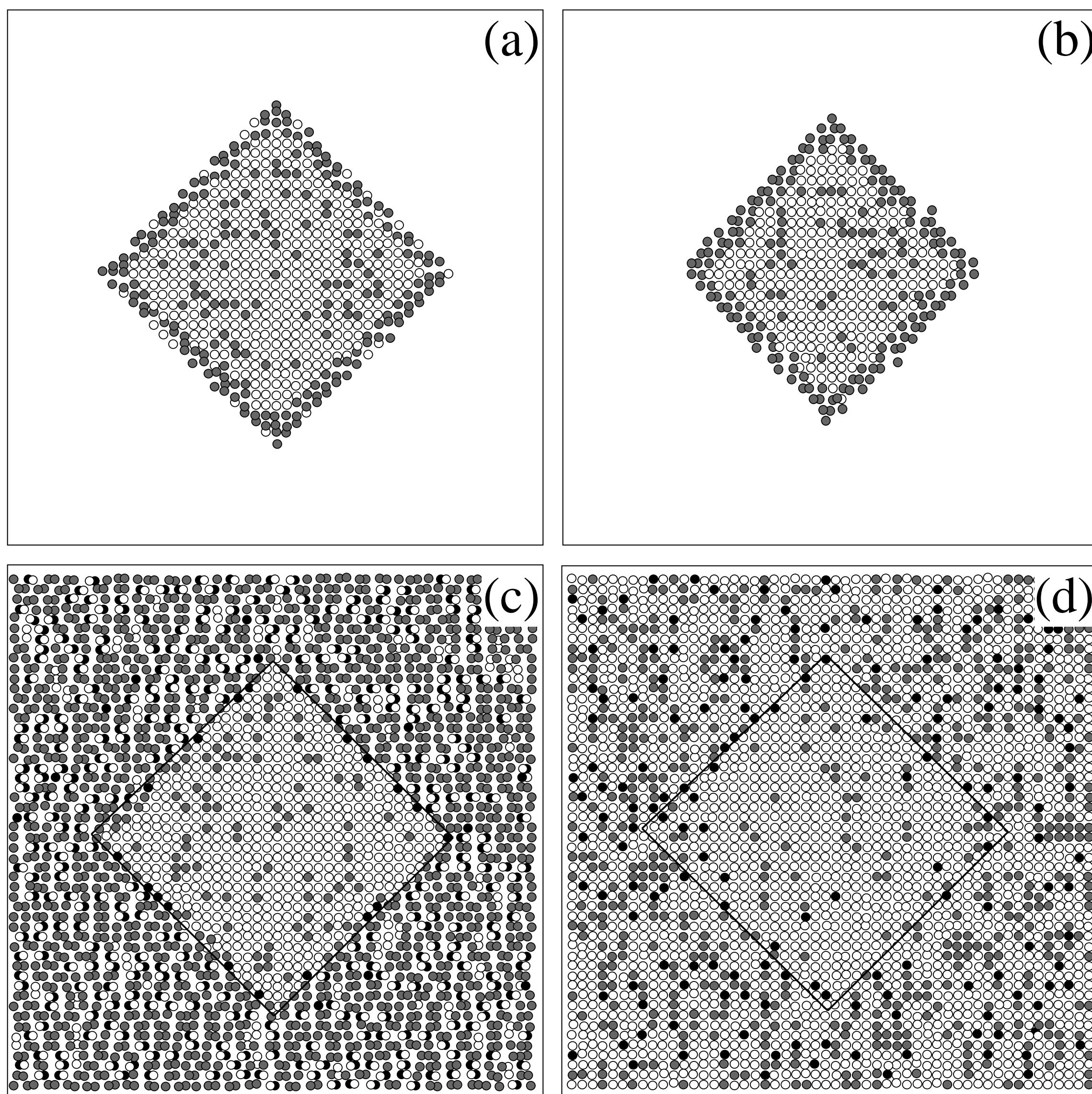

Fig. 4.5: Atomic sites shaded according to their average accupancy. Open spheres show Si atoms, gray spheres denote Ge atoms, and black spheres show C atoms. (a) Base dot layer. (b) Second dot layer. (c) Top substrate layer. (d) Third substrate layer. Solid lines (guide to the eye) enclose the areas below the island.

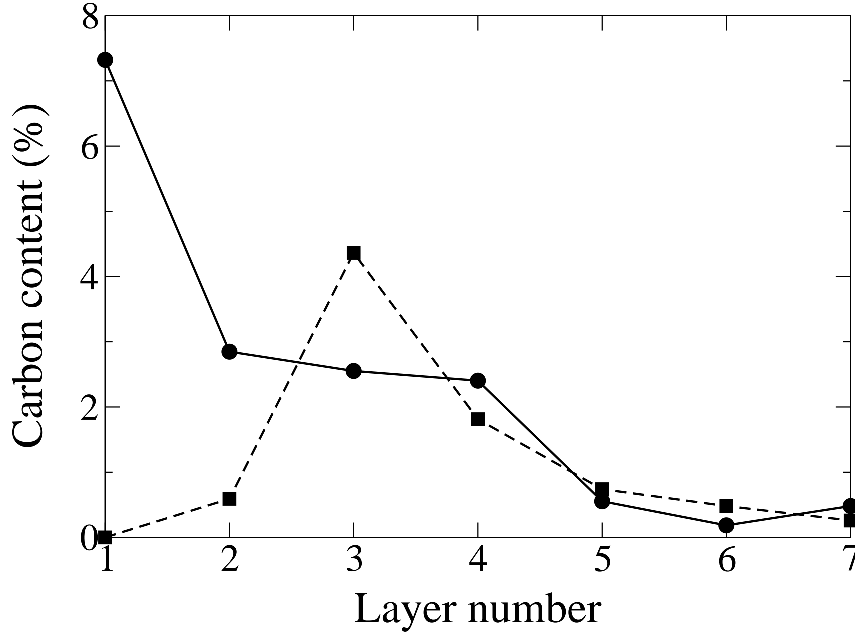

Fig. 4.6: Carbon content in substrate layers. Layer numbered 1 denotes the top layer. Solid (dashed) line shows variation in cell with 0.5 (1.6) ML Ge. The C coverage is 0.36 ML.

ML Ge coverage. Obviously, the Ge–C repulsion forces C into deeper layers. On the other hand, Ge atoms are found to stay on top. We conclude that the relaxed Ge overlayer covers the Si-C geometries.

This has an important consequence. The average of the site occupancies over the whole island yields its Ge content. This comes out to be $\sim$ 60%, for 0.36 ML C, compared to $\sim$ 50% for the bare case [122]. We interpret this to mean that C atoms in deeper layers act as a trap of Si atoms. This decelerates the diffusion of Si in the dot, and the out-diffusion of Ge, so enhancing the Ge content and providing better confinement conditions.

In order to justify this, the vertical variations of Ge content, for the different C coverages (0.16 and 0.36 ML), are calculated, Fig. 4.7. Note, that the trend of these variations are the same compared with the bare case. Again, the Ge content is slowly varying in the bottom and rapidly varying when approaching the apex of the island. However, the variation is mainly influenced in the bottom layers of the island, while the Ge content in the apex remains almost the same. This confirms the observation that the C atoms enhance the Ge content in the islands. We expect that for 2.5 ML Ge, where the PL signal is at the maximum [123], the enhancement of Ge content in the dot will be even stronger.

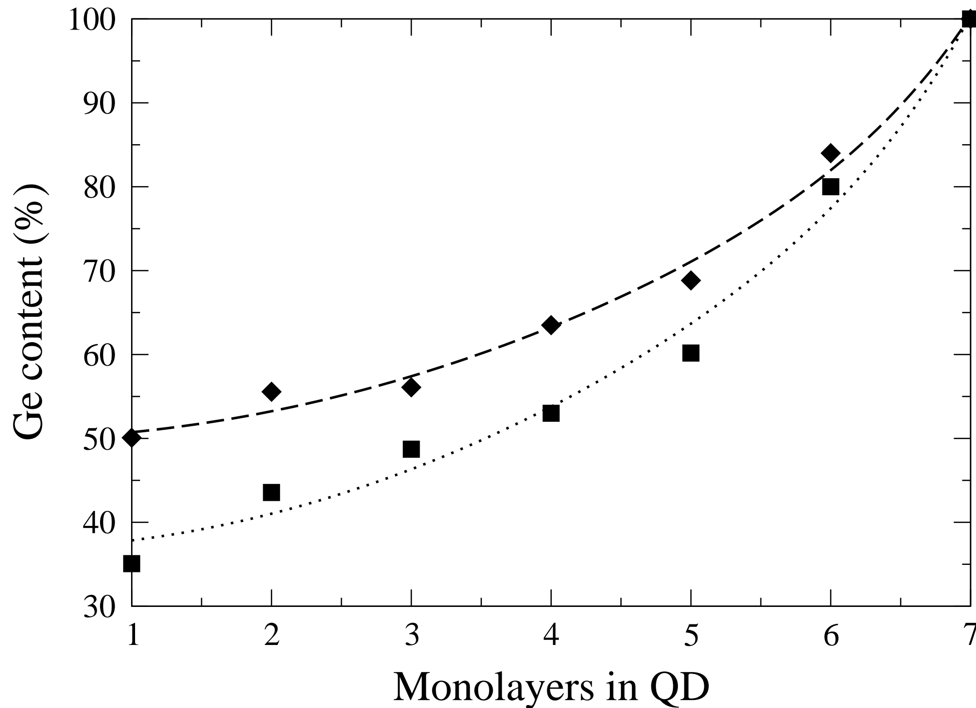

Fig. 4.7: Vertical variation of Ge content in the intermixed island. Squares (diamond) show variation with 0.16 (0.36) ML C. The drawn lines are just guide to the eye.

4.4 Conclusions

In conclusion, our MC simulations provided firm answers about the composition and stress field of C-induced Ge dots, and resolved the controversy between experimental studies. From the investigation of the distribution of each specie, we found that the dot remains free of C. The most important is that the terrace is as well free of C, and the layer below contains a very small amount of it. This is a clear evidence that the islands are located between C-rich regions. Note that this finding is in very good agreement with the experimental results of Ref. [119].

Also, we predict enhancement of Ge content in the islands compared to the C-free case. More specifically, C atoms act as a trap of Si atoms preventing the diffusion of Si in the dot. An increasement of 10% of the Ge content in the island is observed by the predeposition of 0.35 ML C.

Chapter 5

Si Nanocrystals Embedded in a-SiO_2 I. Spherical Nanocrystals

We develop realistic models of Si nanocrystals embedded in a-SiO_2 using a Monte Carlo approach. The interface structure and its energetics are studied as a function of the nanocrystal size. We find that the low-energy geometries at the interface are Si-O-Si bridge bonds. Remarkably, their fraction strongly declines as the size becomes smaller. Concurrently, the embedding causes substantial deformation in such small nanocrystals. Based on these findings, an alternative explanation is given for the reduced optical gaps in this size regime.

5.1 Introduction

Silicon nanocrystals (Si-nc) embedded in an insulating matrix, usually a-SiO_2, have been extensively studied in recent years because of their photoemission properties [40]. It is believed that the interface between the Si-nc and the oxide matrix plays a crucial role in controlling the optoelectronic properties. However, as in the case of porous Si (p-Si) [36, 39], the interpretation of the origin of light emission relies on models which are mainly drawn from the consideration of isolated nanocrystals. These include models based on quantum confinement [37, 124, 125], and on oxygen-related localized surface states [39, 66, 67].

Despite its apparent importance, the structure of the interface of this composite material remains unclear. The kind and proportion of bonds, the width of the interface, and the Si oxidation states are crucial parameters which are poorly known. In addition, since both the quantum confinement effect and the surface local structures depend on the size of the Si-nc, it is essential to examine their stability in the amor-

phous oxide, against distortions and deformations, as they become smaller. This is particularly important for nc sizes below $\sim$ 2 nm, where interesting photoluminescence (PL) phenomena occur [39, 66, 67].

Here, we report the first direct simulations of the Si-nc/a-SiO_2 composite system, which are based on realistic structural models. This is made possible by using an efficient Monte Carlo (MC) approach, which is able to obtain the equilibrium structure of the interface, to investigate its energetics and stability as a function of the nc size, and to incorporate explicitly the interaction of the Si-nc with the embedding amorphous oxide.[1]

The employed MC methodology has been well tested and applied with success for the description of the planar interface [58, 60]. In this method, the Si/a-SiO_2 system is modeled as a defect-free network in which Si and O have four and two bonds, respectively, without any O-O bonds. The energy is reasonably approximated by a Keating-like valence force model. This is composed of two terms representing the cost for bond-length and bond-angle distortions (strain energy), and an additional "suboxide penalty" term, which represents the chemical energy cost for the formation of any suboxide, taken from *ab initio* calculations [90]. Details about the functional form and parameters of the model can be found in Ref. [60].

5.2 Simulation

5.2.1 Construction and Amorphization of the Cell

To generate the amorphous oxide, the MC algorithm of Wooten, Winer, and Weaire [74] is used. This is a well established method to generate continuous random networks, starting from the perfect crystal, by bond breaking and switching [58, 60, 74]. To compositionally equilibrate the interface, we use bond conversion moves [58], which exchange a Si-Si bond in the nc with a neighboring Si-O-Si bond in the oxide. The number of Si and O atoms remains fixed this way. In both types of moves, we first relax locally the structure, following the attempted move, using a steepest-descent method minimizing the forces on the atoms. Then, the change ΔE in energy between this final and the initial configuration is calculated. The attempted move is accepted or rejected according to the Metropolis criterion. Bond switching and conversion moves are periodically followed by volume relaxation moves to relieve the stress in the entire system.

[1] The results of this work have been published in : G. C. Hadjisavvas, and P. C. Kelires, *'Structure and Energetics of Si Nanocrystals Embedded in a-SiO_2'*, Physical Review Letters, **93**, 226104 (2004).

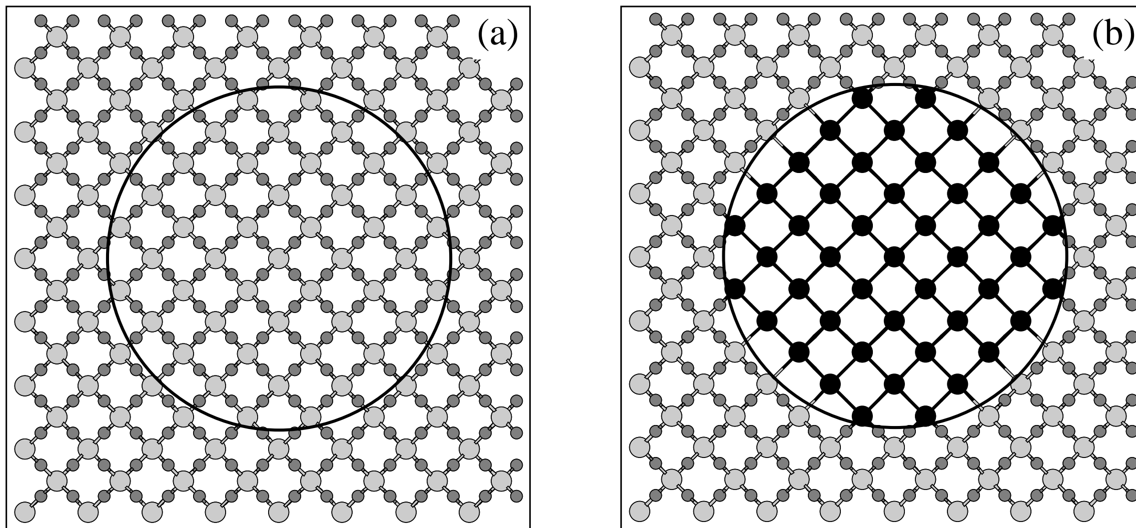

Fig. 5.1: Ball and stick model (part of a thin slice cut) of a Si-nc embedded in a-SiO_2. Dark spheres show Si atoms in the nc. Large (small) grey spheres show Si (O) atoms in the oxide, respectively. Arrows indicate the formation of bridge bonds.

5.2.2 Construction of the Cell

The composite system is generated as follows. We start with a cubic cell in the β-crystobalite structure, the closest to the diamond structure among the SiO_2 polymorphs, containing approximately 8200 atoms. Within a predetermined radius from the center of the cell, all O atoms are removed, giving rise to an all-Si spherical region to simulate the Si-nc. Then, this unphysical starting geometry, which is highly strained both in the Si-nc and the crystalline SiO_2 region, is relaxed to its energy minimum.

5.2.3 Amorphization of the Matrix

In the second stage, we perform MC bond switching in the oxide at a high temperature ($k_BT = 3$ eV) for 40 000 moves, allowing it to liquify. Subsequently, the temperature is gradually reduced to 0.1 eV, bringing the oxide to its glassy, amorphous state [60]. Quenching lasts for more than 1 000 000 moves. During these processes the positions of the atoms in the Si-nc are kept fixed. We then perform unconstrained MC bond conversion and switching of the entire composite system at 0.1 eV (887 °C) for up to 3 000 000 moves, allowing it to both compositionally and topologically equilibrate.

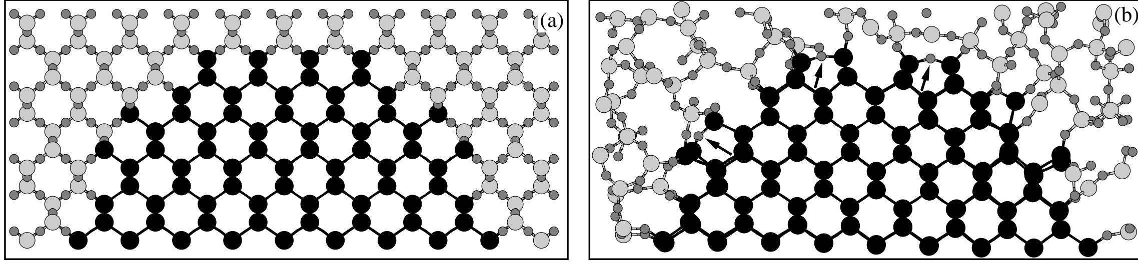

Fig. 5.2: Ball and stick model (part of a thin slice cut) of a Si-nc embedded in a-SiO_2. Dark spheres show Si atoms in the nc. Large (small) grey spheres show Si (O) atoms in the oxide, respectively. Arrows indicate the formation of bridge bonds.

5.3 Results

We have generated in total 12 different fully relaxed composite structures. The size of the Si-nc ranges from 1.2 to 3.5 nm in diameter, and the number of atoms in the nc from $\sim$ 30 to $\sim$ 900. The total content of Si in the whole structure varies from 34% to 44%, close to what is found experimentally. The properties of these structures are calculated by taking averages at 0.1 eV over 800 000 MC steps.

5.3.1 Structural Characteristics

A representative example of a fully relaxed structure, with a relatively large nc (3.2 nm), is shown in Fig. 5.2. Our central finding is that a considerable number of Si-O-Si bridge bonds, in which an O atom connects two Si atoms terminating the Si-nc, have been formed at the interface. Their relative fraction is $\sim$ 60%. The driving force for their formation is the lowering of the interfacial strain energy. We estimate a drop in energy of $\sim$ 0.05 eV/Å^2 when the interface relaxes by bond conversion, leading to enhancement of bridge bonding. The notion that bridge bonds lower the energy has been earlier recognized [59, 60] in the case of the planar Si(001)/a-SiO_2 interface. Bridges can be stretched and bent with minimal energy cost [59]. Ordered arrays of bridges were proposed by *ab initio* calculations [59] and identified by MC simulations [60]. The level of bridge bonding reached in these simulations was of the order of 75%.

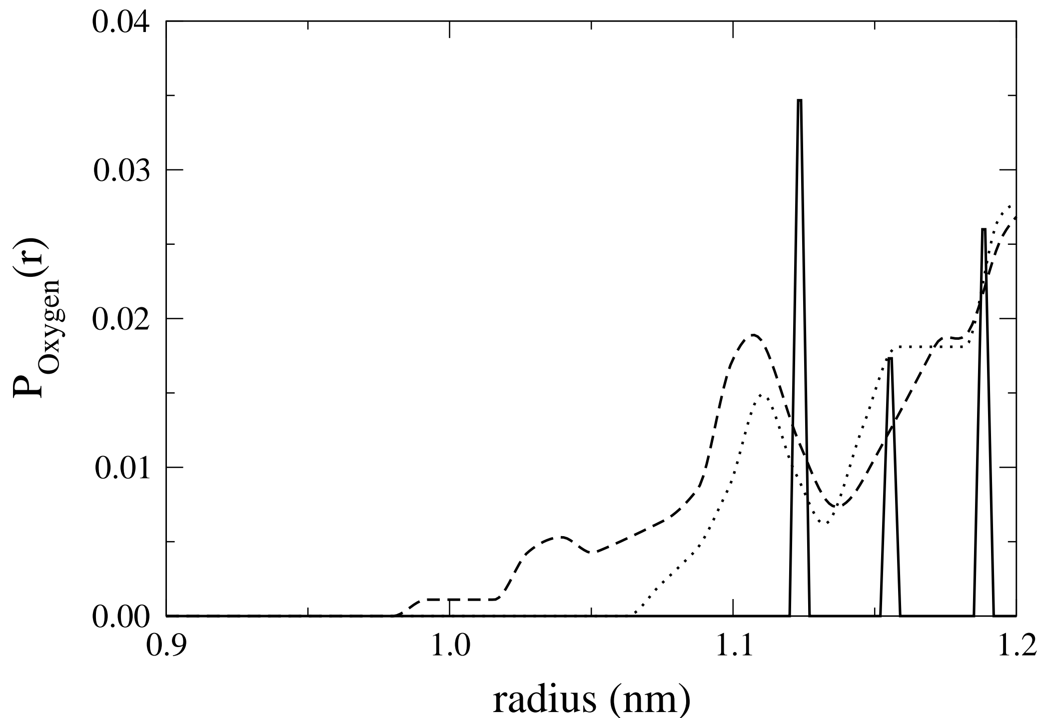

Fig. 5.3: Propability of finding an Oxygen atom versus its distance from the center of the nc. The initial size of the nc was ~ 1.1 nm. Solid line denotes the probability for the initial structure, dotted line is for the structure before the compositional equilibration, and dashed line for the final structure.

5.3.2 Oxygen penetration

One of the advantages, of our simulation, is the ability of the system to equilibrate compositionally, by applying the bond conversion moves. In this way, the methodology gives the posibility of an oxygen atom to penetrate into the Si nanocrystal. The propability of finding an oxygen atom versus the center of a nanocrystal is calculated and is shown in Fig. 5.3. In this figure the nanocrystal with size of ~ 1.1 nm is shown. Note that all nanocrystals have the same trend.

In the initial structure (solid line) all the oxygen atoms are in well defined positions. That is why the delta functions appear in this variation. The firsts oxygen atoms are at 1.13 nm away from the center of the nanocrystal. After the amorphization of the matrix, but before the compositional equilibration of the whole system, the $P_{oxygen}(r)$ became smoother while the oxygen atoms came closer to the center of the nanocrystal for about 0.5 nm (dotted line). This small oxidization happens for two reasons. Either from the constructions of bridge bonds or from the distortions

of the surface atoms.

In the final structure, after bond conversion moves, the oxygen atoms get even closer to the center of the nc but only for less than 0.10 nm (dashed line). A penetration which is negligible concerning the temperature of the system (0.1 eV). It must be noticed that although in our simulation there is a possibility for oxygen atoms to penetrate deep into the nanocrystal, this does not happen. The oxygen atoms enter into the nc only one Si-O bond length. This result means that the Silicon nanocrystal is stable enough to prevent deeper oxidization. However, this oxidization reduces the size of the nanocrystal core from the initial size of 2.3 nm to 2.0 nm.

5.3.3 Chemical Composition

Oxidation number is the number of Oxygen atoms that a Si atom has. That means that oxidation numbers Si^{+1}, Si^{+2} and Si^{+3} correspond to the suboxides Si_2O, SiO and Si_2O_3 respectively. In this way, it is obvious that the variation of the oxidation numbers would be from Si^{+0}, in the center of the nc, to Si^{+4}, in the amorphous matrix.

It is known that in the 'ideal' interface Si(100)/a-SiO_2 exist only silicon atoms with oxidation number +2 (Si atoms with 2 oxygen as neighbors), while in the case of interface Si(111)/a-SiO_2 intermediate oxidation numbers, +1 or +3, [126] are present as well. On the other hand, experimentally is shown that in Si/SiO_2 there is a chemically nonabrupt interface with the coexistence of all intermediate oxidation states [126, 127]. Examining more carefully the structure is found that there are distinct areas in which there are mainly one or two oxidation states.

In our system we expect to have all the oxidation numbers at the surface because of the spherical shape of the nanocrystals. In order to affirm this, we made the oxidation distribution versus the distance from the center of the nanocrystal, which is shown in Fig. 5.4. The nanocrystal of radious ~11 Åis chosen. Indeed, the coexistence of all oxidation numbers is verified and ensures the roughness of our surface.

An important quantity is the total number of Si atoms in intermediate-oxidation states (N_{SiO_x}) and even the number of Si atoms in every oxidation state. These quantities can give us an overview of the transition layer. Hence, we found $N_{SiO_x} =$ 130 while from the number of Si atoms in every oxidation state ($N_{Si^{+1}}$,$N_{Si^{+2}}$,$N_{Si^{+3}}$) we can calculate the average ratio for all atoms of the interface. This average ratio is 1.28:1.00:1.05 ($Si^{+1} : Si^{+2} : Si^{+3}$) and its main result is that the most probable oxidation number is Si^{+1}.

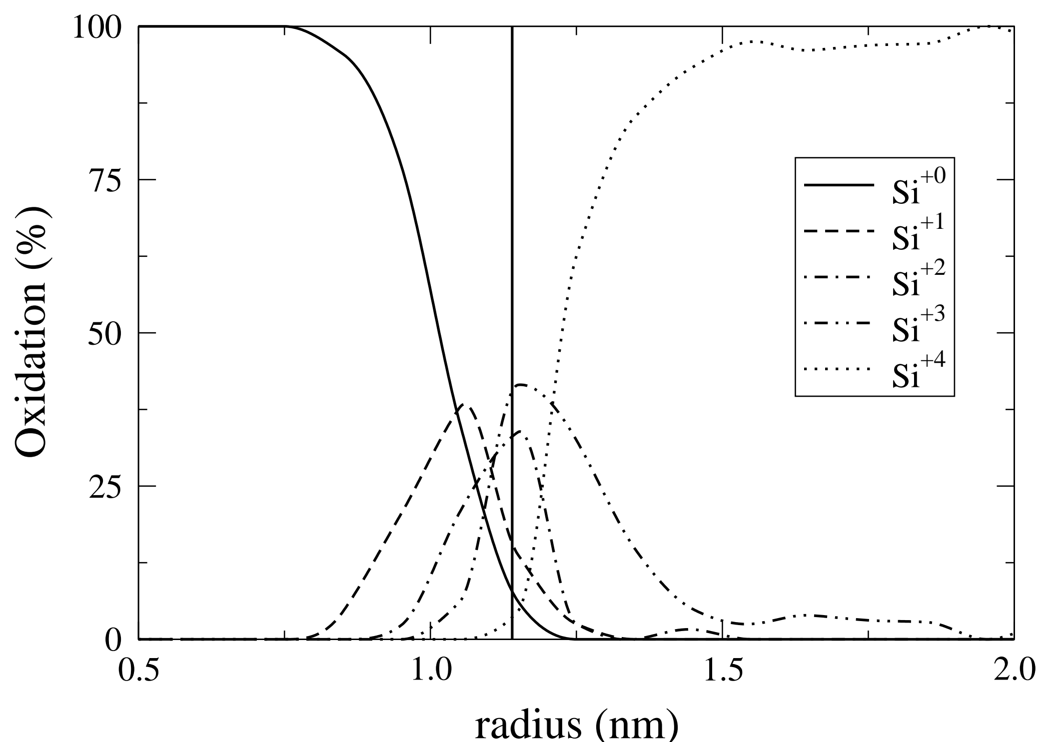

Fig. 5.4: Oxidation numbers versus the distance from the center of the nanocrystal, for the nc with size 1.1 nm. The vertical solid line shows the nominal position of the respective interface.

Also, it is shown that firstly appear atoms with oxidation number +1 and then, almost simultaneously, oxidation numbers +2 and +3. Another interesting point is the distance in which every oxidation state is distributed. Oxidations numbers Si^{+1} and Si^{+2} are spreaded for less than 0.5 nm while Si^{+3} is dispersed in bigger distance.

Furthermore, one would want to conclude that the Si^{+1} and Si^{+2} moieties are located right at the interface, while the Si^{+3} ones are distributed within a nm from the interface. The same results are found in the case of flat interfaces [126].

A straightforward definition of the interface can be given by taking the layer that contains silicon atoms in intermediate-oxidation states. From this figure we can also estimate the width of the surface. It is clearly shown that the thickness of the transition region (where all the oxidation states coexist) is of the order of 0.8 nm. Note that all the nanocrystals have almost the same chemical composition.

5.3.4 Bridge Bonds

It is remarkable that the fraction of bridge bonds at the interface of Si-nc approaches that at the planar interface. The majority of bridges are still formed on the (100)-oriented parts of the interface. However, numerous bridges are formed on other parts, too, as inspection of Fig. 5.2 reveals. (A bridge is shown to have been formed on the (111)-oriented part.) This indicates that bridges are low-energy structural elements on such parts of the interface, as well. We have not been able to raise higher the fraction of bridge bonding, even with intense annealing. Due to the finiteness and the curved nature of the interface, neither ordered arrays of bridges nor a fully bridge-bonded structure can be formed.

Note that within the methodology employed here no Si═O double bonds can be formed at the interface. It was proposed that such bonds create localized surface states which reduce the effective size of the optical gap [39, 66], and can explain the observed redshift of PL in oxidized p-Si and Si-nc. However, as Vasiliev *et al.* [67] showed, practically same gap reductions occur when having Si-O-Si bridge bonds on the surface, instead of double bonds. Therefore, in the following, we consider bridges as a representative type of bonds producing the gap effects due to oxidation.

One of the prime goals of this work was to monitor the interfacial properties as the size of the Si-nc varies. We first focus on the width and the energy of the interface. A quantitative measure of the width is provided by the rms value σ, which can be defined [60] by $\sigma^2 = \sum(r_i - \bar{r})^2/N_{sub}$, where N_{sub} is the number of Si suboxide atoms, r_i is the distance of suboxide atom i from the center of the nc, and $\bar{r} = \sum r_i/N_{sub}$ is the nominal position of the spherical interface. Fig. 5.5(a) shows the variation of σ with size. Clearly, σ increases linearly as the Si-nc shrink, indicating wider spread of suboxides at the interface.

5.3.5 Interface Energy

The variation of the interface energy is shown in Fig. 5.5(b). This energy can be defined as the difference between the total energy, including the suboxide penalty, and the sum of the bulk energies of the amorphous oxide and crystalline Si. Overall, the energy rises as the Si-nc shrink, indicating lower stability. However, contrary to the linear variation of σ, there are two distinctly different regimes in this variation. In the regime over 2 - 2.5 nm, the rise is slow, and the energies lie within the limits defined by the energy of the ideal planar Si(001)/a-SiO$_2$ interface with no suboxide layers (lower limit) and the energy of the planar interface with suboxide layers (upper limit) [59, 60].

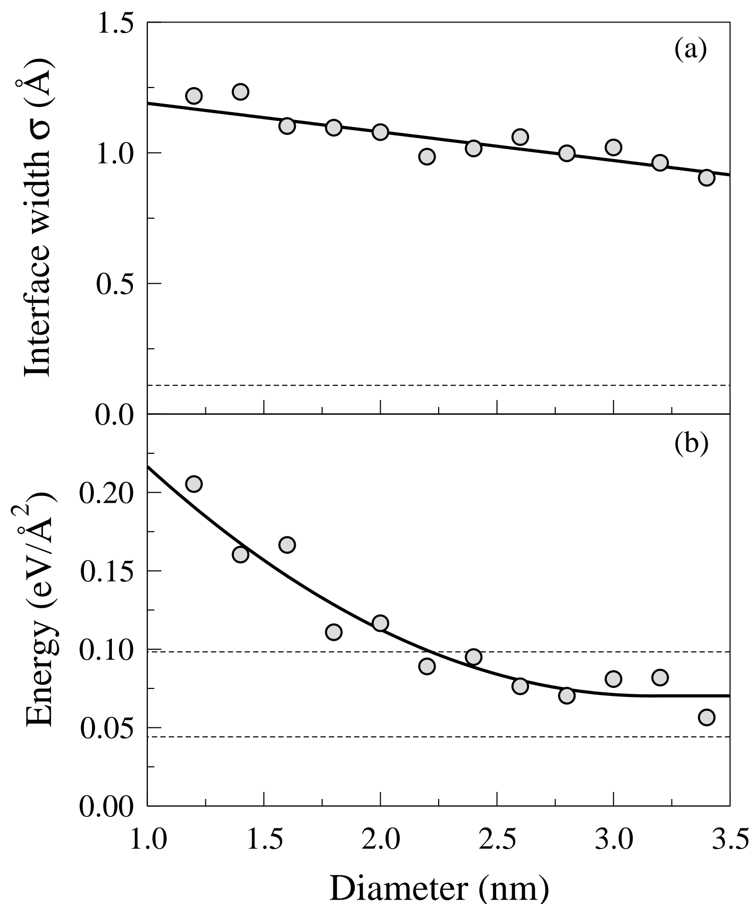

Fig. 5.5: Variation of the (a) interface width and (b) interface energy with the Si-nc size. Solid lines are fits to the points. The dashed horizontal line in (a) shows the width of the ideal planar interface. The dashed horizontal lines in (b) show the energy of the planar interface without suboxides (bottom) and with suboxides (top).

On the other hand, the energies in the size regime below 2 nm rise sharply. This can not be explained by the widening of the suboxide transition region, and the associated increase of chemical energies [90], because the widening variation is linear without any turning point around 2 nm. Instead, much of the sharp energy increase is due to strain which heavily builds up as the Si-nc become smaller.

There are two major contributors to this increase of strain energy. The first is related to bridge bonding. An outstanding finding of our simulations is that the fraction of bridge bonds strongly declines as the size gets smaller. As shown in Fig. 5.6, the reduction is drastic below 2 - 2.5 nm. Bridge bonds are strain-relieving geometries, and reduction in their number increases the interface energy.

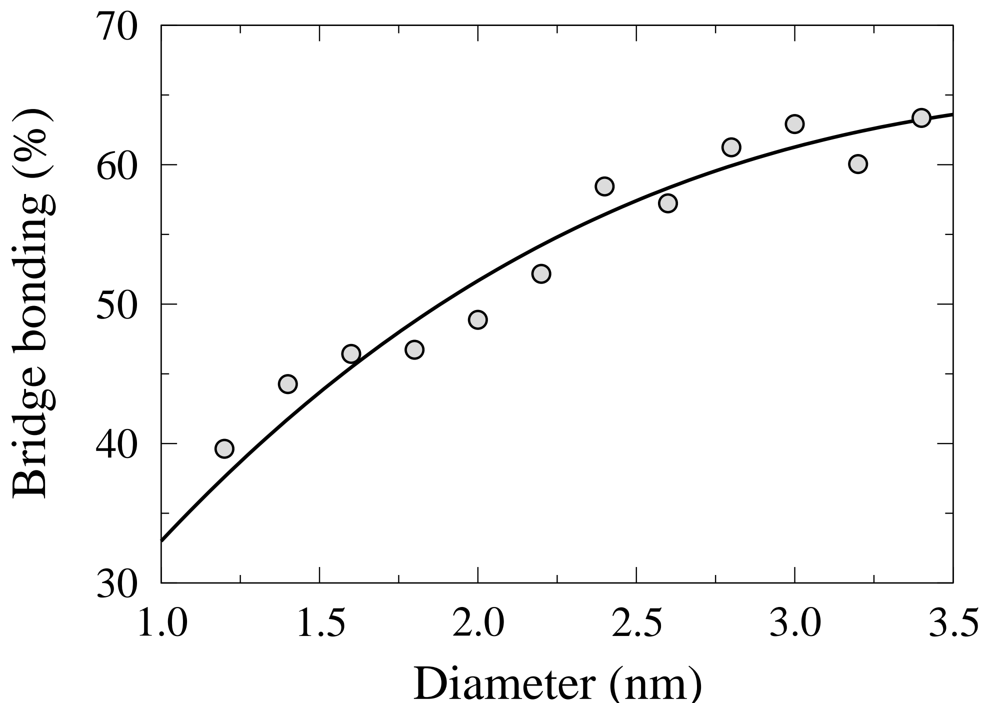

Fig. 5.6: Percentage of bridge bonding as a function of Si-nc size. Line is a fit to the points.

The second, and even more important, contribution to the energy increase comes from the network disorder and deformation incurred at the transition region, as a consequence of embedding the nc in the host oxide matrix. This factor has not been accounted for in studies dealing with isolated nanocrystals. When these two different materials, having a large density gradient (9%), merge at their interface, the network topologies in either side deform in order to accomodate the transition. Obviously, the smaller the nanocrystal, the more heavily strained and distorted is expected to be when put in the embedding host medium.

We demonstrate these principles in Fig. 5.7. Panel (a) shows the variation of the tetrahedral vector $\vec{v}_t$ [128] for three representative embedded Si-nc. $\vec{v}_t$ equals to the sum of the vectors pointing from an atom to its nearest neighbors, and it shows the deviation from ideal tetrahedral geometry (zero value). Thus, it includes both bond-length and angle distortions. We observe a progressive increase of deformation as the size decreases. For the larger nc (3.5 nm), distortions are concentrated near the interface. However, for the nc in the critical size regime (2.2 nm), distortions also develop in its interior, and the distribution widens. The striking feature is that the smaller nc (1.4 nm) is heavily deformed, even in the core region.

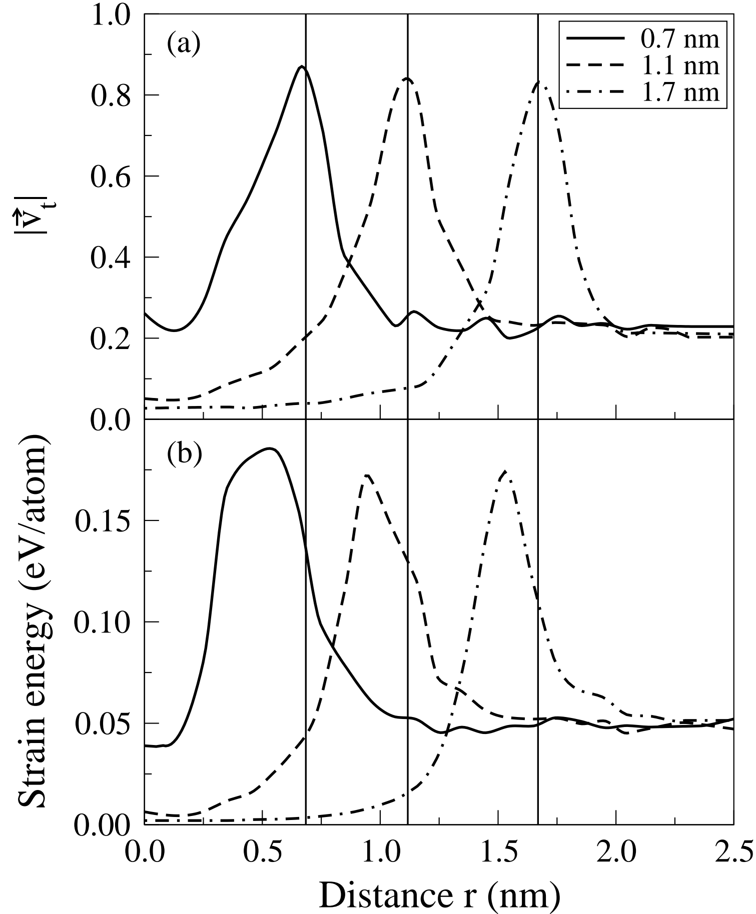

Fig. 5.7: (a) The magnitude of the tetrahedral vector and (b) the strain energy of three different nanocrystals versus the distance from their center. The vertical solid lines show the nominal position of the respective interfaces (see text.)

The corresponding variations of strain energy are shown in Fig. 5.7(b). (The strain energy is decomposed into atomic contributions [60] and averaged over spherical shells 1 Å wide.) Most of the strain energy is concentrated inside the nanocrystals. The embedding oxide is less strained, because the amorphous network has more flexibility to accomodate the structural incompatibility. The heavy deformation of the small nc is reflected into its high interior strain energy.

It can be easily seen that disorder and reduction of bridge bonding are interrelated. Actually, the former is the driving force for the latter. We find that when the interface is highly disordered, both bond lengths and angles involved in bridge bonds are forced to deviate from their nominal values (1.6 Å, $\sim$ 145°). Therefore, their formation is not so energetically favored.

The two remarkable findings in our simulations give us the opportunity to offer an alternative, *albeit* qualitative, explanation for the relatively small energy gaps in Si-nc, in the size regime below 2 nm. We propose that the observed PL redshift is not due to the interface oxygen states alone, but in a large degree also due to the high disorder in the nc. This is based on the crucial observation that bridge bonding declines as size decreases. As shown theoretically [66, 67], the pinning of gap energy is proportional to the fraction of Si=O double bonds or Si-O-Si bridge bonds. Thus, the surface states would play a weaker role in counterbalancing the strong confinement effect, and the gap should increase. It does not, because strain and deformation in the nanocrystal introduce localized states near the band edges and effectively reduce the optical gap. A smaller contribution from the strained oxide side of the interface should also be anticipated [68].

5.4 Conclusions

In conclusion, we have shown that the interface properties of Si nanocrystals are strongly influenced by the embedding amorphous oxide matrix, especially when they attain sizes smaller than 2 nm. Large deformations and decline of bridge bonding are observed. Both findings play a crucial role in understanding the PL properties of small nanocrystals.

Chapter 6

Si Nanocrystals Embedded in a-SiO_2 II. Faceted Nanocrystals

Planar interfaces of different crystal orientations between crystalline Si and amorphous SiO_2 are constructed using a Monte Carlo approach. We find that the lowest-energy interface is the Si(100), while the Si(211) is the energetically closest one to the Si(100). Using the Wulff construction method, the shape of the embedded nanocrystal in a-SiO_2, is predicted. The distortions of the Si-O-Si bonds are found to be larger in the spherical nanocrystals than in the Wulff shape. This is believed to be the key factor for the formation of faceted nanocrystals.

6.1 Introduction

The study of silicon quantum dots is a very active field of research, because of the interesting fundamental physical properties of these mesoscale objects and of promising applications in advanced electronic devices and optical applications. The visible light emission of nanostructured silicon is well known 15 years now [36]. Thanks to the large number of studies devoted to nanostructured Si, the opening of the band gap, when the nanocrystal size shrinks is nowadays an unquestionable fact. This opening arises as a consequence of the quantum confinement of carriers in the three dimensional potential well of the nanocrystal [129, 130].

It is obvious that the structural and the optoelectronic properties of the nc-Si/SiO_2 system are highly correlated. The interface between those two composites plays an active role for the behavior of these systems. The oxidation of Si nanocrystals introduces defects in the band gap, which pin the transition energy. It is found

that the formation of either Si=O double bonds [39, 66] or Si-O-Si bridge bonds [67] are the pinning states.

Since the nc-Si/SiO_2 interface plays such a vital role, it is essential to know whether it is spherical or faceted, and which facets participate in the formation of non-spherical nanocrystals. Experimental information on the subject is rather limited. The work of Ishikawa *et al.* [55] showed that nanocrystals of sizes larger than 4 nm have well defined facets. The observed facets, were the (100) and (111) ones. On the other hand, Wang *et al.* [56] concluded that faceting is thermodynamically favorable to minimize the surface energy leading to an equilibrium shape. Faceting has been observed in Si nanocrystals with diameter greater than 6 nm, while the smaller nanocrystals are mainly spherical. In their case well defined facets of the (100), (111) and (113) orientations were observed. On the other hand, a theoretical treatment of the subject is lacking.

The scope of this section is to shed some light into these open questions and offer a theoretical answer to the problem. Monte Carlo (MC) simulations were used in order to extract the energies of different crystallographic planar interfaces between Si and a-SiO_2. Applying the Wulff theorem and the calculated surface energies, a faceted Si nanocrystal is found to be the equilibrium crystal shape for larger sizes, while for smaller diameters spherical nanocrystals are preferred.

6.2 Simulation

The simulated structures are generated as follows. A periodic strained β-crystoballite cell with layers of a given [hkl] orientation is constructed. An example is shown in Fig. 6.1(a), where the [111] is chosen. The lateral plane is fixed to the lattice constant of Si. The central oxygen atoms of the cell among two predefined planes are removed, giving rise to an all-Si area, Fig. 6.1(b). This area will simulate the Si substrate, having the specific crystal orientation, while the Si volume is chosen to be approximately the $\frac{1}{3}$ of the whole volume. This highly strained structure is relaxed to its energy minimum.

The c-SiO_2 are is then amorphized using the well known WWW method [74], which has been extensively studied in Chapter 2. During the whole simulation only the z-axis was allowed to vary, while the Si atoms of the c-Si area do not take part in the bond-switch moves. Finally, the SiO_2 is amorphized and the total energy of the system is calculated.

Seven different crystal orientations of Si substrate were constructed. The interface energy of each crystal orientation can be calculated by subtracting the bulk

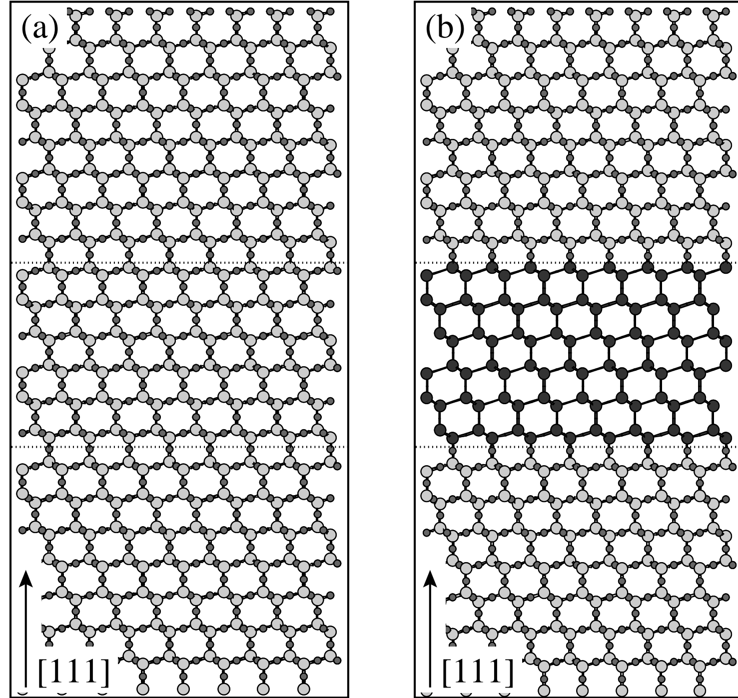

Fig. 6.1: Ball and stick model of the construction of the planar interface Si(111)/c-SiO_2. Dark spheres show Si atoms in the c-Si region. Large (small) grey spheres show Si (O) atoms in the oxide, respectively.

energy of the amorphous dioxide and of the crystalline Si from the total energy of the composite system:

$$E_{inter} = \frac{E_{tot} - N_{Si}E_{Si} - N_{a-SiO_2}E_{a-SiO_2}}{2A}$$

where N_{Si} (N_{a-SiO_2}) is the number of Si (Si and O) atoms in the c-Si (a-SiO_2) area, and E_{Si} (E_{a-SiO_2}) is its bulk energy per atom. The bulk energy of amorphous dioxide has been obtained in independent calculations. On the other hand, the bulk energy of c-Si for the Keating potential, is zero. Also, A is the interface area in Å^2, while the factor "2" is due to the two interfaces per simulation cell.

6.3 Results

By choosing seven different crystal orientations of Silicon substrate, we constructed seven cases of the Si/a-SiO_2 planar interface. These are demonstrated in Fig. 6.2, (a)-(g): (100), (110), (111)I, (111)II, (210), (121), and (221). We carried

Table 6.1: Percentage of bridge bonds, oxidation numbers, interface widths σ (Å), energies of bridge bonds E_{bridge} (eV), and interface energies E_{inter} (eV/Å^2), for various orientations. The (100) orientation is used as a reference for the bridge bonds and the interface energies.

	(100)	(110)	(111)I	(111)II	(210)	(121)	(221)
% bridges	100	0	100	0	83	60	59
Si^{+1}:Si^{+2}:Si^{+3}	0:1:0	1:0:0	0:0:1	1:0:0	1:1:1	3:2:1	1:0:1
σ	0.08	0.12	0.12	0.10	0.61	0.57	0.58
E_{bridge}	0.00	-	0.23	-	0.25	0.21	0.31
E_{inter}	0.000	0.010	0.010	0.010	0.061	0.005	0.050

out two different simulations for the (111) interface because of the distinctiveness of this orientation. One having terminating Silicon atoms with oxidation number +3, Fig. 6.2(c), and one with oxidation number +1, Fig. 6.2(d). Of course in the latter case, because of the morphology of the interface, it is extremely difficult for a bridge bond to be formed.

The characteristics of each structure are shown in Table 6.1. One of the most important properties of the Si/a-SiO_2 interface, is the percentage of bridge bonds at the interface. As it is mentioned in Chapter 1, bridges are the lowest energy key elements because they can bend and stretch with minimal energy cost. Also, it is found that the energetically lowest structure of the Si(100) interface is the one having 100% bridge bonds. The same finding is shown in this Table, and thus this structure is used as a reference.

An important point is that except of the (100) crystal orientation, the (111)I orientation is also composed of 100% bridge bonds. On the other hand the (110) and the (111)II interfaces have no bridges. Finally, all the other structures have intermediate percentage of bridge bonds.

Another property of the interface is the dispersion of the suboxides σ, a term which was defined in Chapter 5. This term is a quantitative measurement of the width of the interface. The σ for every crystal orientation is also given in this Table. The first four interfaces between c-Si and a-SiO_2 can be characterized as *abrupt* because of the small value of σ ($\sim$ 0.1 Å). This small dispersion came due to the distortions of the suboxides on the interface. Note that all these structures consist of only one suboxide, i.e. (100) and (110) interfaces are composed of only Si^{+2} atoms, (111)I of Si^{+3} and (111)II of Si^{+1} atoms. To the contrary, the rest of the interfaces

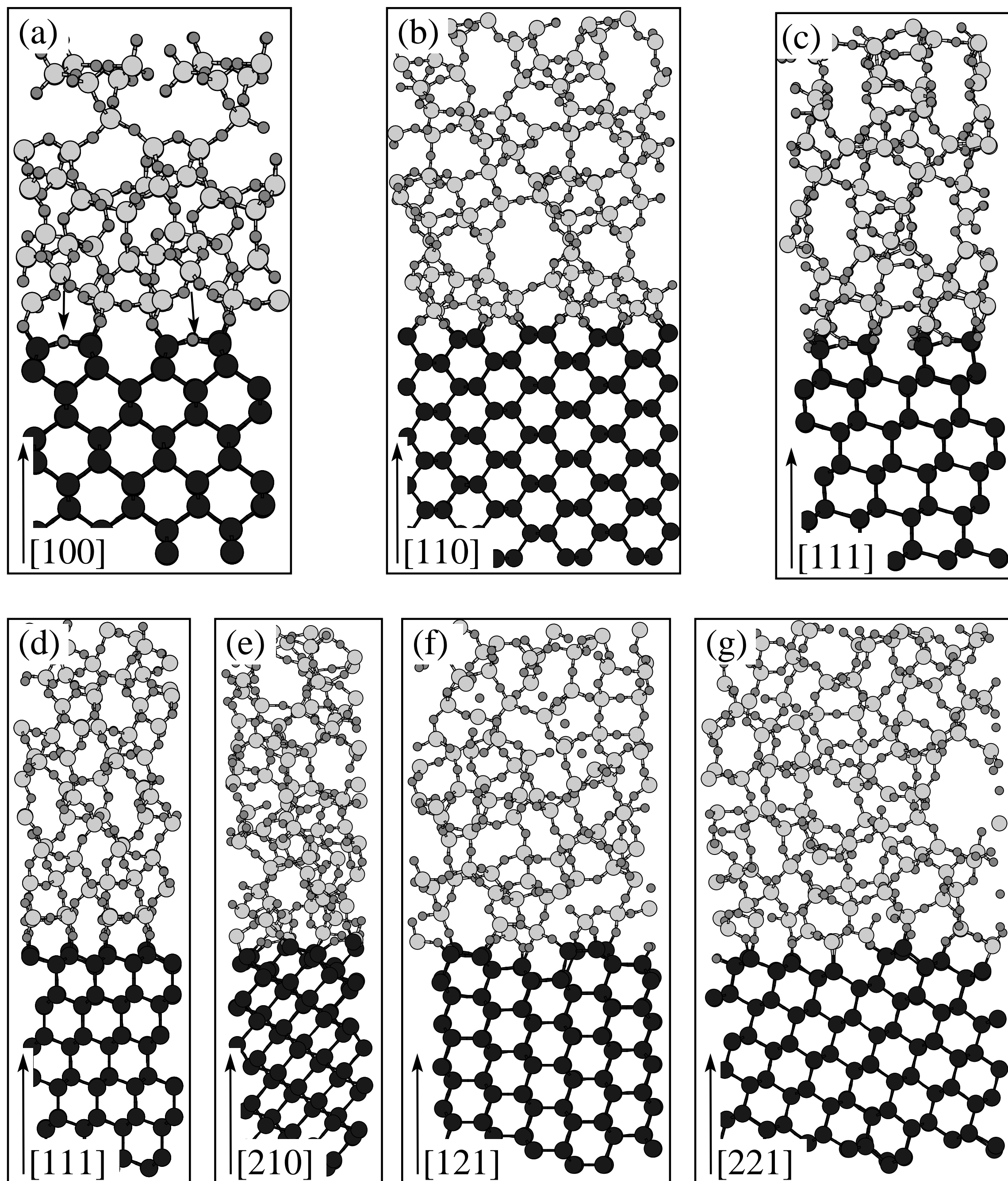

Fig. 6.2: Seven different planar interfaces of Si/a-SiO_2. The crystal orientations are: (a)-(g): (100), (110), (111)I, (111)II, (210), (121), and (221). Dark spheres show Si atoms in the crystalline region. Small grey spheres show O and light grey spheres denote Si atoms in the oxide.

consist of all types of suboxides and thus have a larger value for the dispersion σ (of about 0.6 Å).

As already mentioned, Si-O-Si bridge bonds are of special importance in these structures. So, we gain further insight into the energetics by decomposing the total energy of the system into individual bonding contributions. From this decomposition, the energies of bridge bonds in every configuration are averaged and are shown in Table 6.1. Among all these crystal orientations, the Si(100) has the lowest bridge bond energy. We use this orientation as a reference. The next lowest bridge bond energies are found in the Si(121) case.

The crucial quantities for our analysis are the interface energies, which are shown n last row of Table 6.1. Our main finding is that the closest in energy to the (100) orientation is the (121) structure. Despite the fact that the (121) structure has less bridges than other orientations, the interface energy is very low. This can be attributed to the low energy of bridge bonds that it has. On the other hand, the other non-abrupt interfaces have much larger interface energies and bridge bond energies. The above result means that the (121) orientation is the next to the (100) favorable interface.

Taking these energies into account, one can construct a shape which will minimize the surface energy for a given enclosed volume. This is just the Wulff construction method [92, 131] explained in details in Chapter 2.7. However, let us give the main steps of this method. Along each unit vector $\hat{n}$, a radius is drawn of magnitude $E_{inter}(\hat{n})$, where $E_{inter}(\hat{n})$ is the formation energy of the interface with orientation $\hat{n}$. A plane perpendicular to each such radius vector is drawn passing through its tip. The inner envelope of all these planes is the Wulff construction. Only planes that are part of the Wulff construction are thermodynamically stable.

Applying this method to the calculated interface energies, the optimum shape of the embedded nanocrystal is revealed and is demonstrated in Fig. 6.3. It is a polyhedron composed of 42 facets. However, only three different crystal orientations exist. These are the (100), (110) and (121) with 6, 12 and 24 facets respectively. Note that the (110) case, because of the largest (among these three orientations) formation energy, has the smallest facets.

As mentioned above, the faceted nanocrystals found experimentally were formed by either (100) and (111) [55] or by (100),(111) and (113) facets [56]. We find that the facets which construct the nanocrystal are the (100), (110) and (121). The discrepancy might be attributed partly to the degenerate energies for (110) and (111) found theoretically, and partly to the limited experimental resolution at such small sizes. For example, the (110) facets constitute a very small fraction of the total surface area, and this might be difficult to observe experimentally.

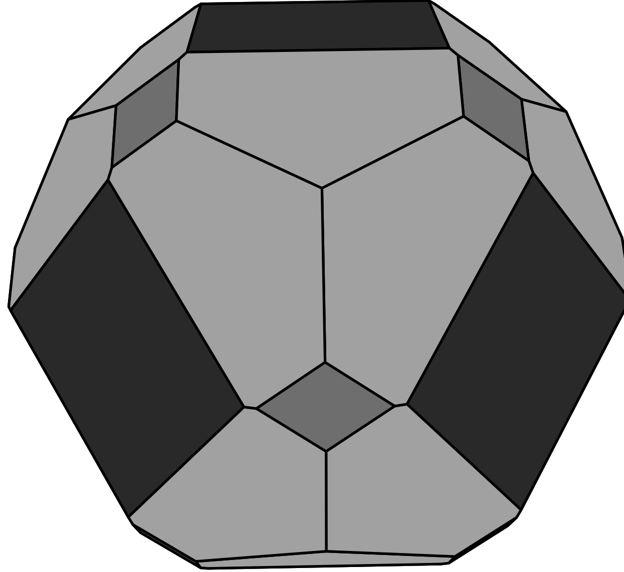

Fig. 6.3: The equilibrium shape of a macroscopic embedded Si crystal using the Wulff construction and the surface energies of Table 6.1. Dark gray shows the (100) facet, gray is the (110) and light gray denotes (121) facets.

The next step in our work is to verify that, when the Si nanocrystal is embedded in the oxide, the above shape is indeed the one with the lowest energy. In order to do this, four different cells were constructed. Two of them contained spherical Si nanocrystals with sizes $\sim$ 3.1 nm and $\sim$ 4.5 nm (hereafter called S1 and S2), while the other two contained faceted nanocrystals with the same sizes as the spherical ones (called F1 and F2, respectively). The faceted nanocrystals have the equilibrium shape, found by the Wulff construction.

The simulational cells containing the faceted nanocrystals are generated applying the same method as in the case of spherical nanocrystals (see Chapter 5) in combination with the Wulff method. An illustration of the procedure is shown in Fig. 6.4. We start with a cubic cell in the β-crystobalite structure, the closest to the diamond structure among the SiO_2 polymorphs, containing approximately 8200 and 17000 atoms for F1 and F2, respectively, see panel (a). Within the polyhedron, predicted by the Wulff construction method, located in the center of the cell, all O atoms are removed, giving rise to an all-Si faceted region to simulate the Si-nc [panel (b)]. Then, this unphysical starting geometry, which is highly strained both in the Si-nc and the crystalline SiO_2 region, is relaxed to its energy minimum.

To construct the amorphous matrix and to compositionally equilibrate the whole system, we apply the methodology used in Chapter 5, The equilibration temperature

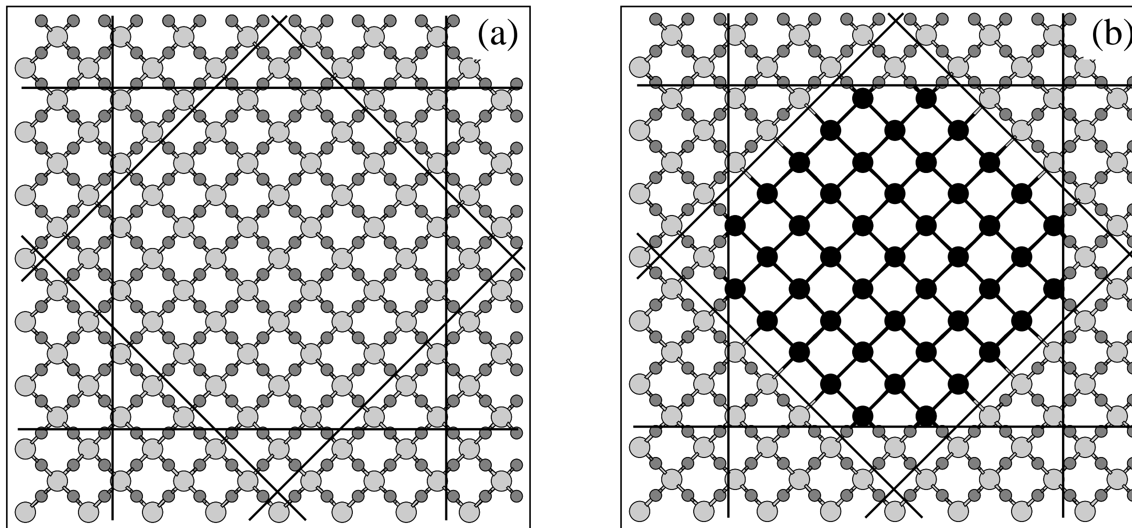

Fig. 6.4: Ball and stick model of the construction of a faceted Si-nc embedded in beta crystobalite. (a) Highly strained beta crystobalite. (b) Creation of a polyhedron and removing all O atoms in it. Dark spheres show Si atoms in the nc. Large (small) grey spheres show Si (O) atoms in the oxide, respectively.

is 0.1 eV. The characteristics of all structures are shown in Table 6.2. Note that for all samples the total content of Si is kept at about 41%, although there are two different sizes of nanocrystals, in order to have similar oxide embedding environments. Note also that the nanocrystals are far away from their image due to periodic boundary conditions. So, the interaction between the nanocrystals and their images can be neglected.

Table 6.2: Characteristics of the four samples S1, F1, S2 and F2 (see text).

	Size (nm)	N_{total}	Si cont. (%)
S1	3.1	6672	41.1
F1	3.1	6668	41.2
S2	4.5	14168	41.2
F2	4.5	14204	41.1

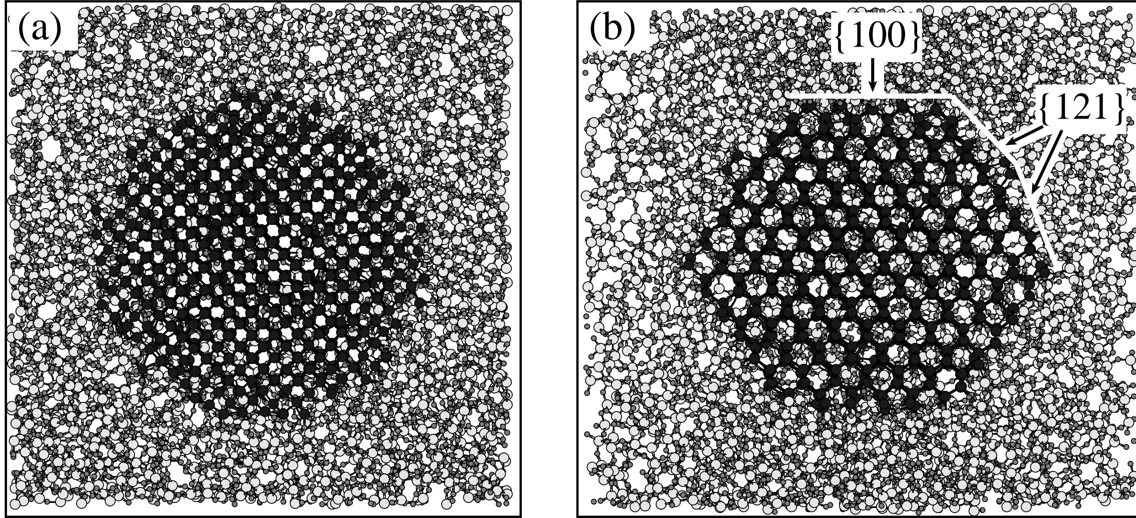

Fig. 6.5: Ball and stick model of the final structure of (a) a spherical (S2) and (b) a faceted (F2) nanocrystal. Dark spheres show Si atoms in the nc. Large (small) grey spheres show Si (O) atoms in the oxide. In (b) the (100) and the (121) planes are clearly distinguished.

6.4 Spherical vs Faceted Nanocrystal

The final structures of the relaxed in the oxide S2 and F2 nanocrystals are portrayed in Fig. 6.5. It is clearly shown that the facets of the second nanocrystal withstand the pressure of the amorphous matrix and are, thus, conserved. Despite the fact that the temperature of this equilibration was quite high (0.1 eV), the facets of the nanocrystal were still well defined. On the other hand, the smaller embedded nc (F1) did not manage to keep its facets intact, but it was heavily deformed towards obtaining finally a spherical shape, Fig. 6.6. This can be explained by noting that the edges and the apeces are the regions most vulnerable to distortions, as concentrating much of the stress. When the size gets smaller than a critical value, which we estimate to be of the order of 4 nm, the edge effects become paramount and lead to the destruction of the faceted shape. These ideas can be quantified by analyzing the interface energies in our cells.

We first compare the interface energies of the S2 and F2 nanocrystals. This energy can be defined just as in the case of planar interfaces, i.e., as the difference between the total energy, including the suboxide penalty, and the sum of the bulk energies of the amorphous oxide and crystalline Si. We find that the energy of the spherical nanocrystal (S2) is 0.066 eV/Å^2, while that of the faceted (F2) is 0.052 eV/Å^2. The reduction of the energy by 0.014 eV/Å^2 reveals that the faceted shape

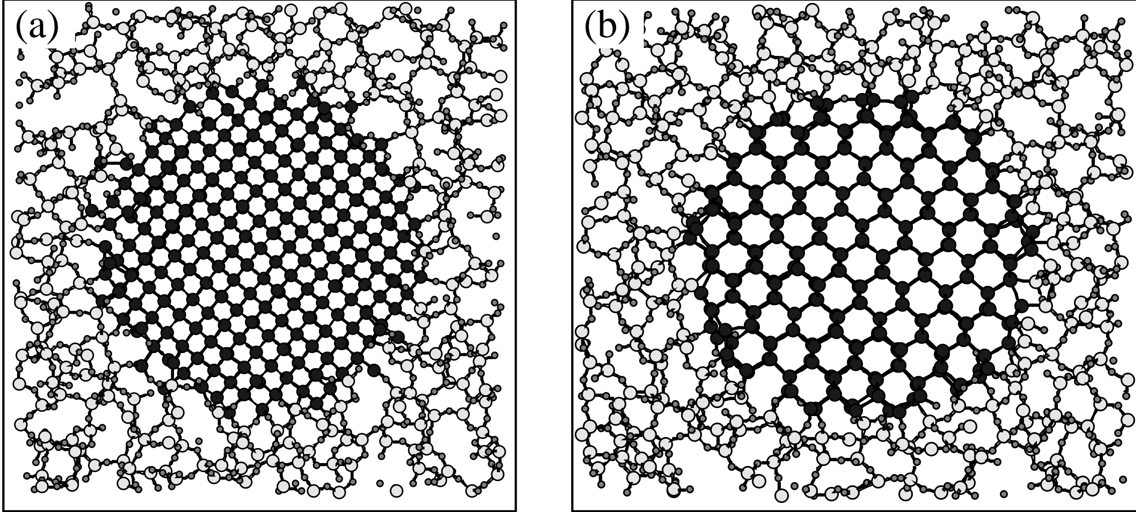

Fig. 6.6: Ball and stick model (a thin slice cut) of the final structure of (a) a spherical (S1) and (b) a faceted (F1) nanocrystal. Dark spheres show Si atoms in the nc. Large (small) grey spheres show Si (O) atoms in the oxide. The planes in F1 are not distinguished.

of the F2 nanocrystal is indeed the thermodynamically stable phase.

On the other hand, for smaller nanocrystals, the interface energies have opposite behavior. In this case the spherical nanocrystal (S1) has lower interface energy than the faceted one (F1). This is an indication that facets are not any more favorable for small nanocrystals. Indeed, most groups report that faceted nanocrystals are observed only for sizes of 5 nm [56], or even 4 nm [55] and larger. For smaller diameter the nanocrystals are spherical, and their projection shape is circular.

The interface energies of all cells are shown in Table 6.3. Note that all of these energies lie within the limits defined by the energy of the ideal planar Si(001)/a-SiO_2

Table 6.3: Percentage of bridge bonds, Si suboxides and surface energy for the spherical and the faceted nanocrystal.

	% bridges	E_{bridge} (eV)	E_{inter} (eV/Å^2)
S1	63	0.38	0.073
F1	50	0.43	0.076
S2	66	0.42	0.066
F2	54	0.33	0.052

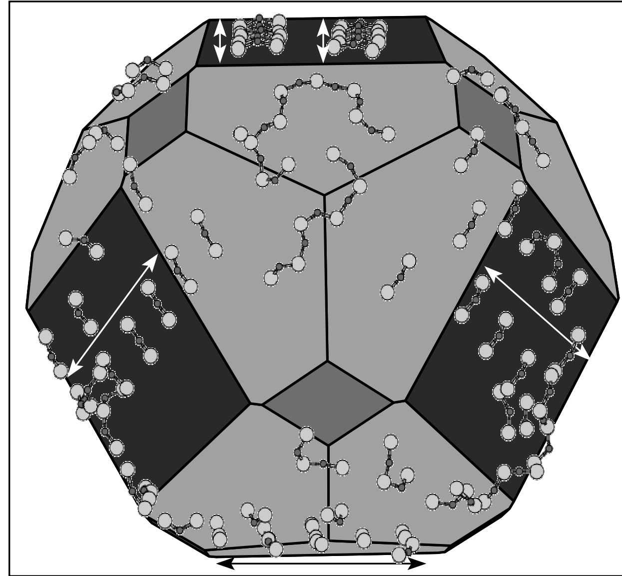

Fig. 6.7: The bridge bonds of the F2 nanocrystal drawn together with the equilibrium shape given by the Wulff method. The arrows show the directions of the bridge rows.

interface with no suboxide layers (0.046 eV) and the energy of the planar interface with suboxide layers (0.098 eV) [59, 60].

In general, it is believed that bridge bonds lower the energy, at least in planar interfaces. So, one might expect that the percentage of bridge bonds would be consistent with the interface energies of these structures. However, this does not happen. In both sizes, the percentages of bridge bonds of the spherical nanocrystals (S1 and S2) are more than in the case of faceted ones. This is because bridge bonds are not favorable for some facets. For example, the facets (110) and (111)II, as shown in Table 6.1, do not consist of any bridge bond at all. In the case of the spherical nanocrystals, bridges are formed almost uniformly on the surface of the nanocrystal.

In order to understand the above result we draw the shape of the optimum nanocrystal, just as in Fig. 6.3, together with the bridge bonds of the F2 structure. The resulting sketch is shown in Fig. 6.7 revealing a lot of interesting results. First of all, bridge bonds are formed mainly on the (100) facets. The "stripe phase" is clearly formed on some facets (for example on the (100) facet shown at the top), while in some other facets a mixture of the stripe and check phase appears. The white and black arrows show the directions of the bridge rows. To the contrary, fewer bridge bonds are formed on the (121) facets and even fewer on the (110). This is consistent with the results of the planar interfaces. Also, we should note that many bridges are joint together forming chains. These are mainly observed on the (121) facets and

rarely on the (100) facets. More specifically, they are frequently formed on the edges, connecting two different facets.

Because of the curvature of the nanocrystal and due to the fact the that spherical nanocrystal encompasses all crystal orientations, bridges have a different effect. In order to get more insight into this effect, we calculated the average energy of bridge bonds for all nanocrystals. The results are summarized in the Table 6.3.

We see that in the F1 case, bridge bonds can not overcome the effect of the edges and the apeces, despite the fact that they are the lowest energy structural elements. The energy contribution due to the edges is comparable to the surface energy terms. So, bridge bonds are formed not on a well defined facet but on the highly distorted edges. This explains the higher energy of bridge bonds on the F1 structure compared to the S1.

To the contrary, as the nanocrystal becomes bigger, the contribution of the edges becomes less important. Now, bridges are formed on well defined facets. Therefore, they are less strained than when formed on a spherical nanocrystal. So, despite the lower fraction of bridge bonds in the F2 case, its interface energy is lower than the S2 structure.

In order to confirm the above result, a deeper examination is needed. A comparison between the energy of the bridge bonds, which are formed on the facets, and the bridge bonds formed on the edges will give us a clear picture of this problem. Indeed, the energy of bridge bonds formed on the facets is found to be 0.26 eV per bond. On the other hand, the bridges formed on the edges or on the apeces have an average energy of about 0.36 eV per bond. The increase in the energy of bridge bonds of 0.1 eV is a result of the strain, which is induced by the join of different crystallographic planes.

The same trend is observed in the F1 case as well. The energy of bridges on the facets (edges) is 0.37 eV (0.43 eV). However, the energy of the bridges on the facets are quite higher compared to the energy of bridges on the larger nanocrystal F2. This is because the area of each facet is too small. So, many Si atoms participating in bridge-bond formation are located near the edges. So we observe many bridges in which the oxygen atoms bridge two Si atoms located on both sides of an edge (see Fig. 6.7). Also, the chains of bridges mainly run across the edges. In this way, the bridges are more strained and consequently they have higher energy.

Our results have provided insight and explain the experimental observations that small nanocrystals have a spherical equilibrium shape, while larger ones can be faceted. We conclude that the critical size, below which facets are not favorable, is estimated to be about 4 nm.

6.5 Conclusions

Seven different interfaces of c-Si/a-SiO_2 having different crystal orientations were constructed using a Monte Carlo approach. The WWW method was used for the amorphization of the Silicon dioxide area. Comparing these structures it is found that the energetically lowest crystal orientation for the Silicon substrate is the (100) and the closest to this one is the (121). Applying the Wulff construction method the shape of the embedded nanocrystal with the minimum surface energy was calculated, revealing a polyhedron, 42 faceted, shape. The facets, which consist this volume, are the (100), (110) and (121) ones.

The verification of the whole simulation is done by the construction of such embedded nanostructures and comparing them with spherical nanocrystals. It is found that in big nanocrystals the faceted shape is more preferable, while as the nanocrystal shrinks the equilibrium shape is spherical. This is explained by the highly strained bridge bonds in the case of small faceted nanocrystals, where edges contribute more than the surfaces. So, faceted nanocrystals might exist under some thermodynamic conditions for sizes of greater than $\sim$ 4 nm.

Chapter 7

First Principles Calculations

Silicon nanocrystals embedded in amorphous SiO_2 are constructed using a Monte Carlo approach. These structures are annealed at 800 K and relaxed to their ground state via ab-initio simulations. The electronic properties of these systems are extracted revealing the reduction of the band gap due to the highly strained nanocrystal cores and interfaces. Si-O-Si double bonds are not the dominant mechanism responsible for the red shift of photoluminescence of these structures. To the contrary, distortions of the Si nanocrystal atoms are found to play the dominant role in the size range of about 1 nm.

7.1 Introduction

Reducing the size of a semiconductor to the nanometer scale changes the physical properties of the material in a fundamental way. For example, semiconductor clusters with a diameter of a few nanometers exhibit an increased optical gap and narrower emission spectra compared to bulk values [36, 38]. Quantum confinement (QC) [36, 124] is the widely accepted model to explain this behavior of the Photoluminescence (PL). QC opens the band gap and pushes the PL in the visible for crystalline sizes below 5 nm [124].

On the other hand, many groups have reported that when the crystalline size decreases to few nanometers, the PL in air does not increase much beyond 2.1 eV, even when the crystallite size drops well below 3 nm [132]. This observation does not coincide with QC theory, which predicts a much larger opening of the band gap, in excess of 3 eV for sizes below 2 nm [124].

Many attempts were made in order to explain the red shift of the PL after the exposure to air. Most of them dealt with isolated Si nanocrystals passivated with

Hydrogen and Oxygen. Some groups [66, 39] proposed that this behavior of the PL is the result of the formation of double Si=O bonds on the surface of the nanocrystals, indicating that the excitons, responsible for the PL, are trapped in these bonds. Some others [67] proposed that the same behavior can be achieved by the formation of Si-O-Si bonds (bridge bonds). The conclusion is that oxygen related bonds are responsible for the reduction of the band gap in these systems (either Si-O-Si bridge or Si=O double bonds).

As already said, those works deal with systems of isolated nanocrystals. In this way the structural changes, which might be induced when the nanocrystals are embedded in the amorphous matrix, are neglected. These changes are possible to be produced on both the surface of the nanocrystals and the inner parts. However, these studies gave us a good estimation of the possible mechanism responsible for the red shift of PL. Also, they acted as a precursor for more realistic studies.

On the other hand, in the only previous theoretical attempt to simulate the structure of a Si nanocrystal embedded in SiO_2, a crystalline SiO_2 matrix was used [68]. In this work, it is shown that the strained interface is important for the optical properties of these systems. Using this approach, the computational load is reduced, but it is not an accurate representation of the real situation. Neither an amorphous host matrix was used nor oxygen related bonds were constructed.

Today, the consensus is that both quantum confinement effect and the interface state recombination play important role to the PL mechanism. However, there are controversial conclusions concerning the effect of these mechanisms as a function of Si nanocrystals size. Some groups [39] believe that the quantum confinement effect dominates in nanocrystals with larger sizes, while for smaller sizes the interface state effect plays a key role. On the other hand, the works of Ref. [133, 134] show that there is a critical size of nanostructures, below which the QC effect dominates, while above which the interface state effect prevails. The main task is to separate the interface effect from the quantum confinement effect in the radiative emission from the complex structured materials.

In this section, we present the first direct simulations of the Si-nc/a-SiO_2 composite system in combination with *ab-initio* calculations. An attempt for the separation of the interface state recombination effect from the quantum confinement effect is done. We find that in small sizes the Si-O-Si bridge bonds do not play an important role. To the contrary, the dominant mechanism, which is responsible for the red shift of photoluminescence, is found to be the distortions of the interface and of the core atoms of the Si nanocrystals. These distortions are produced by embedding the nanocrystal into the amorphous matrix.

7.2 Simulations

Two different types of systems were constructed in this work. The first one concerns isolated Si nanocrystals passivated by Hydrogen/Oxygen. The effect of Si=O double bonds and Si-O-Si bridge bonds on these structures is examined. The second type concerns embedded Si nanoclusters in an amorphous SiO_2 matrix. In this case, a new parameter, which has been till now neglected, shows up. This is the distortions of the Si-nc, which are produced due to the host matrix.

The initial geometries for isolated Si clusters, passivated with Hydrogen, were constructed using a diamond core structure with bulk Si-Si bond lengths. In this way, the surface atoms have one or two dangling bonds. Hydrogen is then placed along the appropriate tetrahedral direction, at a distance found from the ground state of SiH_4. In order to create a Si=O double bond, two H atoms, connected to the same Si, were replaced by an O atom. On the other hand, Si-O-Si were formed by replacing two H atoms, which were connected to different Si atoms, by an O atom. In some cases a Si atom had to be removed, in order for a bridge bond with less strain to be created.

The second type of structures were constructed with Monte Carlo simulations. We start with a cubic cell in the β-crystobalite structure containing 192 atoms (14.3Å×14.3Å×14.3Å). This periodic cell consists of 64 Si and 128 O atoms. Within a radius from the center of the cell, all oxygen atoms are removed. In this way an all-Si nanocluster is formed. Then, this unphysical initial geometry, is relaxed to its energy minimum. The energy is approximated by a Keating like valence force model. For the amorphization of the Si dioxide area, the methodology of WWW is used [74], which is based on bond-switch moves (for more details see Chapter 2). Note that the Si atoms of the nc do not take part in these flips during the whole amorphization procedure. The resulting structures are then used as input to first principles calculations, in order to extract the electronic properties of these systems.

All geometry optimization and minimization of the total energy have been performed using the VASP (Vienna *ab-initio* Simulation Package) program. The Kohn-Sham equations of the DFT have been solved with the generalized gradient approximation (GGA) based on the Perdew-Wang formulation for the exchange correlation potential [135]. For better accuracy, the projected augmented wave (PAW) potential as supplied by Kresse and Hafner was used [104]. A relatively high cutoff of 400 eV was adopted. For the Brillouin-zone integration one k-point has been used (Γ). The structure was relaxed via a conjugate-gradient algorithm until the residual forces were less than 1×10^{-3} eV/Å.

In the case of embedded nanocrystals, the model was first annealed at 800 K

via the VASP. Annealing is a well known technique in order to escape from any local minima. The ground state of the system is eventually found with a conjugate-gradient algorithm. The final structure is then analyzed.

7.3 Results

This section is constructed as follows. First, we calculate the band gaps of different sizes of Hydrogenated Si nanocrystals verifying the Quantum Confinement effect. Then, the effect of bridge bonds and double bonds on the gap is examined by passivating the nanocrystals by oxygen. Next, we present the first theoretical measurement of the band gap of an embedded Si nanocrystal in a-SiO_2. To get more insight into this effect, we decompose the contribution of bridge bonds and strained Si atoms to the density of states (DOS).

7.3.1 Hydrogenated Si-nc and Quantum Confinement

Five different sizes of Si nanocrystals were constructed. Starting with the SiH_4 cluster (zero size nanocluster), the nanocrystals gradually increase their size until about 1.3 nm, $Si_{87}H_{76}$. The density of states and the structure of each one are shown in Fig. 7.1. In the quantum confinement theory, the PL energy is blueshifted with respect to the gap of bulk silicon (E_o). Tight-binding calculations by Delerue, Allan and Lannoo found that this shift as a function of the particle diameter d is described by a power law with a characteristic exponent equal to -1.39 [129]:

$$E_{PL}(d) = E_o + \frac{3.73}{d^{1.39}} \tag{7.1}$$

where d is measured in nm. Wang and Zunger [130] found a very similar expression for the shift of PL. Their exponent was equal to -1.37:

$$E_{PL}(d) = E_o + \frac{3.77}{d^{1.37}} \tag{7.2}$$

Our results for the band gap energies as a function of the nanocrystal size are shown in Fig. 7.2. It is obvious that the gap shrinks, as the size of the cluster increases, approaching the value of the bulk Si. The solid curve represents a simple fit of these results. The theoretical results of Delerue *et al.* [129], and of Wang *et al.* [130] are also shown in this figure (dotted and dashed curve, respectively). It is clear that the isolated Si nanocrystals passivated only by Hydrogen follow the quantum confinement trend. However, it is well known that Density Functional Theory band calculations underestimate the band gap. This explains the lower band gap energies

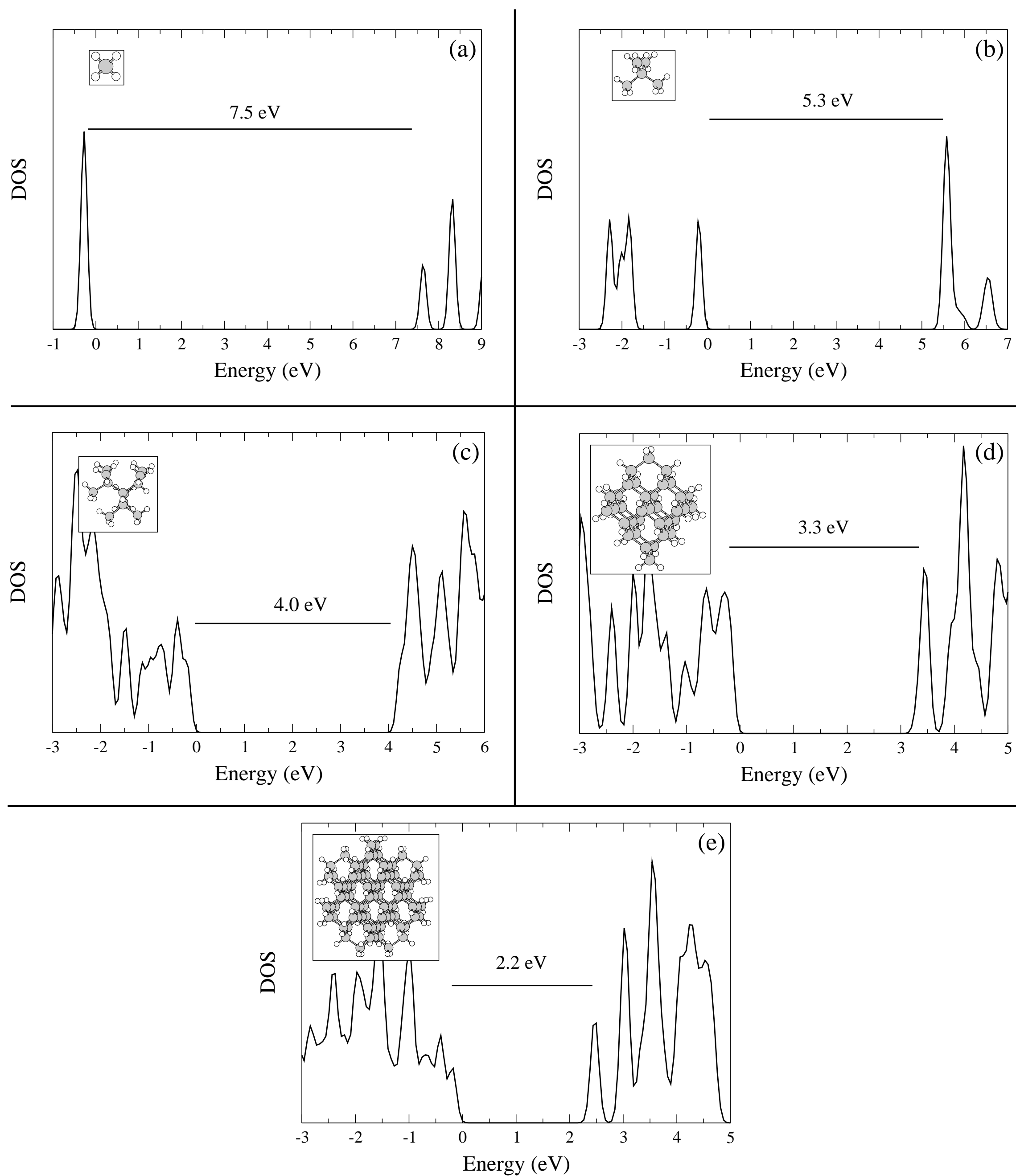

Fig. 7.1: GGA calculated density of states of a (a) SiH_4, (b) Si_5H_{12}, (c) $Si_{13}H_{28}$, (d) $Si_{35}H_{36}$, and (e) $Si_{87}H_{76}$ cluster. Gray (white) spheres denote Si (H) atoms.

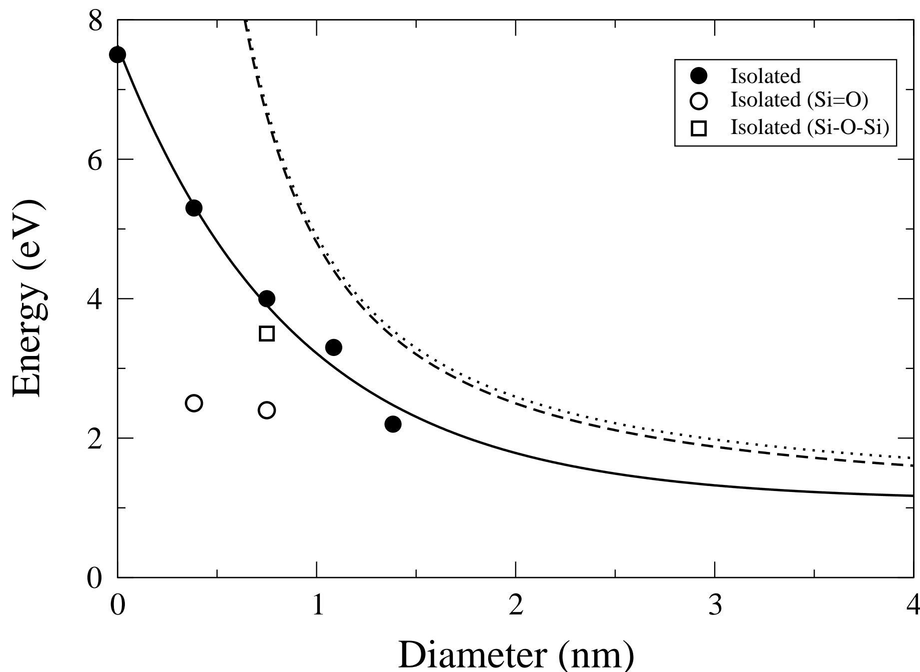

Fig. 7.2: Energy gap versus diameter (nm) for hydrogen passivated Silicon nanoclusters with (open symbols) and without (filled symbols) oxygen. The nanocrystals with a Si=O double bond are marked with open circles, while the one having a Si-O-Si double bond is marked with open square. The solid curve represents a simple fit of our results, whereas the dotted curve represents the theoretical result of Delerue, Allan, and Lannoo [129], and the dashed curve shows the result of Wang and Zunger [130].

of our structures with respect to the expected values given by the Eq. 7.1. Note that our results are in very good agreement with the analogous work by A. Puzder *et al.* [66], who also carried out LDA-GGA calculations on isolated Si-nc.

7.3.2 Hydrogenated Si-nc with Oxygen

Much effort has been devoted to the understanding of the reduction of the PL after the exposure of samples to air. To date, it is accepted that oxygen states (either Si=O double bonds or Si-O-Si) create states in the gap reducing it dramatically. In order to verify this result, new structures were constructed having either the first type of O bonds or the second type.

First, the effect of double bonds is studied. Two new structures were constructed having a double bond. The first one was the Si_5OH_{10} with diameter ~0.4 nm, while the second one was the $Si_{13}OH_{26}$ cluster having size of about 0.75 nm. The calculated

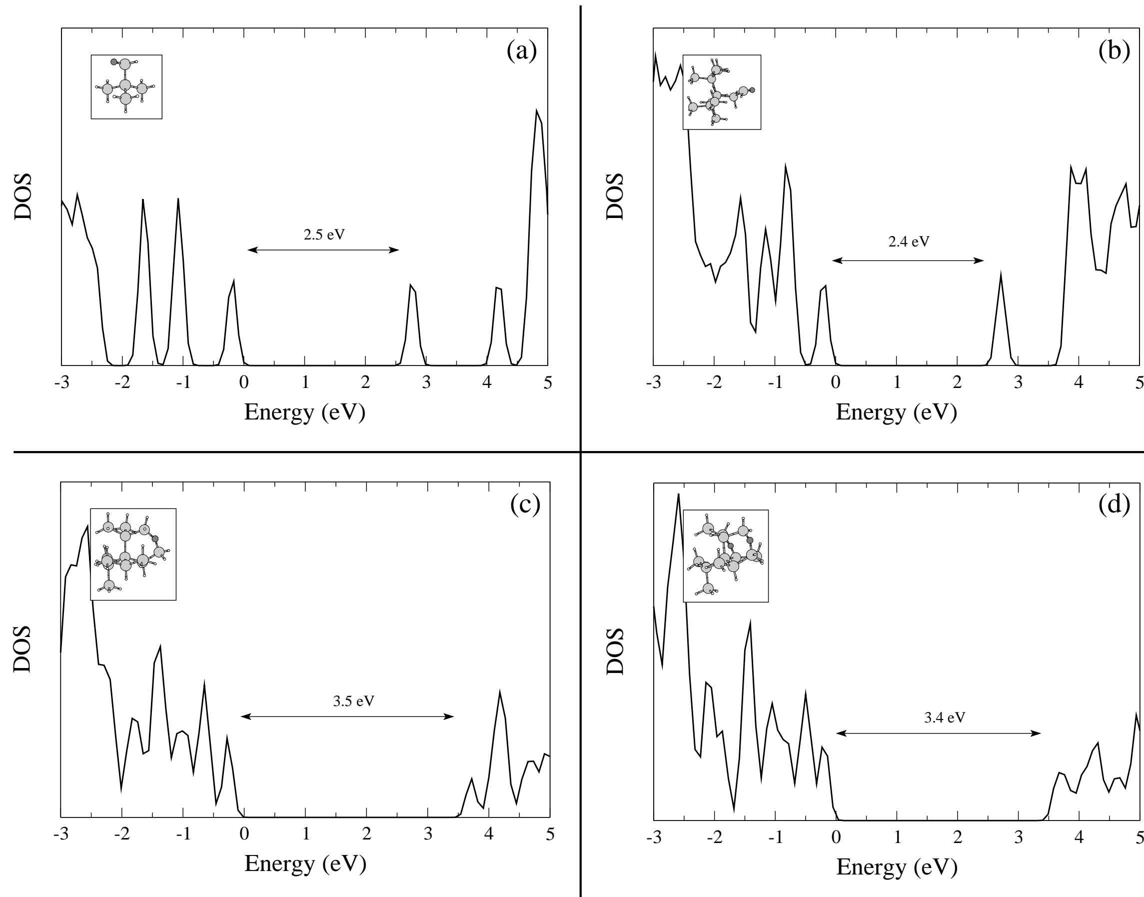

Fig. 7.3: GGA calculated density of states of a (a) Si_5OH_{10}, (b) $Si_{13}OH_{26}$, (c) $Si_{13}OH_{26}$, (d) $Si_{13}O_2H_{24}$ cluster. (a) and (d) are structures having double bonds, while (c) and (d) have bridge bonds. Light gray balls represent Si, dark gray spheres denote O and white stands for H atoms.

DOS and their structures are shown in Fig. 7.3(a) and (b). Their band gaps are also filled in Fig. 7.2, revealing an important red shift of the energy gap, with respect to their initial structures, which had no oxygen bonds. These results are in quantitative agreement with those of Ref. [66, 39]

On the other hand, one bridge bond is formed on the $Si_{13}H_{28}$ nanocrystal reducing the gap by 0.5 eV. This reduction is low compared to the reduction induced by the double bond. Also, creating multiple bridges on the same nanocrystal has slightly effect in the energy gap, Fig. 7.3(c) and (d). On the contrary, Vasiliev *et al.* [67] observed that there is no change in the size of optical gaps between cluster isomers with Si=O and Si-O-Si bonds on the surface.

Table 7.1: Characteristics of the structures S1 and S2.

	S1	S2
Size (nm)	0.75	1.10
N_{total}	180	141
N_{Si}	64	64
N_O	116	37
Si cont. (%)	35.6	45.4
N_{nc}	13	40
N_{surf}	11	24
Bridge bonds	2	10
% Bridge bonding	36	50

7.3.3 Embedded Si nanocrystals in a-SiO_2

Wang *et al.* [133] tried to separate the interface state recombination effect from the quantum confinement effect in PL signals from Si-rich oxide material systems. They conclude that there is a critical size of nanocrystals, below which the quantum confinement effect dominates, and above which the interface state effect prevails. They showed that this transition happens in a narrow Si content between 42 to 44 %. On the other hand, some other groups [39] believe exactly the opposite.

In order to resolve the controversy, concerning the origin of PL mechanism, two different structures were constructed applying the above methodology. Despite the fact that the total Si content of these structures were 35.6% and 45.4%, values which are below and above the transition value proposed in Ref. [133], their sizes are too small (0.75 nm and 1.1 nm respectively) in order to observe this transition. The two structures will be named as S1 and S2 for abbreviation. The characteristics of these two samples are given in Table 7.1.

As already said, oxygen bonding is believed to play the most important role concerning the red shift of PL in isolated Si-nc. In the S1 structure only two bridge bonds have been created, while in the S2 ten bridge bonds exist. However an interesting property is the percentage of bridge bonds on the surface of each nanocrystal. A Si atom is indicated as a surface atom if it has oxidation number 1, 2 or 3. So, the small nanocrystal has 11 surface atoms while the bigger one has 24. On the other hand, the Si atoms which take part on bridge bonds are 4 and 12 for the S1 and S2 structures, respectively. In this way the percentage of bridge bonding is found to be 36 (50) % for the S1 (S2) structure. This result is in agreement with our previous

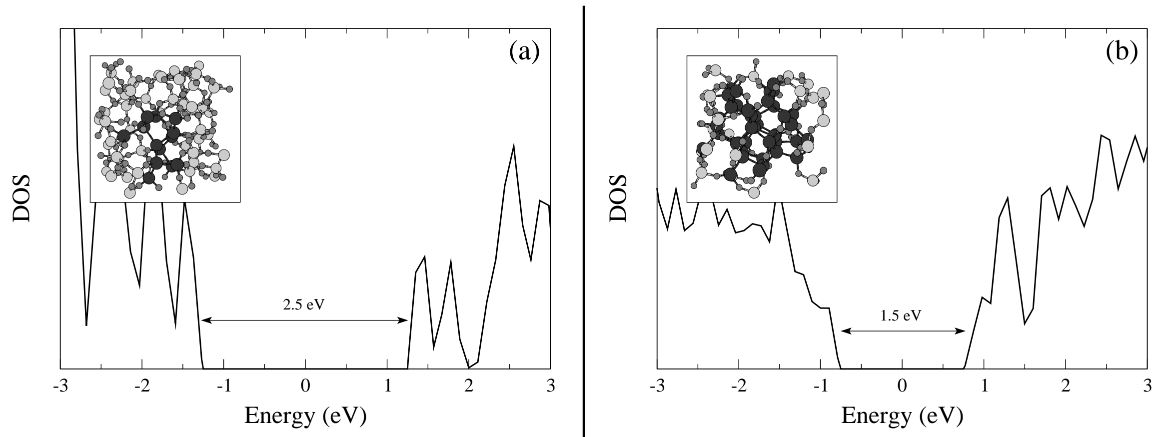

Fig. 7.4: GGA calculated density of states of the embedded Si clusters in a-SiO_2. S1 and S2 in panels (a) and (b), respectively.

finding in Chapter 5, namely that the fraction of bridge bonds strongly declines as the size gets smaller.

The final structures with the corresponding density of states are shown in Fig. 7.4. In (a) the S1 structure is illustrated with a band gap energy of 2.5 eV. The isolated nanocrystal of the same size has band gap of 4.0 eV (Fig. 7.2). On the other hand, in (b) the S2 has a smaller gap of 1.5 eV. In this case the isolated nanocrystal should have gap of about 3.0 eV. So, the reduction of the gap in both cases is of the order of 1.5 eV.

In order to get more insight into this result, we have to separate the contribution to the energy gap from the quantum confinement effect and from the interface state effect. This is done in three steps. In the first one, we isolate the nanocrystals from the amorphous matrix. This is possible by removing the atoms of the amorphous matrix and replacing the terminating oxygen atoms of the nanocrystals with Hydrogen. In this step, the oxygen atoms of bridge bonds were not replaced by H. The resulting isolated structures (having bridge bonds) are the $Si_{13}O_2H_{24}$ (B1) and $Si_{40}O_{10}H_{38}$ (B2). Then, the resulting structures were relaxed via a conjugate-gradient algorithm and the ground state of these nanocrystals were found. In this minimization procedure the Si atoms of the nanocrystals are kept fixed. By doing this the strain, which has been induced on the nanocrystal, is preserved.

Fig. 7.5 shows the B1 and B2 structures and the corresponding density of states. Both of them exhibit a small increment of band gap energy, with respect to the embedded case S1 and S2, respectively, by 0.1 eV. The host matrix applies constrains on the nanocrystal atoms at the interface, resulting in this small reduction of the

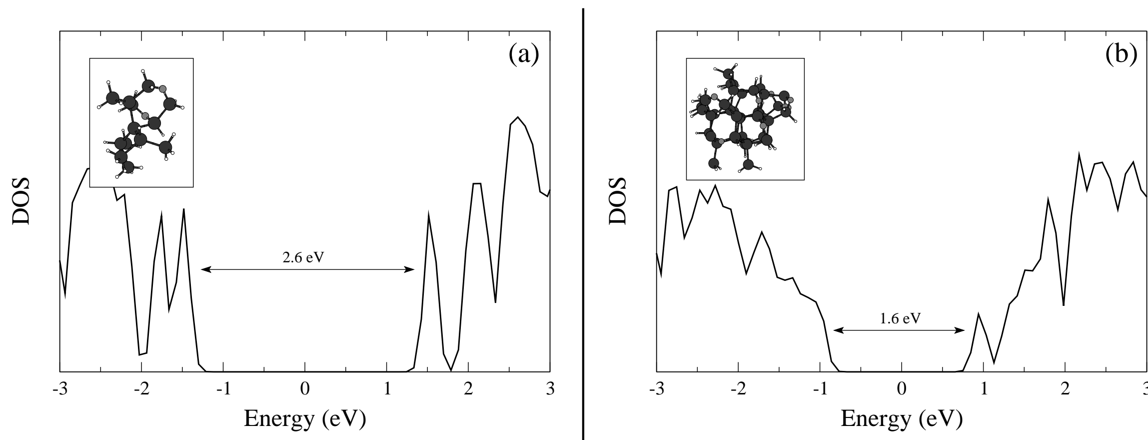

Fig. 7.5: GGA calculated density of states of the distorted isolated Si clusters with bridge bonds. B1 and B2 in panels (a) and (b), respectively.

band gap. By removing the amorphous matrix and passivating the nanocrystals with H the constrains disappeared. The conclusion from this step is that the amorphous matrix does not directly affect the band gap of these systems.

In the second step, each oxygen atom of all bridges is replaced with two Hydrogen atoms in the appropriate distances. Again the structure is relaxed conserving the strain on the Si atoms. The new isolated structures, which are passivated only by H, are the $Si_{13}H_{28}$ (I1) and $Si_{40}H_{58}$ (I2). In this way, the effect of bridge bonds on the band gap can be revealed.

Indeed, from the resulting electronic properties, which are shown in Fig. 7.6, it is clear that Si-O-Si bridge bonds do not affect the energy gap. Removing 2 (10) bridge bonds from the B1 (B2) structures the bang gap remained unchanged. Note that in the *ideal* isolated nanoclusters bridge bonds reduce the gap, as shown in the previous section and in Ref. [67]. Also, it is clear that the distorted isolated nanoclusters I1 and I2, have a smaller gap, with respect to the *ideal* H-passivated Si-nc. These results give us the opportunity to conclude that the red shift of PL in the embedded Si-nc case is produced because of the distortion, which appears at the interface and even the core of the nanocrystal. To the contrary, bridge bonds have no effect in the band gaps, at least in the size range which we have been focusing.

The amorphous matrix has been modeled as a defect-free network in which Si and O have four and two bonds, respectively, without any O-O bonds or even any Si=O double bonds. Despite that the structure was annealed with the VASP program, neither a double bond nor a O-O bond was created. In order to examine the effect of double bonds we proceeded in the third step.

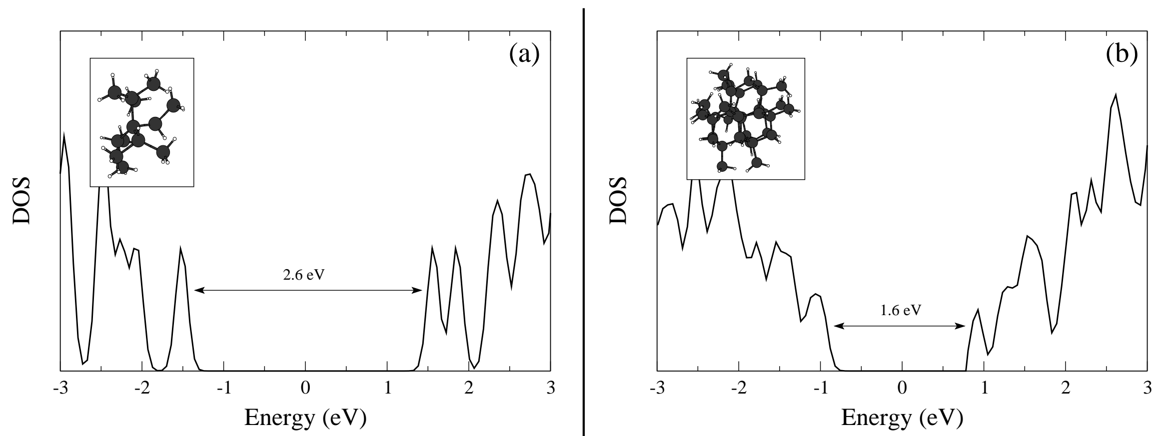

Fig. 7.6: GGA calculated density of states of the distorted isolated Si clusters passivated only by H. I1 and I2 in panels (a) and (b), respectively.

Starting from the isolated distorted Si nanocrystals, I1 and I2, we produced a double bond in each nanocrystal. This is done just as in the case of the *ideal* nanocrystals. Two H atoms were replaced by an O atom, which is placed in the appropriate distance. Again, the conjugate-gradient algorithm is used to find the ground state of the new system. The Si atoms of the nanocluster are not allowed to move. The new distorted isolated Si nanoclusters with double bonds are the $Si_{13}OH_{26}$ (D1) and $Si_{40}OH_{56}$ (D2).

The final structures and their corresponding density of states are shown in Fig. 7.7. It is clear that double bonds reduce the gap, with respect to the I1 and I2 cases. In the large nanocrystal the reduction is imperceptible (0.1 eV), while in the small nanocrystal the band gap energy is decreased by 0.7 eV. This is a clear result that in the distorted nanocrystals double bonds produce pinning states in the gap, while bridge bonds do not. This effect is more substantial in the smaller nanocrystal than in the larger one.

On the other hand, the energetics of all isolated nanoclusters, which are examined, are given in Table 7.2. “Distorted” nanocrystals are named those having distortions, implied by the amorphous host matrix (just as in I1 and D1 cases), while the “ideal” nanoclusters have diamond core structure with bulk Si-Si bond lengths (see Fig. 7.3).

It is clearly that the distorted structures have always higher energy with respect to the ideal structure of the same system. The most important finding is that for these structures, bridge bonds have lower energy than double bonds. This finding can be used as a clue that double bonds are not so favorable as bridge bonds are.

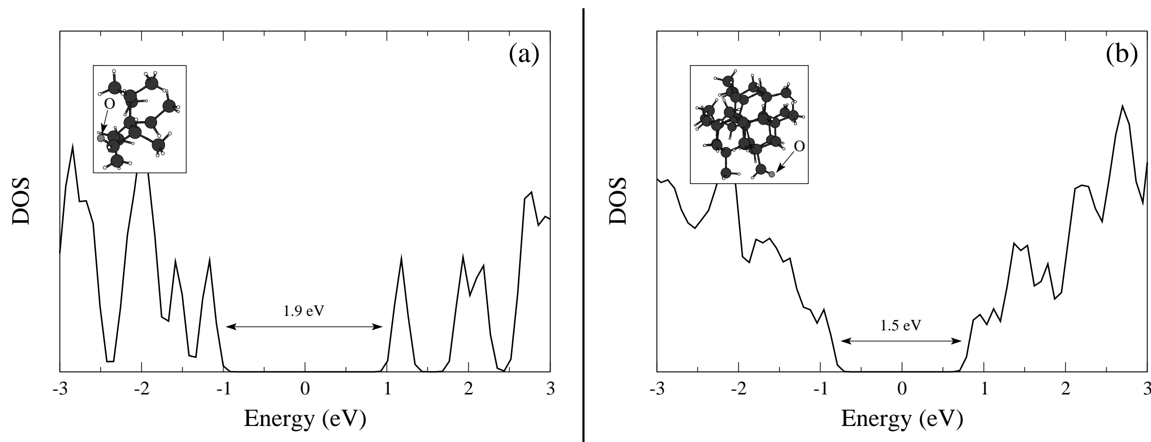

Fig. 7.7: GGA calculated density of states of the isolated Si clusters with distortions and with one double bond.

However, a more intensive search is needed.

Table 7.2: Total energies of isolated Si-nc with/without oxygen.

	$Si_{13}H_{28}$	$Si_{13}OH_{26}$		$Si_{13}O_2H_{24}$	
		1 Si=O	1 Si-O-Si	2 Si=O	2 Si-O-Si
Ideal	-164.03	-164.19	-166.65	-163.56	-168.57
Distorted	-162.58	-162.12	-164.99	-161.59	-167.11

7.4 Conclusions

The effect of bridge bonds and of double bonds were first investigated in the Hydrogen passivated Si nanoclusters. It is found that double bonds can reduce more dramatically the energy band gap than the Si-O-Si bridge bonds.

Two Silicon nanocrystals embedded in amorphous SiO_2 were then constructed using an efficient Monte Carlo approach. The first one had a diameter of about 0.75 nm, while the second one was 1.1 nm in size. Both of them consist of bridge bonds (2 and 10, respectively). The ground state of these structures were found via the VASP (Vienna *ab-initio* Simulation Package) program. A great reduction of the band gap of these structures, with respect to the isolated nanocrystals without oxygen states, were observed.

In order to examine the influence of the amorphous matrix in the gap, the distorted nanocrystals were extracted and passivated by H. The bridge bonds and the distortions are preserved while the H atoms are moved to their ground state. An increment of about 0.1 eV is observed in these structures. This means that the host matrix adds some constrains to the surface Si atoms, which as a result affects slightly the band gap.

Next, the effect of bridge bonds and of double bonds on these distorted isolated Si nanocrystals are studied. Bridge bonds are found to have negligible contribution to the band gap. They do not create any states in the gap. This is because distortions have more substantial effect than bridge bonds. On the contrary, double bonds reduce further the energy gap of the isolated distorted nanocrystals. The smaller the nanocrystal, the more effect a double bond has.

Appendices

Appendix A

Optical Properties

The electronic and the optical properties of different systems are studied in this chapter. For the calculations, the VASP ab-initio program has been used. More specifically, the properties of c-Si, a-Si, c-SiO_2, and of two embedded Si nanocrystals in an amorphous SiO_2, with different Si contents, are reported.

A.1 Introduction

In this appendix the properties of simple structures, c-Si and c-SiO_2, and some more complicated, i.e. embedded Si-nc in a-SiO_2, are calculated. The calculations are mainly carried out via the VASP *ab initio* program. Using this simulation package the density of states and the dielectric function, both real ϵ_1 and imaginary part ϵ_2, can be extracted. The absorption coefficient can be very easily extracted by the well known equations:

$$\epsilon_1 = n^2 - k^2 \tag{A.1}$$

and

$$\epsilon_2 = 2nk \tag{A.2}$$

where, the quantities n and k are collectively called the "optical constant" of the solid. n is the index of refraction and k is the extinction coefficient.

In the high-absorption region (where absorption is associated with interband transitions), the form of the absorption coefficient α(E) was given in quadratic form by Tauc *et al.* [136] and discussed in more general terms by Davis and Mott [137], who use the equation of the form:

$$\alpha(E) = \frac{B(E - E_g)^r}{E} \tag{A.3}$$

where B is a constant, E_g is the optical band gap, $\alpha(E)$ is the absorption coefficient at an energy E, and r is an index which can assume values of 0.5, 1.5, 2 and 3, depending on the nature of the electronic transitions responsible for the absorptions. r is equal to 0.5 for allowed direct transitions, 1.5 for direct forbidden transitions, 2 for allowed indirect transitions and 3 for forbidden indirect transitions.

Fundamental absorption edge in most amorphous semiconductors follow an exponential law. Above the exponential tail, the absorption coefficient of any amorphous semiconductor has been observed to obey an equation similar to the above equation. Although it is very difficult to determine the exact value of the exponent r, it is obtained that r=2 for most amorphous semiconductors. In this notation, the value of E_g is obtained by plotting $(\alpha E)^{1/r}$ versus E and extrapolating the linear region of the plots of $(\alpha E)^{1/r}$ to zero. This extrapolated value is used to define the so-called optical gap in amorphous materials.

Another interesting property is the Urbach energy. The exponential behavior of α(E) can be described with:

$$\alpha(E) = \alpha_0 \exp\left[\frac{E}{E_U}\right] \tag{A.4}$$

where E_U is the Urbach energy. It reflects the shape of the valence band tails and therefore it varies with the structural disorder. So, it is used for the characterization of the disorder in the samples. Urbach energy can be calculated via the equation:

$$E_U^{-1} = \frac{d[\ln\alpha]}{dE}\bigg|_{E_{03}} \tag{A.5}$$

where E_{03} is the energy at which the absorption coefficient has the value 10^3 cm^{-1}.

A.2 Results

A.2.1 Bulk Si

One of the first systems explored, using the VASP program, was the bulk c-Si. Using the primitive unit cell, which contains a basis of two atoms, electronic and optical calculations were performed. The geometry optimization was performed via a GGA exchange-correlation treatment. The kinetic energy cutoff was set at 250 eV and a grid of $21\times21\times21$ k points was used. Also, a total of 100 bands were considered.

More specifically, in Fig. A.1, some of the properties of this system are shown. First of all, the electronic density of states (a) is calculated revealing the band gap of

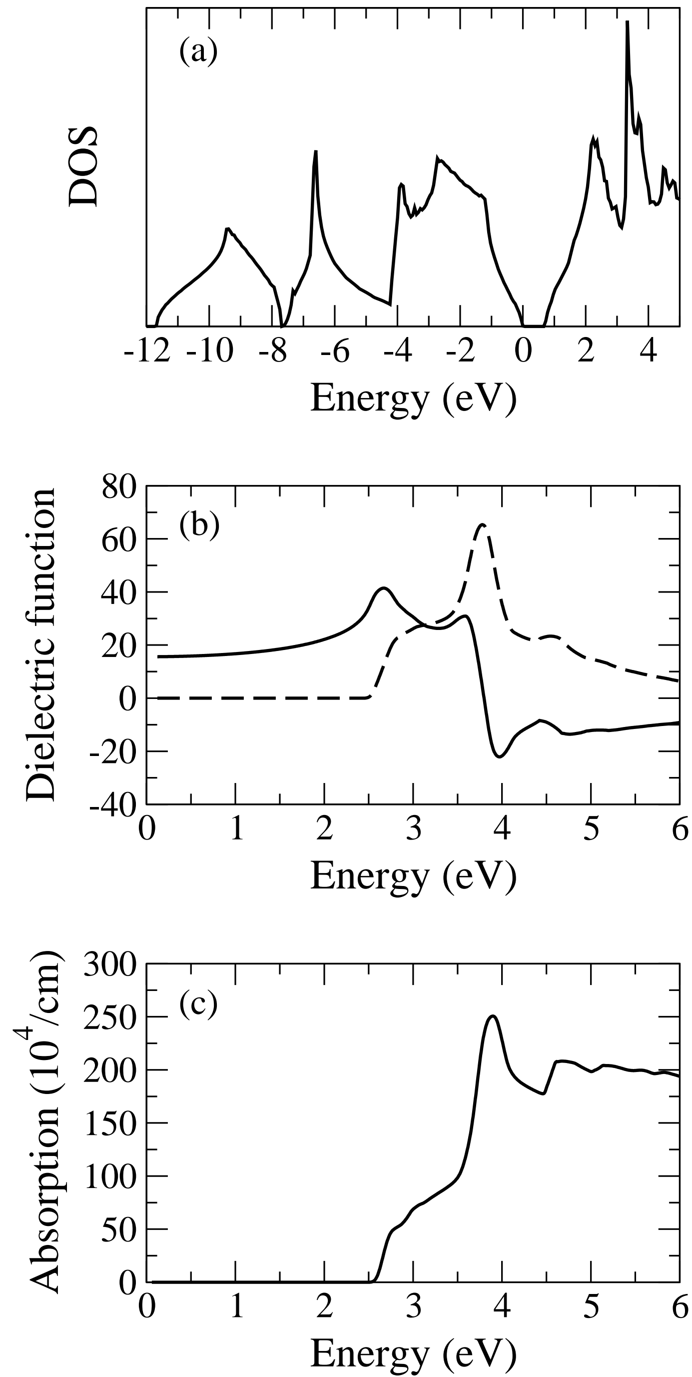

Fig. A.1: Electronic and optical properties of bulk c-Si. (a) Density of states, (b) real (solid line) and imaginary part (dashed line) of dielectric function, and (c) the absorption coefficient.

Si, 0.86 eV. It is well known the under-estimation of the band gap of Si, using either LDA or GGA. Next, the dielectric function, both the real and the imaginary part, is shown in (b). Finally, the absorption coefficient α of c-Si is illustrated in (c). Note that the onset of the absorption happens at the correct value of 2.52 eV (which is, for c-Si, the GGA direct transition at Γ).

A.2.2 Amorphous Si

An amorphous structure of 64 Si atoms was constructed with the WWW method (see Chapter 2). First, an annealing procedure, with the VASP program, at 800 K is applied. Then, the ground state of the system is found via an efficient conjugate-gradient algorithm. The properties of the resulting structure are shown in Fig. A.2.

From the density of states a band gap of about 0.4 eV is found. A reduction of about 0.45 eV from the crystalline case. On the other hand, the Tauc gap is found to be $E_{Tauc} = 0.47$ eV, a little higher than the direct calculation of the gap through the density of states. Finally, the Urbach energy of this system has been calculated $E_U = 140$ meV. In experiments the Urbach energy varies from 50-100 meV for a-Si.

A.2.3 Bulk β-cristobalite SiO_2

The structure of beta cristobalite is analogous to the structure of diamond. Diamond is composed of pure carbon, but each carbon atom has four identical bonds that connect to other carbon atoms. These bonds lay as far apart from each other as four bonds can get in three dimensions or in a tetrahedral shape. By replacing the tetrahedrons in the diamond structure with the tetrahedrons of SiO_4, we get approximately the structure of beta cristobalite. In the idealized structure the Si-O distance is 1.54 Å and the Si-O-Si angle is 180°.

A conventional cubic cell of 24 atoms was used. Eight of them were Si and the rest of them (16) were O. The cell had a size of 7.16Å×7.16Å×7.16Å. The kinetic energy cutoff was set at 400 eV and a grid of 11×11×11 k points was used.

From the density of states (a) the band gap of the β-crystobalite structure is extracted, 5.84 eV. Note that from the absorption coefficient, (c), the gap is also 5.84 eV, clearly shown in the inset.

A.2.4 Embedded Si Nanocrystals

Two different Si nanocrystals embedded in amorphous SiO_2 were constructed. The first one has a diameter of 0.75 nm and a total Si content of 35.6 % (S1), while

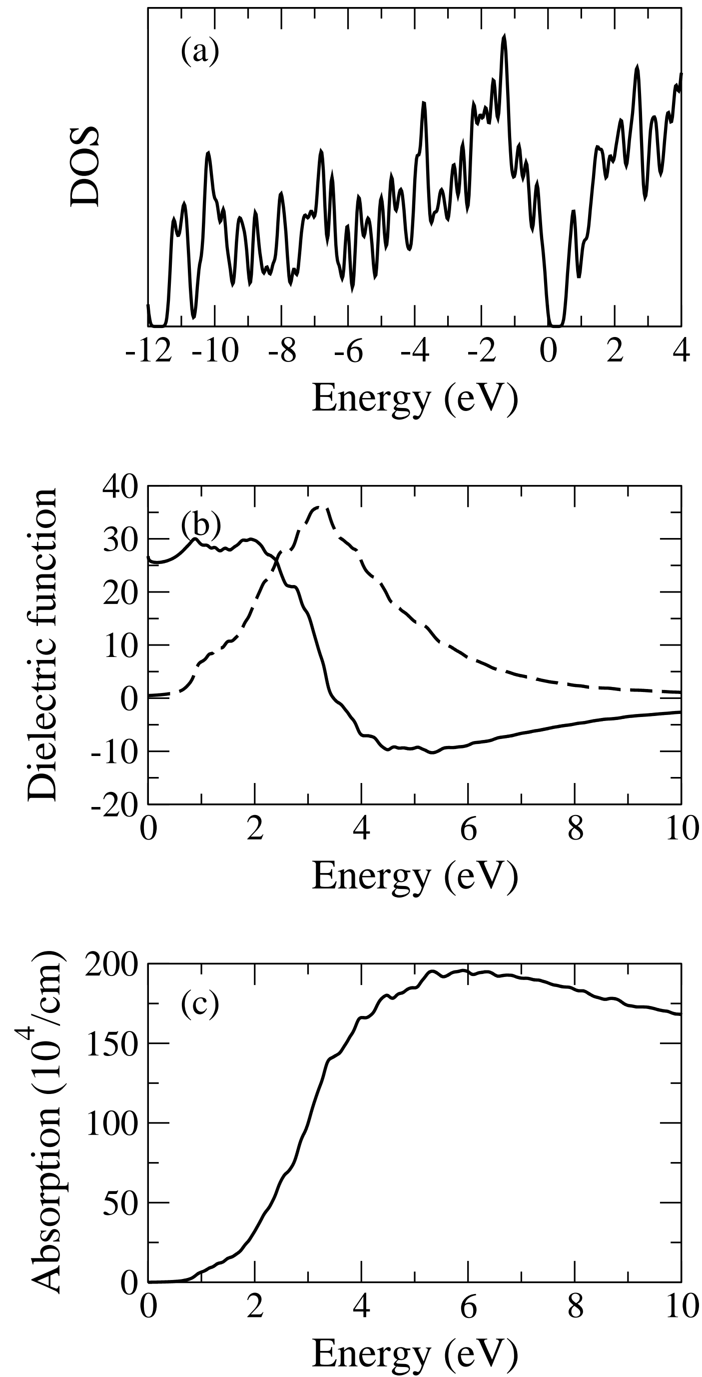

Fig. A.2: Electronic and optical properties of a-Si. (a) Density of states, (b) real (solid line) and imaginary part (dashed line) of dielectric function, and (c) the absorption coefficient.

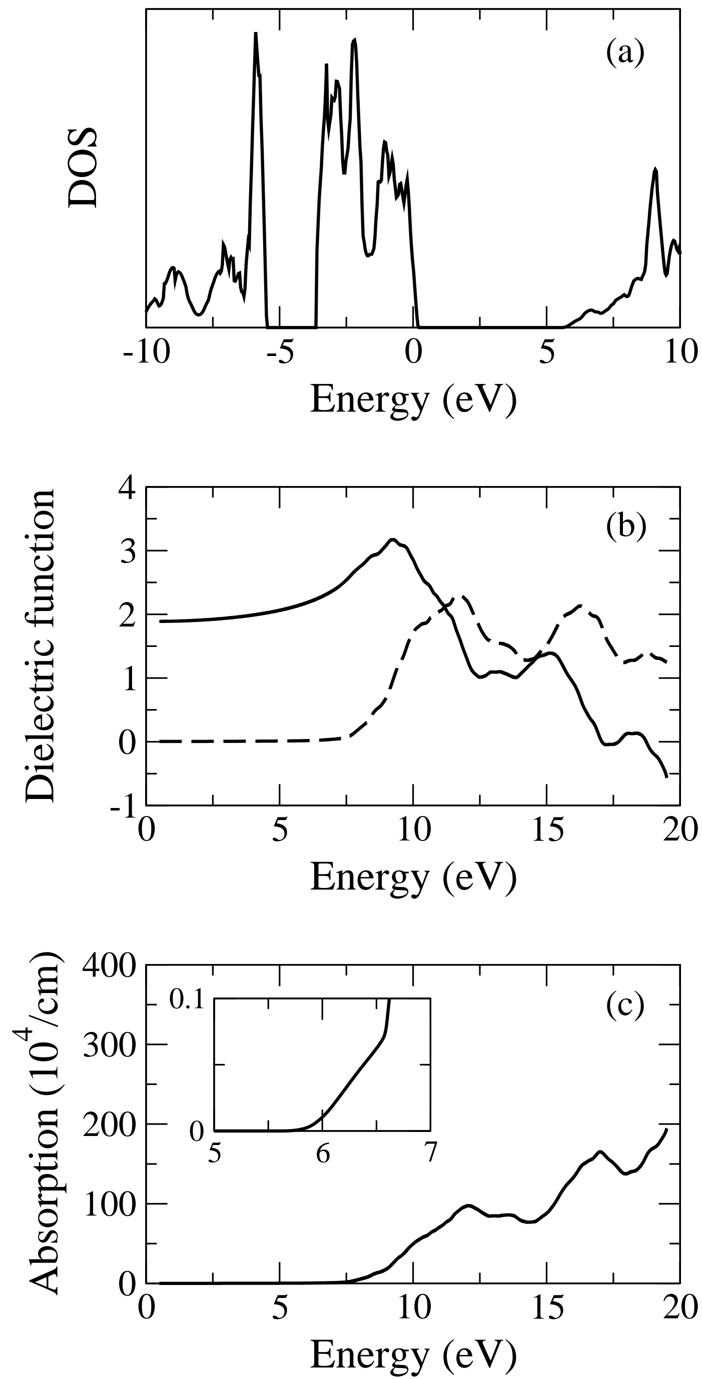

Fig. A.3: Electronic and optical properties of bulk β-cristobalite SiO_2. (a) Density of states, (b) real (solid line) and imaginary part (dashed line) of dielectric function, and (c) the absorption coefficient.

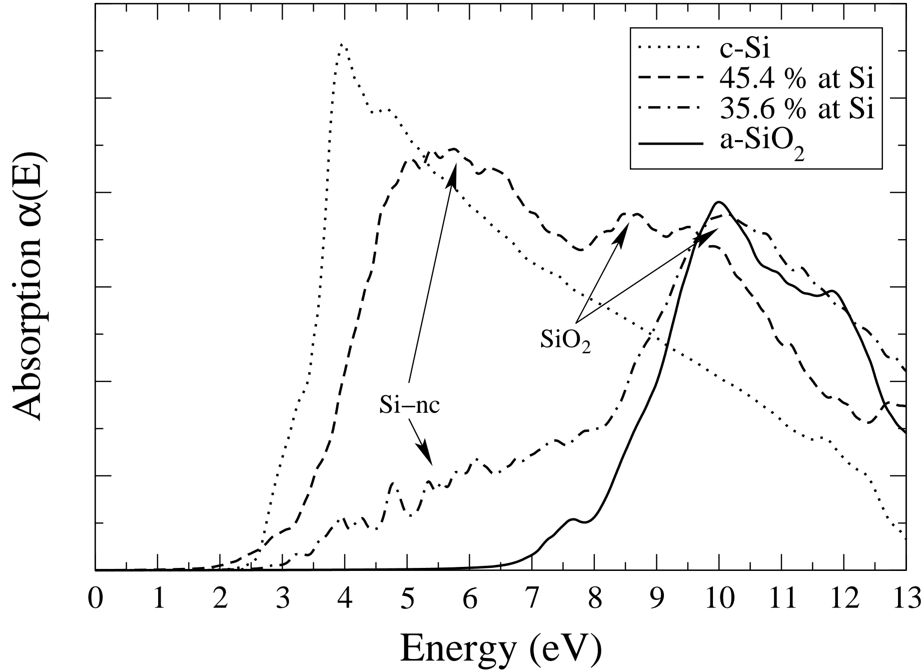

Fig. A.4: Absorption coefficient α(E) for four different samples (c-Si, S1, S2 and a-SiO_2 structures).

the seconds one size was about 1.10 nm with a total Si content of 45.4 % (S2). The exacts characteristics of these samples have been shown in Table 7.1. The absorption of these samples has been calculated and will be presented in this section.

In Fig. A.4 the absorption coefficient α(E) of those two samples is shown. Also, the absorption spectra of the crystalline Si and amorphous SiO_2 has been drawn for comparison. For the a-SiO_2 sample, an initial cubic periodic cell of 192 total atoms in β-crystobalite has been used. The amorphization has been accomplished with the methodology of WWW [74], which has been extensively used and described throughout this thesis (Chapters 2, 5, 6 and 7).

Let us discuss first the region of the low energy edge. In this region, the relative intensity of the absorption coefficient depends on the fraction of Si atoms clustered in Si-nc with respect to those coordinated to O in SiO_2. This contribution grows with increasing the Si content. On the other hand, it is obvious that the second position of the S1 and S2 samples corresponds to the a-SiO_2 contribution. In this case the contribution of the a-SiO_2 area is proportional to the Si content.

List of Figures

1.1 Schematic representation of Stranski-Krastanow growth. (a) The bare Si(001) substrate is shown while the first atoms (or clusters of atoms) of Ge are going to be deposited on the surface. (b) Ge atoms wet the substrate without forming any island until a critical thickness of this *wetting layer*. (c) Dots are formed. 3

1.2 Schematic representation of Vollmer-Weber growth. (a) The bare Si(100) substrate. (b) Islands are formed immediately, without the formation of a 2D wetting layer. (c) Further deposition wets the rest surface and covers the already formed island. 4

1.3 Typical Ge island shapes, obtained by STM, during Si capping of Ge domes, grown on Si(001): (a),(b), domes; (c) pyramids; (d)-(f) prepyramids. The Si coverages are 0, 1, 2, 4, 8, and 16 ML's for panels (a)-(f). Taken from Ref. [7]. 5

1.4 Size distribution of several island types, during deposition of Ge on Si(001). The inset shows the time evolution of the island density for different types. Adapted from Ref. [11]. 6

1.5 Comparison between experimental and theoretical PL energies as a function of crystalline size. The upper line is the free exciton band gap and the lower line is the lowest transition energy in the presence of a Si=O bond. In zone I the PL peak energies are identical, whether the samples have been exposed to oxygen or not. Adapted from Ref. [39]. 10

1.6 A magnification of a particular Silicon Nanoparticle in a sample with diameter of 160 Å. {100}, {111} and their equivalent facets are identified. Adapted from Ref. [55]. 12

1.7 Planar interface Si(100)/a-SiO_2. Two very close energetically structures, stripe (a),(b) and check (c),(d) phase. Arrows indicate bridge bonds. The black (light gray) balls represent Si atoms in substrate (a-SiO_2) while smaller dark gray atoms denote O. 13

1.8 Schematic illustration of the chemical composition of the transition layers based on the model of Ref. [63]. 14

1.9 Three different types of isolated Si nanocrystals passivated with H. In panel (a) the nanocrystal is terminated only with H ($Si_{35}H_{36}$), in (b) has one Si=O double bond ($Si_{35}OH_{34}$), and in (c) has one Si-O-Si bridge bond ($Si_{34}OH_{34}$). The light gray atoms stand for Si, the white ones for H and the dark gray for O. 15

1.10 Top view of the relaxed structure for the Si_{10}/β-SiO_2 supercell. The white and the gray balls stand for the Si and O atoms of $SiO_2\beta$, the black ones for the Si atoms of the nanocrystal. 16

2.1 Different simulation methods. 20

2.2 Schematic representation of canonical ensemble. The number of particles, the volume and the temperature of the system are kept fixed, (N,V,T). 23

2.3 Schematic illustration of the Isobaric-Isothermal ensemble. The number of particles, the pressure and the temperature of the system are kept fixed, (N,P,T). 25

2.4 Isobaric-Semigrand ensemble. The total number of particles, the pressure, the temperature and the differences of chemical potentials between different types of atoms are kept fixed, (N,P,T,$\Delta\mu$). 26

2.5 Two different types of switching move: (a) two distant random atoms and (b) two nearest neighbors exchange identities. 27

2.6 An identity switch of a site from being Si to C, produces strained bonds. In order to make the flips less costly, appropriate relaxations of first nearest neighbor atoms are applied. 28

2.7 Bond Switch move. The elementary rearrangement applied by Wooten *at al.* [74]. 29

2.8 Three snaps of the Wooten-Winer-Weaire simulation. (a) The initial supercell of crystalline Si and its pair distribution function g(r) which is consisted of delta functions. (b) The supercell at high temperature. The characteristics of a liquid structure are observed in the g(r). (c) The final structure of the simulation. Note that the third peek in g(r) is missing. 31

2.9 Bond Conversion move. A Si-Si bond is converted to a Si-O-Si bond and vise versa. The total number of atoms in this way remain fixed. . 34

2.10 An illustration of the Wulff construction method. 40

2.11 Schematic illustration of a pseudopotential and pseudo-wave. 45

3.1 Schematic of a multifaceted dome island used in the simulations. Different facets are shown by arrows. 50

3.2 Top panel: Variation of hydrostatic stress in the base layer (circles, solid line) of a non-alloyed dome and in the top substrate layer (squares, dashed line), along a line passing through the island base center. Bottom panel: Stress map of the dome island. A thin slice cut through its center is shown. 52

3.3 Vertical variation of Ge content in the intermixed island. Solid line is a guide to the eye. 53

3.4 Composition profiles in a pyramidal (left) and a dome island (right). Panels (a), (c) portray thin slice cuts through the center of the islands. Panels (b), (d) show the base layers. 54

3.5 Stress maps of an alloyed dome. (a) The whole cell. (b) The dome base layer. 56

4.1 Scheme of spatial dot compositions. (a) is taken from Ref. [117] while (b) is derived in Ref. [119]. 60

4.2 Variations of average stress layer-by-layer in (a) the dot and (b) the substrate at 625 K. Layere numbered 1 denotes the base in the dot and the top layer in the substrate. Squares (diamonds) show variation in cell with 0.16 (0.36) ML C. As a reference, the bare variation in the dot is also shown (circles). Positive (negative) sign indicates compressive (tensile) stress. 63

4.3 Probability distribution of stresses in the base layer of the dot. Sign of stress as in Fig. 4.2. 64

4.4 Atomic sites shaded according to their local stress. Filled spheres, compressive; open spheres, tensile. (a) Base dot layer. (b) Second dot layer. (c) Top substrate layer. (d) Second substrate layer. Solid lines (guide to the eye) enclose the areas below the island. 65

4.5 Atomic sites shaded according to their average accupancy. Open spheres show Si atoms, gray spheres denote Ge atoms, and black spheres show C atoms. (a) Base dot layer. (b) Second dot layer. (c) Top substrate layer. (d) Third substrate layer. Solid lines (guide to the eye) enclose the areas below the island. 67

4.6 Carbon content in substrate layers. Layer numbered 1 denotes the top layer. Solid (dashed) line shows variation in cell with 0.5 (1.6) ML Ge. The C coverage is 0.36 ML. 68

4.7 Vertical variation of Ge content in the intermixed island. Squares (diamond) show variation with 0.16 (0.36) ML C. The drawn lines are just guide to the eye. 69

5.1 Ball and stick model (part of a thin slice cut) of a Si-nc embedded in a-SiO_2. Dark spheres show Si atoms in the nc. Large (small) grey spheres show Si (O) atoms in the oxide, respectively. Arrows indicate the formation of bridge bonds. 73

5.2 Ball and stick model (part of a thin slice cut) of a Si-nc embedded in a-SiO_2. Dark spheres show Si atoms in the nc. Large (small) grey spheres show Si (O) atoms in the oxide, respectively. Arrows indicate the formation of bridge bonds. 74

5.3 Propability of finding an Oxygen atom versus its distance from the center of the nc. The initial size of the nc was $\sim$ 1.1 nm. Solid line denotes the probability for the initial structure, dotted line is for the structure before the compositional equilibration, and dashed line for the final structure. 75

5.4 Oxidation numbers versus the distance from the center of the nanocrystal, for the nc with size 1.1 nm. The vertical solid line shows the nominal position of the respective interface. 77

5.5 Variation of the (a) interface width and (b) interface energy with the Si-nc size. Solid lines are fits to the points. The dashed horizontal line in (a) shows the width of the ideal planar interface. The dashed horizontal lines in (b) show the energy of the planar interface without suboxides (bottom) and with suboxides (top). 79

5.6 Percentage of bridge bonding as a function of Si-nc size. Line is a fit to the points. 80

5.7 (a) The magnitude of the tetrahedral vector and (b) the strain energy of three different nanocrystals versus the distance from their center. The vertical solid lines show the nominal position of the respective interfaces (see text.) 81

6.1 Ball and stick model of the construction of the planar interface Si(111)/c-SiO_2. Dark spheres show Si atoms in the c-Si region. Large (small) grey spheres show Si (O) atoms in the oxide, respectively. 85

6.2 Seven different planar interfaces of Si/a-SiO_2. The crystal orientations are: (a)-(g): (100), (110), (111)I, (111)II, (210), (121), and (221). Dark spheres show Si atoms in the crystalline region. Small grey spheres show O and light grey spheres denote Si atoms in the oxide. . 87

6.3 The equilibrium shape of a macroscopic embedded Si crystal using the Wulff construction and the surface energies of Table 6.1. Dark gray shows the (100) facet, gray is the (110) and light gray denotes (121) facets. 89

6.4 Ball and stick model of the construction of a faceted Si-nc embedded in beta crystobalite. (a) Highly strained beta crystobalite. (b) Creation of a polyhedron and removing all O atoms in it. Dark spheres show Si atoms in the nc. Large (small) grey spheres show Si (O) atoms in the oxide, respectively. 90

6.5 Ball and stick model of the final structure of (a) a spherical (S2) and (b) a faceted (F2) nanocrystal. Dark spheres show Si atoms in the nc. Large (small) grey spheres show Si (O) atoms in the oxide. In (b) the (100) and the (121) planes are clearly distinguished. 91

6.6 Ball and stick model (a thin slice cut) of the final structure of (a) a spherical (S1) and (b) a faceted (F1) nanocrystal. Dark spheres show Si atoms in the nc. Large (small) grey spheres show Si (O) atoms in the oxide. The planes in F1 are not distinguished. 92

6.7 The bridge bonds of the F2 nanocrystal drawn together with the equilibrium shape given by the Wulff method. The arrows show the directions of the bridge rows. 93

7.1 GGA calculated density of states of a (a) SiH_4, (b) Si_5H_{12}, (c) $Si_{13}H_{28}$, (d) $Si_{35}H_{36}$, and (e) $Si_{87}H_{76}$ cluster. Gray (white) spheres denote Si (H) atoms. 101

7.2 Energy gap versus diameter (nm) for hydrogen passivated Silicon nanoclusters with (open symbols) and without (filled symbols) oxygen. The nanocrystals with a Si=O double bond are marked with open circles, while the one having a Si-O-Si double bond is marked with open square. The solid curve represents a simple fit of our results, whereas the dotted curve represents the theoretical result of Delerue, Allan, and Lannoo [129], and the dashed curve shows the result of Wang and Zunger [130]. 102

7.3 GGA calculated density of states of a (a) Si_5OH_{10}, (b) $Si_{13}OH_{26}$, (c) $Si_{13}OH_{26}$, (d) $Si_{13}O_2H_{24}$ cluster. (a) and (d) are structures having double bonds, while (c) and (d) have bridge bonds. Light gray balls represent Si, dark gray spheres denote O and white stands for H atoms. 103

7.4 GGA calculated density of states of the embedded Si clusters in a-SiO_2. S1 and S2 in panels (a) and (b), respectively. 105

7.5 GGA calculated density of states of the distorted isolated Si clusters with bridge bonds. B1 and B2 in panels (a) and (b), respectively. . . 106

7.6 GGA calculated density of states of the distorted isolated Si clusters passivated only by H. I1 and I2 in panels (a) and (b), respectively. . . 107

7.7 GGA calculated density of states of the isolated Si clusters with distortions and with one double bond. 108

A.1 Electronic and optical properties of bulk c-Si. (a) Density of states, (b) real (solid line) and imaginary part (dashed line) of dielectric function, and (c) the absorption coefficient. 115

A.2 Electronic and optical properties of a-Si. (a) Density of states, (b) real (solid line) and imaginary part (dashed line) of dielectric function, and (c) the absorption coefficient. 117

A.3 Electronic and optical properties of bulk β-cristobalite SiO_2. (a) Density of states, (b) real (solid line) and imaginary part (dashed line) of dielectric function, and (c) the absorption coefficient. 118

A.4 Absorption coefficient α(E) for four different samples (c-Si, S1, S2 and a-SiO_2 structures). 119

List of Tables

2.1 Parameters of the Keating-like potential for Silicon and Oxygen. . . . 37

6.1 Percentage of bridge bonds, oxidation numbers, interface widths σ (Å), energies of bridge bonds E_{bridge} (eV), and interface energies E_{inter} (eV/Å^2), for various orientations. The (100) orientation is used as a reference for the bridge bonds and the interface energies. 86

6.2 Characteristics of the four samples S1, F1, S2 and F2 (see text). . . . 90

6.3 Percentage of bridge bonds, Si suboxides and surface energy for the spherical and the faceted nanocrystal. 92

7.1 Characteristics of the structures S1 and S2. 104

7.2 Total energies of isolated Si-nc with/without oxygen. 108

Publications (related to the thesis)

- G. C. Hadjisavvas, and P. C. Kelires, *'Critical aspects of alloying and stress relaxation in Ge/Si(100) islands'*, Physical Review B, **72**, 075334 (2005).
- G. C. Hadjisavvas, and P. C. Kelires,*'Advances in Monte Carlo simulations of nanostructured materials'*, Computer Simulation Sudies in Condensed Matter Physics XVIII (Sprin-ger Verlag, Heidelberg, Berlin, 2005), in press.
- G. C. Hadjisavvas, and P. C. Kelires, *'Structure and Energetics of Si Nanocrystals Embedded in a-SiO_2'*, Physical Review Letters, **93**, 226104 (2004).
- G. Hadjisavvas, Ph. Sonnet. and P. C. Kelires, *'Stress and composition of C-induced Ge dots on Si(100)'*, Physical Review B, **67**, 241302(R) (2003).
- G. Hadjisavvas, Ph. Sonnet, and P. C. Kelires, *'Carbon-induced Ge Dots on Si(100) : Interplay of Strain and Chemical Effects'*, Proceedings of the Nato ARW, Crete, June 2003.

Bibliography

[1] I. N. Stranski, and L. Krastanow, Sitzungsber. Akad. Wiss. Wien, Math.-Naturwiss. Kl., Abt. 2B **146**, 797 (1938).

[2] D. J. Eaglesham, and M. Cerullo, *Dislocation-free Stranski-Krastanow growth of Ge on Si(100)*, Phys. Rev. Lett. **64**, 1943 (1990).

[3] Y.-M. Mo, D. E. Savage, B. S. Swartzentruber, and M. G. Lagally, *Kinetic pathway in Stranski-Krastanov growth of Ge on Si(001)*, Phys. Rev. Lett. **65**, 1020 (1990).

[4] O. Leifeld, A. Beyer, D. Grützmacher, and K. Kern, *Nucleation of Ge dots on the C-alloyed Si(001) surface*, Phys. Rev. B **66**, 125312 (2002).

[5] P.C. Kelires and J. Tersoff, *Equilibrium alloy properties by direct simulation: Oscillatory segregation at the Si-Ge(100) 2x1 surface*, Phys. Rev. Lett. **63**, 1164 (1989).

[6] P.C. Kelires, *Monte Carlo Studies of Ternary Semiconductor Alloys: Application to the $Si_{1-x-y}Ge_xC_y$ System*, Phys. Rev. Lett. **75**, 1114 (1995).

[7] A. Rastelli, M. Kummer and H. von Kaenel, *Reversible Shape Evolution of Ge Islands on Si(001)*, Phys. Rev. Lett. **87**, 256101 (2001).

[8] D. E. Jesson, M. Kaestner, and B. Voigtländer, *Direct Observation of Subcritical Fluctuations during the Formation of Strained Semiconductor Islands*, Phys. Rev. Lett. **84**, 330 (2000).

[9] P. Sutter, and M. C. Lagally, *Nucleationless Three-Dimensional Island Formation in Low-Misfit Heteroepitaxy*, Phys. Rev. Lett. **84**, 4637 (2000).

[10] R. M. Tromp, E. M. Ross, and M. C. Reuter, *Instability-Driven SiGe Island Growth*, Phys. Rev. Lett. **84**, 4641 (2000).

[11] A. Vailionis, B. Cho, G. Glass, P. Desjardins, D. G. Cahill, and J. E. Greene, *Pathway for the Strain-Driven Two-Dimensional to Three-Dimensional Transition during Growth of Ge on Si(001)*, Phys. Rev. Lett. **85**, 3672 (2000).

[12] A. Rastelli, M. Kummer, and H. von Kaenel, *Shape evolution of Ge domes on Si (0 0 1) during Si capping*, Physica E (Amsterdam) **13**, 1008 (2002).

[13] A. Rastelli, E. Mueller, and H. von Kaenel, *Shape preservation of Ge/Si(001) islands during Si capping*, Appl. Phys. Lett. **80**, 1438 (2002).

[14] P. Sutter, and M. C. Lagally, *Embedding of Nanoscale 3D SiGe Islands in a Si Matrix*, Phys. Rev. Lett. **81**, 3471 (1998).

[15] J. Tersoff, and R. M. Tromp, *Shape transition in growth of strained islands: Spontaneous formation of quantum wires*, Phys. Rev. Lett. **70**, 2782 (1993).

[16] J. Tersoff, and F. K. LeGoues, *Competing relaxation mechanisms in strained layers*, Phys. Rev. Lett. **72**, 3570 (1994).

[17] A. Barabási, *Self-assembled island formation in heteroepitaxial growth*, Appl. Phys. Lett. **70**, 2565 (1997).

[18] M. Kästner, and B. Voigtländer, *Kinetically Self-Limiting Growth of Ge Islands on Si(001)*, Phys. Rev. Lett. **82**, 2745 (1999)

[19] J. Tersoff, C. Teichert, and M. G. Lagally, *Self-Organization in Growth of Quantum Dot Superlattices*, Phys. Rev. Lett. **76**, 1675 (1996).

[20] F. M. Ross, J. Tersoff, and R. M. Tromp, *Coarsening of Self-Assembled Ge Quantum Dots on Si(001)*, Phys. Rev. Lett. **80**, 984 (1998).

[21] W. Yu and A. Madhukar, *Molecular Dynamics Study of Coherent Island Energetics, Stresses, and Strains in Highly Strained Epitaxy*, Phys. Rev. Lett. **79**, 905 (1997).

[22] N. Moll, M. Scheffler, and E. Pehlke, *Influence of surface stress on the equilibrium shape of strained quantum dots*, Phys. Rev. B **58**, 4566 (1998).

[23] D. E. Jesson, G. Chen, K. M. Chen, and S. J. Pennycook, *Self-Limiting Growth of Strained Faceted Islands*, Phys. Rev. Lett. **80**, 5156 (1998).

[24] P. Raiteri, L. Miglio, F. Valentinotti, and M. Celino, *Strain maps at the atomic scale below Ge pyramids and domes on a Si substrate*, Appl. Phys. Lett. **80**, 3736 (2002).

[25] J. Tersoff, *Enhanced Nucleation and Enrichment of Strained-Alloy Quantum Dots*, Phys. Rev. Lett. **81**, 3183 (1998).

[26] N. Liu, J. Tersoff, O. Baklenov, A. L. Holmes, and C. K. Shih, *Self-Limiting Growth of Strained Faceted Islands*, Phys. Rev. Lett. **80**, 5156 (1998).

[27] O. Kirfel, E. Müller, D. Grützmacher, and K. Kern, *Shape transformation of Ge quantum dots due to Si overgrowth*, Physica E **16**, 602 (2003).

[28] Ph. Sonnet and P.C. Kelires, *Monte Carlo studies of stress fields and intermixing in Ge/Si(100) quantum dots*, Phys. Rev. B **66**, 205307 (2002).

[29] S. A. Chaparro, J. Drucker, Y. Zhang, D. Chandrasekhar, M. R. McCartney, and D. J. Smith, *Strain-Driven Alloying in Ge/Si(100) Coherent Islands*, Phys. Rev. Lett. **83**, 1199 (1999).

[30] S. A. Chaparro, Y.Zhang, J. Drucker, D. Chandrasekhar, and D. J. Smith, *Evolution of Ge/Si(100) islands: Island size and temperature dependence*, J. Appl. Phys. **87**, 2245 (2000).

[31] Y. Zhang, M. Floyd, K. P. Driver, J. Drucker, P. A. Crozier, and D. J. Smith, *Evolution of Ge/Si(100) island morphology at high temperature*, Appl. Phys. Lett. **80**, 3623 (2002).

[32] G. Capellini, M. De Seta, and F. Evangelisti, *SiGe intermixing in Ge/Si(100) islands*, Appl. Phys. Lett. **78**, 303 (2001).

[33] X. Z. Liao, J. Zou, D. J. H, Cockayne, J. Qin, Z. M. Jiang, X. Wang, and R. Leon, *Strain relaxation by alloying effects in Ge islands grown on Si(001)*, Phys. Rev. B **60**, 15605 (1999).

[34] T.U. Schülli, J. Stangl, Z. Zhong, R.T. Lechner, M. Sztucki, T.H. Metzger, and G. Bauer, *Direct Determination of Strain and Composition Profiles in SiGe Islands by Anomalous X-Ray Diffraction at High Momentum Transfer*, Phys. Rev. Lett. **90**, 066105 (2003).

[35] U. Denker, M. Stoffel, and O.G. Schmidt, *Probing the Lateral Composition Profile of Self-Assembled Islands*, Phys. Rev. Lett. **90**, 196102 (2003).

[36] L.T. Canham, *Silicon quantum wire array fabrication by electrochemical and chemical dissolution of wafers*, Appl. Phys. Lett. **57**, 1046 (1990).

[37] L.W. Wang and A. Zunger, J. Phys. Chem. **98**, 2158 (1994).

[38] A. G. Cullis, L. T. Canham, and P. G. J. Calcott, *The structural and luminescence properties of porous silicon*, J. Appl. Phys. **82**, 909 (1997).

[39] M.V. Wolkin, J. Jorne, P.M. Fauchet, G. Allan, and C. Delerue, *Electronic States and Luminescence in Porous Silicon Quantum Dots: The Role of Oxygen*, Phys. Rev. Lett. **82**, 197 (1999).

[40] L. Pavesi, L. Dal Negro, C. Mazzoleni, G. Franzo, and F. Priolo, *Optical gain in silicon nanocrystals*, Nature (London) **408**, 440 (2000).

[41] T. Shimizu-Iwayama, K. Fujita, S. Nakao, K. Saitoh, T. Fujita, and N. Itoh, *Visible photoluminescence in* Si^+*-implanted silica glass*, J. Appl. Phys. **75**, 7779 (1994).

[42] J. G. Zhu, C. W. White, J. D. Budai, S. P. Withrow, and Y. Chen, *Growth of Ge, Si, and SiGe nanocrystals in* SiO_2 *matrices*, J. Appl. Phys. **78**, 4386 (1995).

[43] K. S. Min, K. V. Shcheglov, C. M. Yang, H. A. Atwater, M. L. Brongersma, and A. Polman, *Defect-related versus excitonic visible light emission from ion beam synthesized Si nanocrystals in* SiO_2, Appl. Phys. Lett. **69**, 2033 (1996).

[44] E. Werwa, A. A. Seraphin, L. A. Chiu, Chuxin Zhou, and K. D. Kolenbrander, *Synthesis and processing of silicon nanocrystallites using a pulsed laser ablation supersonic expansion*, Appl. Phys. Lett. **64**, 1821 (1994).

[45] L. N. Dinh, L. L. Chase, M. Balooch, L. J. Terminello, and F. Wooten, *Photoluminescence of oxidized silicon nanoclusters deposited on the basal plane of graphite*, Appl. Phys. Lett. **65** 3111 (1994).

[46] H. Morisaki, F. W. Ping, H. Ono, and K. Yazawa, *Above-band-gap photoluminescence from Si fine particles with oxide shell*, J. Appl. Phys. **70**, 1869 (1991).

[47] S. Hayashi, T. Nagareda, Y. Kanzawa, and K. Yamamoto, Jpn. J. Appl. Phys., Part 1 **32**, 3840 (1993).

[48] Y. Kanzawa, T. Kageyama, S. Takeoka, M. Fujii, S. Hayashi, and K. Yamamoto, *Size-dependent near-infrared photoluminescence spectra of Si nanocrystals embedded in* SiO_2 *matrices*, Solid State Commun. **102**, 533 (1997).

[49] P. Melinon *et al.*, Int. J. Mod. Phys. **9**, 339 (1995).

[50] F. Iacona, G. Franzo, and C. Spinella, *Correlation between luminescence and structural properties of Si nanocrystals*, J. Appl. Phys. **87**, 1295 (2000).

[51] T. Inokuma, Y. Wakayama, T. Muramoto, R. Aoki, Y. Kurata, and S. Hasegawa, *Optical properties of Si clusters and Si nanocrystallites in high-temperature annealed SiO_x films*, J. Appl. Phys. **83**, 2228 (1998).

[52] C. Bonafos, B Garrido, M. Lopez, A. Perez-Rodriguez, J. R. Morante, Y. Kihn, G. Ben Assayag, and A. Claveria, *An electron microscopy study of the growth of Ge nanoparticles in SiO_2*, Appl. Phys. Lett. **76**, 3962 (2000).

[53] Y. Kanemitsu, T. Ogawa, K. Shiraishi, and K. Takeda, *Visible photoluminescence from oxidized Si nanometer-sized spheres: Exciton confinement on a spherical shell*, Phys. Rev. B **48**, 4883 (1993).

[54] H. Hofmeister, F. Huisken, and B. Kohn, Eur. Phys. J. D **9**, 137 (1999).

[55] Yukari Ishikawa, N. Shibata, and S. Fukatsu, *Fabrication of highly oriented Si:SiO_2 nanoparticles using low energy oxygen ion implantation during Si molecular beam epitaxy.*, Appl. Phys. Lett. **68**, 2249 (1996).

[56] Y. Q. Wang, R. Smirani, F. Schiettekatte, and G. G. Ross, *Faceting os Si nanocrystals embedded in SiO_2*, Chem. Phys. Lett. **409**, 129 (2005).

[57] A. Pasquarello, M.S. Hybertsen, and R. Car, *Interface structure between silicon and its oxide by first-principles molecular dynamics*, Nature (London) **396**, 58 (1998).

[58] K.O. Ng and D. Vanderbilt, *Structure and oxidation kinetics of the Si(100)-SiO_2 interface*, Phys. Rev. B **59**, 10132 (1999).

[59] R. Buczko, S.J. Pennycook, and S.T. Pantelides, *Bonding Arrangements at the Si-SiO_2 and SiC-SiO_2 Interfaces and a Possible Origin of their Contrasting Properties*, Phys. Rev. Lett. **84**, 943 (2000).

[60] Y. Tu and J. Tersoff, *Microscopic Dynamics of Silicon Oxidation*, Phys. Rev. Lett. **89**, 086102 (2002).

[61] Y. Tu and J. Tersoff, *Structure and Energetics of the Si-SiO_2 Interface*, Phys. Rev. Lett. **84**, 4393 (2000).

[62] D. A. Luh, T. Miller, and T. C. Chiang, *Statistical Cross- Linking at the Si(111)/SiO_2 Interface*, Phys. Rev. Lett. bf 79, 3014 (1997).

[63] J.H. Oh *et al.*, *Chemical structure of the ultrathin SiO_2/Si(100) interface: An angle-resolved Si 2p photoemission study*, Phys. Rev. B **63**, 205310 (2001).

[64] A. A. Demkov, and O. F. Sankey, *Growth Study and Theoretical Investigation of the Ultrathin Oxide SiO_2-Si Heterojunction*, Phys. Rev. Lett. **83**, 2038 (1999).

[65] R. J. Baierle, M. J. Caldas, E. Molinari and Stefano Ossicini, *Optical emission from small Si particles*, Solid State Commun. **102**, 545 (1997).

[66] A. Puzder, A.J. Williamson, J.C. Grossman, and G. Galli, *Surface Chemistry of Silicon Nanoclusters*, Phys. Rev. Lett. **88**, 097401 (2002).

[67] I. Vasiliev, J.R. Chelikowsky, and R. Martin, *Surface oxidation effects on the optical properties of silicon nanocrystals*, Phys. Rev. B **65**, 121302(R) (2002).

[68] N. Daldosso *et al.*, *Role of the interface region on the optoelectronic properties of silicon nanocrystals embedded in SiO_2*, Phys. Rev. B **68**, 085327 (2003).

[69] N. Metropolis, A. Rosenbluth, M. Rosebluth, A. Teller, and E. Teller, *Equation of State Calculations by Fast Computing Machines*, J. Chem. Phys. **21**, 1087 (1953).

[70] W. H. Zachariasen, *The atomic arrangement in glass*, J. Am. Chem. Soc. **54**, 3841 (1932)

[71] R. Alben, D. Weaire, J. E. Smith, Jr., and M. H. Brodsky, *Vibrational properties of amorphous Si and Ge*, Phys. Rev. B **11**, 2271 (1975).

[72] W. Y. Ching, C. C. Lin, and L. Guttman, *Structural disorder and electronic properties of amorphous silicon*, Phys. Rev. B **16**, 5488 (1977).

[73] L. Guttman, W. Y. Ching, and J. Rath, *Charge-Density Variation in a Model of Amorphous Silicon*, Phys. Rev. Lett. **44**, 1513 (1980).

[74] F. Wooten, K. Winer, and D. Weaire, *Computer Generation of Structural Models of Amorphous Si and Ge*, Phys. Rev. Lett. **54**, 1392 (1985).

[75] D. Weaire, and N. Rivier, Contemp. Phys. **25**, 59 (1984).

[76] Lester Guttman, and Shafiqur M. Rahman, *Simulation of the structure of amorphous silicon dioxide*, Phys. Rev. B **37**, 2657 (1988).

[77] Yuhai Tu, J. Tersoff, G. Grinstein, and D. Vanderbilt, *Properties of a Continuous-Random-Network Model for Amorphous Systems*, Phys. Rev. Lett. **22**, 4899 (1998).

[78] G. T. Barkema, and N. Mousseau, *High-quality continues random networks*, Phys. Rev. B **62**, 4985 (2000).

[79] J. Tersoff, *Empirical interatomic potential for Silicon with improved elastic properties*, Phys. Rev. B **38**, 9902 (1988).

[80] J. Tersoff, *Empirical interatomic potential for carbon with applications to amorphous carbon*, Phys. Rev. Lett. **61**, 2879 (1988).

[81] J. Tersoff, *Modeling solid-state chemistry: Interatomic potentials for multicomponent systems*, Phys. Rev. B **39**, 5566 (1989).

[82] P. M. Morse, *Diatomic Molecules According to the Wave Mechanics. II. Vibrational Levels*, Phys. Rev. **34**, 57 (1930).

[83] G. C. Abell, *Empirical chemical pseudopotential theory of molecular and metallic bonding*, Phys. Rev. B **31**, 6184 (1985).

[84] J. L. Martins, and A. Zunger, *Stability of ordered bulk and epitaxial semiconductor alloys*, Phys. Rev. Lett. **56**, 1400 (1986).

[85] P. C. Kelires , *Simulations of Carbon Containing Semiconductor Alloys: Bonding, Strain Compensation, and Surface Structure*, Intern. J. of Mod. Phys. C **9**, 357 (1998);Surf. Sci. L**418**, 62 (1998).

[86] F. Stillinger, and T. Weber, *Computer simulation of local order in condensed phases of silicon*, Phys. Rev. B **31**, 5262 (1985)

[87] K. Ding, and H. C. Andersen, *Molecular-dynamics simulation of amorphous germanium*, Phys. Rev B **34**, 6987 (1986).

[88] P. C. Kelires,*Interfacial stability and intermixing in thin-layer Si_n/Ge_n superlattices*, Phys. Rev. B **49**, 11496(R) (1994).

[89] P. N. Keating, *Effect of Invariance REquirements on the Elastic Strain Energy of Crystals with Application to the Diamond Structure*, Phys. Rev. **145**, 637 (1966).

[90] D.R. Hamann, *Energetics of silicon suboxides*, Phys. Rev. B **61**, 9899 (2000).

[91] V. Vitek and T. Egami, *Atomic Level Stresses in Solids and Liquids*, Phys. Stat. Sol. **144**, 145 (1987).

[92] G. Wulff, Z. Kristallogr. Mineral. **34**, 449 (1901).

[93] M. Born, and R. Oppenheimer, *Zur Quantentheorie der Molekulen*, Ann. Phys. **84**, 457 (1927).

[94] P. Hohenberg and W. Kohn, *Inhomogeneous Electron Gas*, Phys. Rev. **136**, B864 (1964).

[95] W. Kohn and L. J. Sham, *Self-Consistent Equations Including Exchange and Correlation Effects*, Phys. Rev. **140**, A1133 (1965).

[96] J. F. Janak, *Proof that* $\partial E/\partial n_i = \varepsilon_i$ *in density-functional theory*, Phys. Rev. B **18**, 7165 (1978).

[97] J. P. Perdew, and A. Zunger, *Self-interaction correction to density-functional approximations for many-electron systems*, Phys. Rev. B **23**, 5048 (1981).

[98] J. P. Perdew, K. Burke, and Y. Wang, *Generalized gradient approximation for the exchange-correlation hole of a many electron system*, Phys. Rev. B **54** 16533 (1996).

[99] F. Bloch, Zeits. f. Physik bf 52, 555 (1928).

[100] G. Kresse, and J. Furthmüller, Comput. Mat. Sci. **6**, 15-50 (1996).

[101] G. Kresse, and J. Furthüller, *Efficient itaratice schemes for ab initio total-energy calculations using a plane-wave basis set*, Phys. Rev. B **54**, 11169 (1996)

[102] G. Kresse, and J. Hafner, *Ab initio molecular dynamics for liquid metals*, Phys. Rev. B **47**, 558 (1993).

[103] D. Vanderbilt, *Soft self-consistent pseudopotentials in a generalized eigenvalue formalism*, Phys. Rev. B **41**, 7892 (1990).

[104] G. Kresse, and J. Hafner, *Norm-conserving and ultrasoft pseudopotentials for first-row and transition elements*, J. Phys.: Condens. Matter **6**, 8245 (1994).

[105] A. Malachias, S. Kycia, G. Medeiros-Ribeiro, R. Magalhaes-Paniago, T.I. Kamins, and R.S. Williams, *3D Composition of Epitaxial Nanocrystals by Anomalous X-Ray Diffraction: Observation of a Si-Rich Core in Ge Domes on Si(100)*, Phys. Rev. Lett. **91**, 176101 (2003).

[106] G. Medeiros-Ribeiro, A. Malachias, S. Kycia, R. Magalhaes-Paniago, T.I. Kamins, and R.S. Williams, Appl. Phys. A **80**, 1211 (2005).

[107] N. Liu, J. Tersoff, O. Baklenov, A.L. Holmes, and C.K. Shih, *Nonuniform Composition Profile in* $In_{0.5}Ga_{0.5}As$ *Alloy Quantum Dots*, Phys. Rev. Lett. **84**, 334 (2000).

[108] K. Nakajima, A. Konishi, and K. Kimura, *Direct Observation of Intermixing at Ge /Si(001) Interfaces by High-Resolution Rutherford Backscattering Spectroscopy*, Phys. Rev. Lett. **83**, 1802 (1999).

[109] B.P. Uberuaga, M. Leskovar, A.P. Smith, H. Jónsson, and M. Olmstead, *Diffusion of Ge below the Si(100) Surface: Theory and Experiment*, Phys. Rev. Lett. **84**, 2441 (2000).

[110] Ph. Sonnet and P.C. Kelires, Appl. Phys. Lett. *Physical origin of trench formation in Ge/Si(100) islands*, **85**, 203 (2004).

[111] P.C. Kelires, J. Phys. Condens. Matter **16**, S1485 (2004).

[112] Note that we have no explicit barriers (activation energies) in the exchange moves, beside the implicit barriers associated with overcoming the small size mismatch. We are currently working on the inclusion of such exchange barriers in the algorithm.

[113] L. Nurminen, F. Tavazza, D.P. Landau, A. Kuronen, and K. Kaski, *Reconstruction and intermixing in thin Ge layers on Si(001)* , Phys. Rev. B **68**, 085326 (2003).

[114] G.C. Hadjisavvas, Ph. Sonnet, and P.C. Kelires, *Stress and composition of C-induced Ge dots on Si(100)*, Phys. Rev. B **67**, 241302(R) (2003).

[115] F. Montalenti *et al.*, *Atomic-Scale Pathway of the Pyramid-to-Dome Transition during Ge Growth on Si(001)*, Phys. Rev. Lett. **93**, 216102 (2004).

[116] O.G. Schmidt, C. Lange, K. Eberl, O. Kienzle, and F. Ernst, *Formation of carbon-induced germanium dots*, Appl. Phys. Lett. **71**, 2340 (1997).

[117] O.G. Schmidt and K. Eberl, *Photoluminescence and band edge alignment of C-induced Ge islands and related SiGeC structures*, Appl. Phys. Lett. **73**, 2790 (1998).

[118] O. Leifeld, D. Grützmacher, B. Müller, K. Kern, E. Kaxiras, and P.C. Kelires, *Dimer Pairing on the C-Alloyed Si(001) Surface*, Phys. Rev. Lett. **82**, 972 (1999).

[119] O. Leifeld, A. Beyer, D. Grützmacher, and K. Kern, *Nucleation of Ge dots on the C-alloyed Si(001) surface*, Phys. Rev. B **66**, 125312 (2002).

[120] I.N. Remediakis, E. Kaxiras, and P.C. Kelires, *Thermodynamics of C Incorporation on Si(100) from ab initio Calculations*, Phys. Rev. Lett. **86**, 4556 (2001).

[121] Ph. Sonnet, L. Stauffer, A. Selloni, A. De Vita, R. Car, L. Simon, M. Stoffel, and L. Kubler, *Energetics of surface and subsurface carbon incorporation in Si(100)*, Phys. Rev. B **62**, 6881 (2000).

[122] Ph. Sonnet and P.C. Kelires, *Monte Carlo studies of stress fields and intermixing in Ge/Si(100) quantum dots*, Phys. Rev. B **66**, 205307 (2002).

[123] A. Beyer, O. Leifeld, S. Stutz, E. Müller, and D. Grützmacher, Nanotechnology **11**, 298 (2000).

[124] J.P. Proot, C. Delerue, and G. Allan, *Electronic structure and optical properties of silicon crystallites: Application to porous silicon*, Appl. Phys. Lett. **61**, 1948 (1992).

[125] S. Ogut, J.R. Chelikowsky, and S.G. Louie, *Quantum Confinement and Optical Gaps in Si Nanocrystals*, Phys. Rev. Lett. **79**, 1770 (1997).

[126] F. J. Himpsel, F. R. McFeely, A. Taleb-Ibrahimi, and J. A. Yarmoff, *Microscopic structure of the SiO_2/Si interface*, Phys. Rev. B **38**, 6084 (1988).

[127] J. H. Oh, H. W. Yeom, Y. Hagimoto, K. Ono, M. Oshima, N. Hirashita, M. Nywa, A. Toriumi, and A. Kakizaki, *Chemical structure of the ultrathin SiO_2/Si(100) interface: An angle-resolved Si 2p photoemission study*, Phys. Rev. B **63**, 205310 (2001).

[128] M. Fyta, I.N. Remediakis, and P.C. Kelires, *Energetics and stability of nanostructured amorphous carbon*, Phys. Rev. B **67**, 035423 (2003).

[129] C. Delerue, G. Allan, and M. Lannoo, *Theoretical aspects of the luminescence of porous silicon*, Phys. Rev. B **48**, 11024 (1993)

[130] L.W. Wang and A. Zunger, *Solving Schrödinger's equation around a desired energy: Application to sillicon quantum dots* J. Phys. Chem. **100**, 2394 (1994).

[131] C. Herring, *Some Theorems on the Free Energies of Crystal Surfaces*, Phys. Rev. **82**, 87 (1951).

[132] S. Schuppler, S. L. Friedman, M. A. Marcus, D. L. Adler, Y.H. Xie, F. M. Ross, Y. J. Chabal, T. D. Harris, L. E. Brus, W. L. Brown, E. E. Chaban, P. F. Szajowski, S. B. Christman, and P. H. Citrin, *Size, shape, and composition of luminescent species in oxidized Si nanocrystals and H-passivated porous Si*, Phys. Rev. B **52** 4910 (1995).

[133] X. X. Wang, J. G. Zhang, L. Ding, B. W. Cheng, W. K. Ge, J. Z. Yu, and Q. M. Wang, *Origin and evolution of photoluminescence from Si nanocrystals embedded in a SiO_2 matrix.*, Phys. Rev. B **72**, 195313 (2005).

[134] G. G. Qin, and Y. J. Li, *Photoluminescence mechanism model for oxidized porous silicon and nanoscale-silicon-particle-embedded silicon oxide*, Phys. Rev. B **68**, 85309 (2003).

[135] J. P. Perdew, and Y. Wang, *Accurate and simple analytic representation of the electron-gas correlation energy*, Phys. Rev. B **45**, 13244 (1992).

[136] I. Tauc, *Amorphous and Liquid Semiconductors*, Plenum, London 175 (1974).

[137] E. A. David, and N. F. Mott, Phil. Mag. **22**, 903 (1970).